Multi-scale thermal-hydraulic modelling for the Primary Heat Transfer System of a tokamak

Doctoral Dissertation
Doctoral Program in Energy Engineering (30th Cycle)

Multi-scale thermal-hydraulic modelling for the Primary Heat Transfer System of a tokamak

By

Antonio Froio

******

Supervisor:
Prof. L. Savoldi

Doctoral Examination Committee:

Prof. P. A. Di Maio, Referee, Università degli Studi di Palermo
Dr. A. Ciampichetti, Referee, ITER Organization
Dr. F. Cismondi, Referee, EUROfusion Consortium
Dr. A. Del Nevo, Referee, ENEA
Prof. R. Zanino, Referee, Politecnico di Torino

Politecnico di Torino
2018

Declaration

I hereby declare that, the contents and organization of this dissertation constitute my own original work and does not compromise in any way the rights of third parties, including those relating to the security of personal data.

Antonio Froio

2018

This work has been carried out within the framework of the EUROfusion Consortium and has received funding from the Euratom research and training programme 2014-2018 under grant agreement No 633053. The views and opinions expressed herein do not necessarily reflect those of the European Commission.

* This dissertation is presented in partial fulfilment of the requirements for **Ph.D. degree** in the Graduate School of Politecnico di Torino (ScuDo).

A zio Totò, zio Alberto, zio Saverio, zio Pino, zia Rita e zio Franco

Acknowledgement

First of all, I wish to thank my mother, my father and my sister, who have been close to me despite the long distance that separates us since five years; thank you for supporting me all along my educational path.

I would also like to thank my supervisor, Laura, who guided me through my PhD experience, and prof. Zanino, whose expertise helped me a lot to improve the presentation of my work.

Many thanks to the EUROfusion Programme Management Unit staff in Garching, for their hospitality during my periods there, and in particular to Fabio and Sergio, who deeply helped me in the development of the thesis. Thanks also to prof. Casella, who introduced me to the magic of Modelica.

Thank you also to my friends, Mario, Francesco, Giorgio and Carlo, with whom I spent a lot of nice moments during my studies.

I also wish to thank all the PhD and MSc students that have shared this experience with me: Stefano, Dominic, Siew Sin, Andrea B., Alberto, Mattia, Haosheng, Andrea Z., Giuseppe, Valerio, Ortensia and Vincenzo: your presence made these years a lot less hard.

A special thank goes to my office mates, Raffaella T., Roberto, Stefano and Andrea Z., for all the funny moments we shared, and for sustaining me in the toughest moments. A particular thank to Raffaella T. and Raffaella G., who tolerated my random yelling in the office, and a very special one to Roberto and Stefano, who I had as fellows since the start of my MSc thesis five years ago, up to the very last moment of my PhD.

Finally, I deeply want to thank Elisabetta, who constantly stood at my side during all my University career: at moments, your presence and your belief in me have been the only reasons to go on. I feel much stronger when you are with me.

Abstract

The EU DEMO reactor is currently in its pre-conceptual design phase by the EUROfusion Consortium members; it aims to be the first tokamak fusion reactor to demonstrate the capability to produce net electrical energy from fusion reactions. To this aim, it must prove tritium self-sufficiency, and so it will be the first tokamak to include a Breeding Blanket (BB), to breed tritium exploiting lithium and the neutrons coming from the fusion reactions. Moreover, to prove feasibility of fusion electricity, the EU DEMO reactor will also be the first to include the power conversion chain, converting the heat coming from fusion reactions into electrical energy, through a Primary Heat Transfer System, which removes the heat deposited in the components close to the plasma and delivering it to the Power Conversion System, that, in the end, produces electricity.

Within this framework, a new computational tool is developed, supported by the EUROfusion Programme Management Unit. This code, called the GEneral Tokamak THErmal-hydraulic Model (GETTHEM), aims at fast, system-level, transient thermal-hydraulic modelling of the EU DEMO Primary Heat Transfer System and Balance-of-Plant (BoP), including all the in-vessel and ex-vessel cooling components, and it is the first system-level code of this type explicitly developed for fusion applications. The thermal-hydraulic models of the in-vessel components are developed, starting from the BB, as it is the most thermally loaded component and, consequently, the most important for the BoP. The GETTHEM development currently focuses on two out of the four BB concepts studied in the EU, namely the Helium-Cooled Pebble Bed (HCPB) and the Water-Cooled Lithium-Lead (WCLL) BB concepts. Considering that the EU DEMO is still in pre-conceptual design, the code focuses on execution speed, while maintaining an acceptable accuracy, typically modelling the different components as 0D/1D interconnected objects.

GETTHEM is applied to analyse the coolant distribution in the HCPB BB, as well as the maximum temperature reached under normal operating condition in the structural material of both BB concepts, which must stay below 550 °C as a safety requirement. The model is capable to highlight if and where the coolant distribution in the HCPB BB should be optimized in order to avoid an overheating of the structures, allowing at the same time to reduce the compression power needed to circulate the coolant. It also can show if in some regions of the BB, for both coolant options, more detailed analyses are needed, as the current design, tailored on the equatorial BB region, somehow penalizes the regions far from the equatorial plane. Moreover, a separate module of the code is developed, aiming, through suitable simplifications, at fast modelling of accidental transients such as in-vessel Loss-Of-Coolant Accidents (LOCAs). Such module of the code is applied to the parametric analysis of an in-vessel LOCA for HCPB and WCLL, exploiting the code speed to rapidly screen the effect, for instance, of different break sizes, contributing to the proper sizing of the Vacuum Vessel Pressure Suppression System.

Contents

List of Figures

List of Tables

Nomenclature

Abbreviations

BB	Breeding Blanket
BC	Boundary Condition
BD	Burst Disk
BL	Bleed Line
BV	Bleed Valve
BM	Blanket Module
BoP	Balance-of-Plant
BSS	Back Supporting Structure
BWR	Boiling Water Reactor
BZ	Breeding Zone
CEA	Commissariat à l'énergie atomique et aux énergies alternatives
CFD	Computational Fluid-Dynamics
CIEMAT	Centro de Investigaciones Energéticas, Medioambientales y Tecnológica
CP	Cooling Plates
DAE	Differential and Algebraic Equation
DBA	Design-Basis Accident
DCLL	Dual Cooled Lithium-Lead
DWT	Double-Walled Tubes
ENEA	Agenzia nazionale per le nuove tecnologie, l'energia e lo sviluppo economico sostenibile
EU DEMO	European Demonstration Fusion Power Reactor
EV	Expansion Volume
FV	Finite Volume
FW	First Wall
GETTHEM	GEneral Tokamak THErmal-hydraulic Model
HCLL	Helium-Cooled Lithium-Lead
HCPB	Helium-Cooled Pebble Bed
HCPB-I	HCPB-Integrated
HCPB-S	HCPB-Separated
HELOKA	HElium LOop KArlsruhe
HX	Heat Exchanger
IAPWS	International Association for the Properties of Water and Steam
IB	Inboard
ICE	Ingress of Coolant Event

ICE facility	Inlet Coolant Event Facility
IF97	Industrial Formulation ‘97
IHTS	Intermediate Heat Transfer System
IV	Isolation Valve
KIT	Karlsruher Institut für Technologie
LOCA	Loss-Of-Coolant Accident
MMS	Multi-Module Segment
MS	Molten salts
NBI	Neutral Beam Injector
NWL	Nuclear Wall Load
OB	Outboard
ODE	Ordinary Differential Equation
OSMC	Open-Source Modelica Consortium
PC	Plasma Chamber
PCS	Power Conversion System
PDE	Partial Differential Equation
PHTS	Primary Heat Transfer System
PMU	Programme Management Unit
RL	Relief Line
RM	Remote Maintenance
SMS	Single-Module Segment
SP	Suppression Pool
ST	Suppression Tank
VV	Vacuum Vessel
VVPSS	Vacuum Vessel Pressure Suppression System
WCLL	Water-Cooled Lithium-Lead

Symbols

A	Area of channel cross section
C	Heat capacity
c	Specific heat
e	Specific internal energy
F_F	Liquid critical pressure ratio factor
F_k	Ratio of specific heat factor
f_p	Peaking / shape factor
HTC	Heat transfer coefficient
h	Specific enthalpy
K	Localized pressure loss coefficient
k	Thermal conductivity
L, l	Length
m	Mass
$\dot{m}$	Mass flow rate

p	Pressure
Δp	Pressure drop
$\dot{Q}$	Power
S	Heat transfer surface
s	Specific entropy
T	Temperature
t	Time
V	Volume
v	Speed
Y	Compressibility factor
x	Vapour quality
x_T	Terminal pressure drop ratio

Greek

γ	Ratio of specific heats
ϵ	Error
ρ	Density
ϕ	Internal diameter
Ω	Heat transfer perimeter

Subscripts

ave	Average
ch	Choked
$c, crit$	Critical
eff	Effective
ext	External
i	Volume index
in	Inlet/Input
l	Saturated liquid
loc	Localized pressure drop
m	Solid
$m \rightarrow f$	From solid to fluid
nom	Nominal
$thresh$	Threshold
w	Water
v	Saturated vapour

Chapter 1

Introduction

1.1. The EU DEMO tokamak

The European Demonstration Fusion Power Reactor (EU DEMO), under development by the EUROfusion Consortium [1], aims to become the first reactor to produce net electrical energy from nuclear fusion reactions [2], at least in Europe. The plant, which is currently in its pre-conceptual design phase, should be operating by the 2050s; a scheme of the 2015 revision [3] of the reactor (which is the basis for this dissertation) is reported in Figure 1.1. In this revision, the tokamak is toroidally segmented in 18 equal sectors, separated by the Toroidal Field coils[1].

In view of its mission, the EU DEMO will be the first reactor to include the components needed to produce electricity, i.e. the Balance-of-Plant (BoP). Also, since the reactor will be based on the deuterium-tritium fusion reaction, it must produce the tritium it needs to operate: in fact, tritium is a radioactive isotope with a relatively short half-life, which is then hard to find in nature; a sustainable fusion power plant should prove that it is possible to close the fuel cycle producing enough tritium in situ. As a consequence, the EU DEMO will include a component known as the Breeding Blanket (BB), which should be the first component facing the plasma, where the neutrons produced by the fusion reactions will interact with lithium, to produce tritium. Since it faces directly the plasma, the BB will experience

[1] The most recent EU DEMO design at the moment of writing is the 2017 revision, which foresees 16 sectors. Since this revision was issued after most of the work described here has been performed, the 2015 revision is taken as reference.

the largest total power deposition, becoming the most important component from the heat removal point of view, and then for the electricity production. The heat will be removed through a Primary Heat Transfer System (PHTS), with different coolant options under investigations according to the blanket concepts, but all eventually delivering the heat to a steam generator, to have a Rankine cycle in the Power Conversion System (PCS) to produce electricity. Since the EU DEMO operation will be pulsed, to avoid pulsation in the turbine operation (which would reduce its lifetime), several options are under investigation, among which the most promising one is to use an Intermediate Heat Transfer System (IHTS), using molten salts (MS) as energy storage fluid. In this case, the PHTS would deliver the heat to a heat exchanger (HX) having MS on the secondary side, and the IHTS would integrate the steam generator; a conceptual scheme of the DEMO BoP is reported in Figure 1.2.

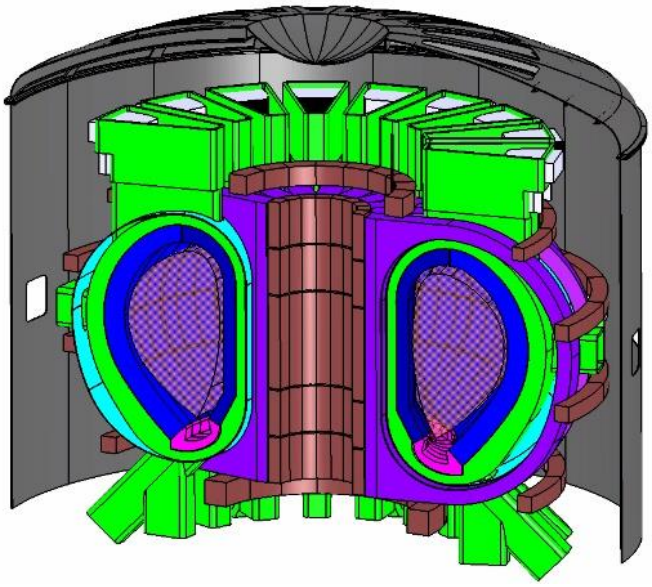

Figure 1.1: The EU DEMO tokamak, 2015 revision [3, 4].

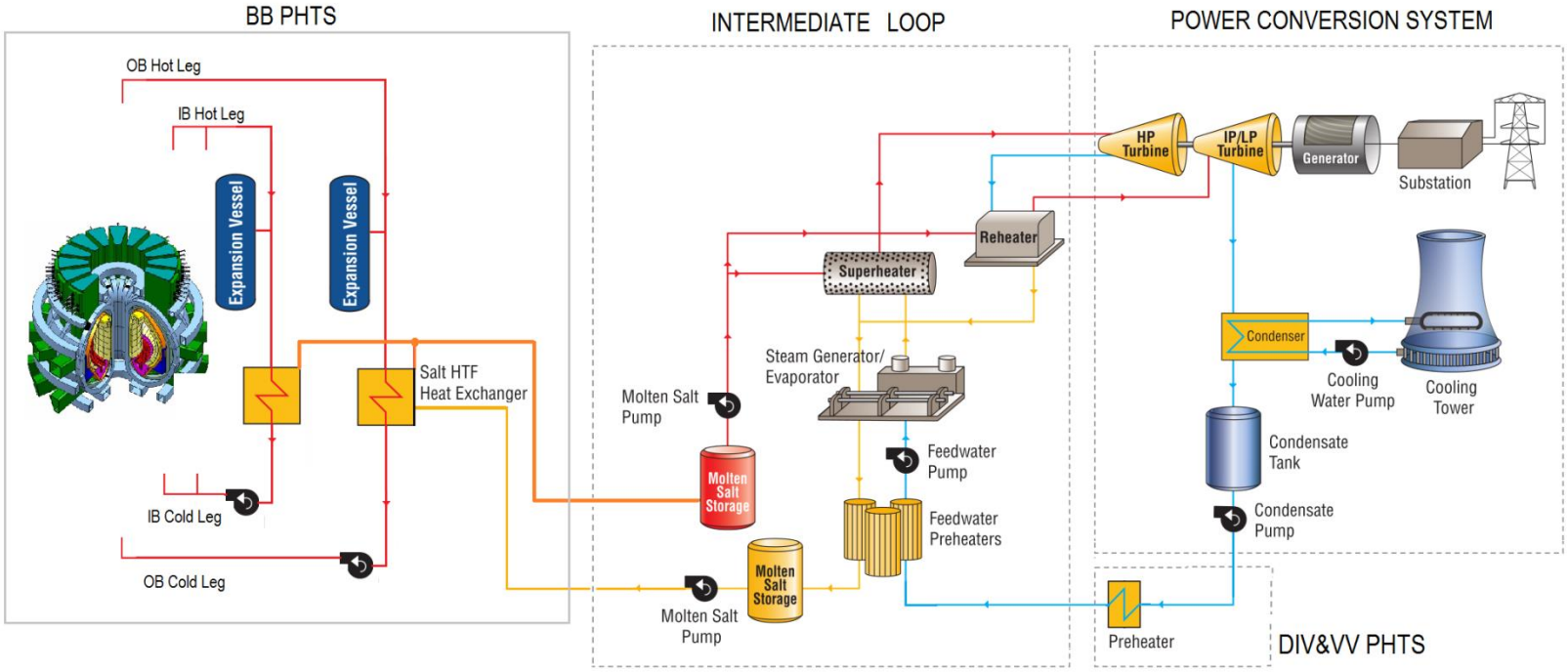

Figure 1.2: Conceptual scheme of the EU DEMO BoP (reproduced from [5]).

1.2. The EU DEMO Breeding Blanket

In the 2015 revision of the EU DEMO, each tokamak sector contains three outboard (OB) and two inboard (IB) BB segments; each BB segment may in turn be poloidally divided in Blanket Modules (BM), according to the different designs [6]. A scheme of the BB segmentation is reported in Figure 1.3.

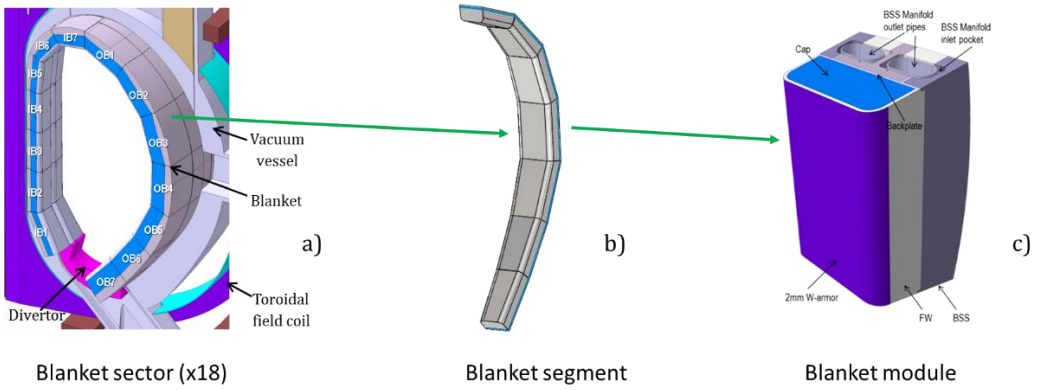

Figure 1.3: The 2015 EU DEMO BB segmentation, showing a blanket sector (a), a blanket segment (b) and a BM (c) (adapted from [6, 7]).

The BB has two main roles: the first one is of course to breed tritium, exploiting two nuclear reactions having as reactants a neutron (which is a product of the deuterium-tritium fusion) and two isotopes of lithium, namely the reactions ^{6}Li(n,α)T (exothermic, yielding 4.8 MeV) and ^{7}Li(n,n'α)T (endothermic, consuming 2.5 MeV). To this aim, inside the BB a Li-rich material (hereafter called "breeder") is used, together with a neutron multiplier to complete the neutron balance and compensate for escaping neutrons or parasitic captures; the region of the BB where these materials are found is then called the Breeding Zone (BZ). The BZ is separated from the plasma by means of a First Wall (FW), which is the first solid component facing the plasma.

On the other hand, as mentioned above, the BB has the total largest thermal load, so it must be adequately cooled to avoid failures, at the same time transferring this heat to the primary coolant, in order to produce electricity. So, both the BZ and the FW contain cooling channels where the primary coolant increases its enthalpy removing power from the BB components.

In EU, four different BB concepts are being explored, with different coolants and/or breeders:

- The Helium-Cooled Pebble Bed (HCPB) uses helium as coolant, Li_4SiO_4 pebbles as breeder and Be pebbles as neutron multiplier; its development is led by *Karlsruher Institut für Technologie* (KIT, Germany) [7].
- The Water-Cooled Lithium-Lead (WCLL) uses water as coolant and LiPb liquid eutectic as breeder and neutron multiplier; its development is led by *Agenzia nazionale per le nuove tecnologie, l'energia e lo sviluppo economico sostenibile* (ENEA, Italy) [8].
- The Helium-Cooled Lithium-Lead (HCLL) uses helium as coolant and LiPb liquid eutectic as breeder and neutron multiplier; its development is led by *Commissariat à l'énergie atomique et aux énergies alternatives* (CEA, France) [9].
- The Dual Cooled Lithium-Lead (DCLL) uses helium as coolant for the FW and LiPb liquid eutectic both as breeder and neutron multiplier, and as coolant for the BZ; its development is led by *Centro de Investigaciones Energéticas, Medioambientales y Tecnológicas* (CIEMAT, Spain) [10].

This work focuses only on HCPB and WCLL, which are described more in detail in the following.

1.2.1. The Helium-Cooled Pebble Bed blanket concept

The most recent design (2015) of the HCPB BB [7] is based on a Multi-Module Segment (MMS) approach and foresees a poloidal subdivision in 7 BMs, both for the IB and OB segments; a sketch of the OB equatorial BM is reported in Figure 1.4a. The BZ is organized as a sandwich structure, with the two mentioned pebble beds (Li_4SiO_4 and Be), alternated and separated by metalling Cooling Plates (CPs), acting as stiffening structure and also providing a pathway for the coolant, see Figure 1.4b. The FW and BZ are cooled in series, using helium at 80 bar in the range 300 °C – 500 °C. The coolant is distributed to the square (12.5×12.5 mm²) FW cooling channels by a manifold located in the segment Back Supporting Structure (BSS); it is then collected inside a BM-wide manifold, which redistributes it to the CPs, where another manifold distributes the coolant to the CP rectangular (5×2.5 mm²) channels. The coolant is then collected, at first at CP level, then at BM level and finally delivered to the outlet manifold in the segment BSS. All the components are cooled by two loops running in countercurrent (hereafter called A and

B)[2], such that each channel is surrounded by two channels running in the opposite direction, with the aim of having a toroidally symmetric temperature field. The scheme of the HCPB coolant flow path is reported in Figure 1.5.

Figure 1.6 reports a detailed cross section of an elementary cell of a HCPB BM; it clearly shows how inside a CP, in addition to the cooling channels referring to loops A and B, there is a third type of channels, called "dummy" channels as no coolant flows inside them; consequently, all the channels in the CP are equally spaced, but the active channels rarefy going from the FW towards the BSS, in order to have more cooling power in the part of the BM closer to the plasma.

Even though the HCPB foresees a single cooling system for both BZ and FW the PHTS for such BB concept is segmented in different, independent loops, in view of the very large helium volumes involved: in particular, six loops are foreseen for the OB cooling (three sectors each), whereas three loops are foreseen for the IB cooling (six sectors each) [11]. The layout of the HCPB PHTS is reported in Figure 1.7.

The IHTS and PCS for HCPB have not been designed yet; nevertheless, the HXs of the PHTS are designed as He-MS HX: in particular, they are tube-and-shell HXs, with primary helium flowing in the tubes and MS flowing in the shell. The heat deposited in the divertor and Vacuum Vessel (VV) will be used in the PCS to preheat the feedwater, before it enters the steam generator.

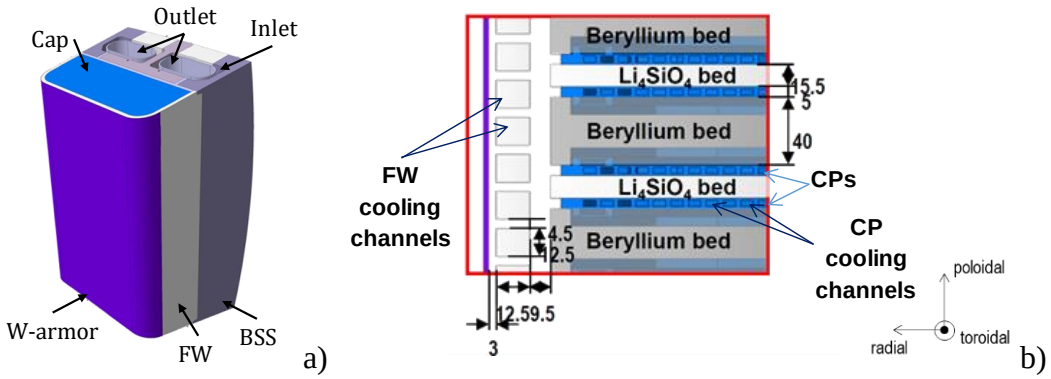

Figure 1.4: The HCPB OB equatorial BM (OB4) (a) and a radial-poloidal cross section, showing the alternate structure of breeder, neutron multiplier and cooling plates (reproduced from [7]).

[2] The two loops are not redundant.

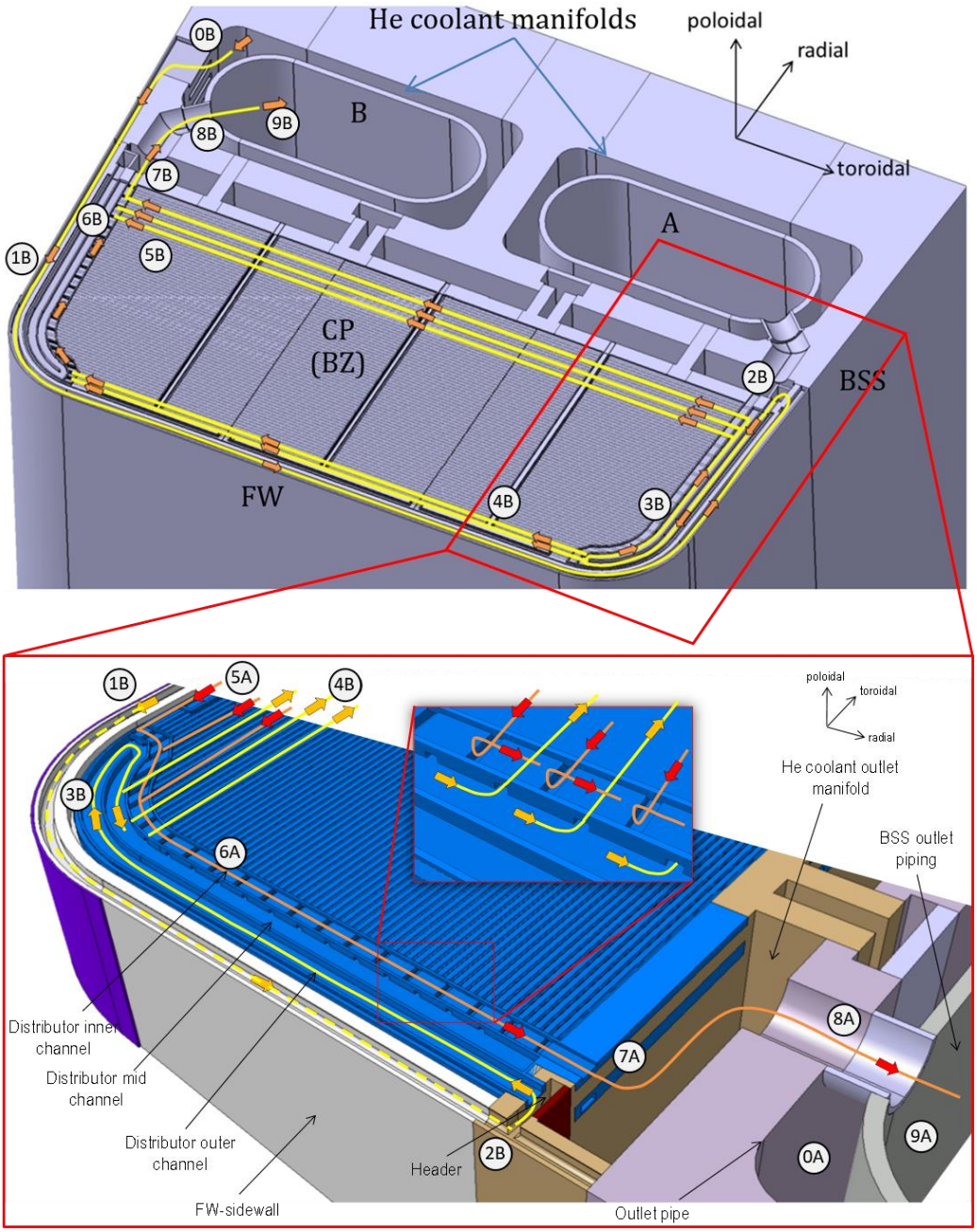

Figure 1.5: Coolant flow path in the HCPB: the coolant is distributed initially from the manifold in the BSS (bullet 0) to the FW square cooling channels (bullet 1), and it is successively collected and redistributed (bullets 2 and 3, respectively) to the CP rectangular cooling channels (bullets 4 and 5) by a rather complex system of internal manifolds, before being collected again in a manifold inside the CP at first (bullet 6) and in a BM-wide manifold (bullet 7), which finally delivers the hot coolant to the outlet manifold inside the BSS (bullets 8 and 9). The red lines and arrows refer to loop A, whereas the yellow ones refer to loop B (adapted from [7, 12]).

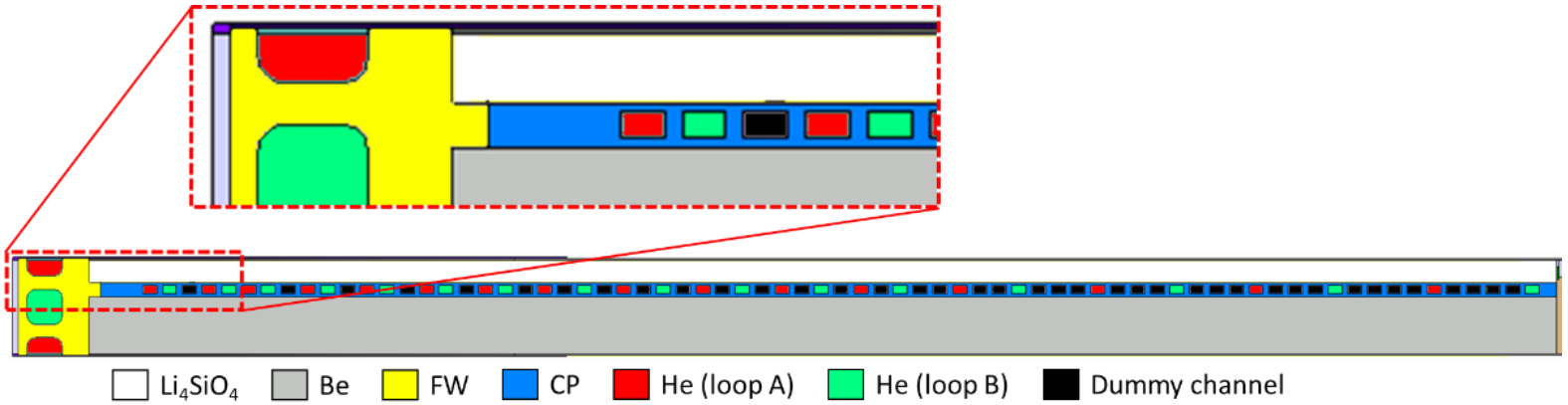

Figure 1.6: Detailed view of a HCPB elementary cell, showing the different regions and cooling channels, as well as the dummy channels (adapted from [13]).

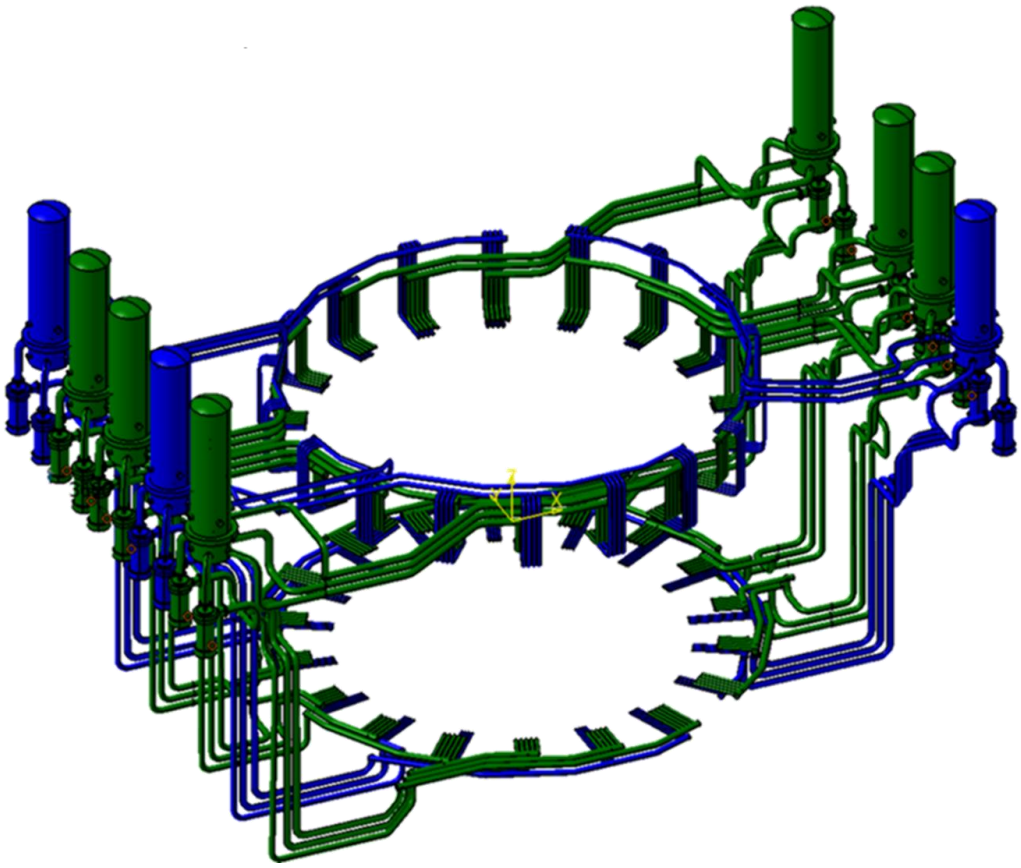

Figure 1.7: The HCPB BB PHTS; the blue components refer to the IB PHTS, whereas the green components refer to the OB PHTS (reproduced from [11]).

1.2.2. The Water-Cooled Lithium-Lead blanket concept

The 2016 version of the WCLL BB [8] is instead based, as opposed to the HCPB concept, on the Single-Module Segment (SMS) approach, i.e. the segments are not poloidally subdivided; a WCLL OB segment and its internals are reported in Figure 1.8. The segment design is based on an elementary cell, shown in Figure 1.9, which is repeated in the poloidal direction. The liquid breeder (LiPb) flows in the free space around the BZ cooling tubes, entering the BM from below each baffle plate and exiting from above; the 21 BZ cooling tubes of each elementary cell are Double-Walled Tubes (DWT, ϕ8 mm), with two EUROFER walls separated by a copper layer, in order to reduce the probability of interaction between hot pressurized water and liquid LiPb, which could cause severe pressure and temperature transients and hydrogen production. The FW cooling channels are square (7×7 mm²); in this case, the same countercurrent approach as described in HCPB is used, with the only difference that all the channels refer to the same loop.

Differently from the HCPB, the FW and the BZ are cooled independently; the coolant is distributed to and collected from those channels by manifolds located in the BSS, which are shown in Figure 1.10.

The WCLL PHTS is divided in two separate cooling circuits, one for the FW and one for the BZ; all the segments refer to the same circuit; each cooling circuit is articulated in two (connected) loops, each one having its own HX/Steam Generator and circulation pump. The FW PHTS is connected to the IHTS, providing heat to the MS energy storage system, whereas the BZ PHTS delivers the power directly to the PCS [15]. A 3D view of the WCLL PHTS is reported in Figure 1.11, whereas the Process Flow Diagram of the entire WCLL BoP is shown in Figure 1.12. In this figure, also the role of the heat coming from the VV and divertor is shown: as already mentioned for the HCPB, the heat transfer systems for such components will provide low-temperature heat, which will be used to preheat the PCS feedwater, before it enters the steam generator.

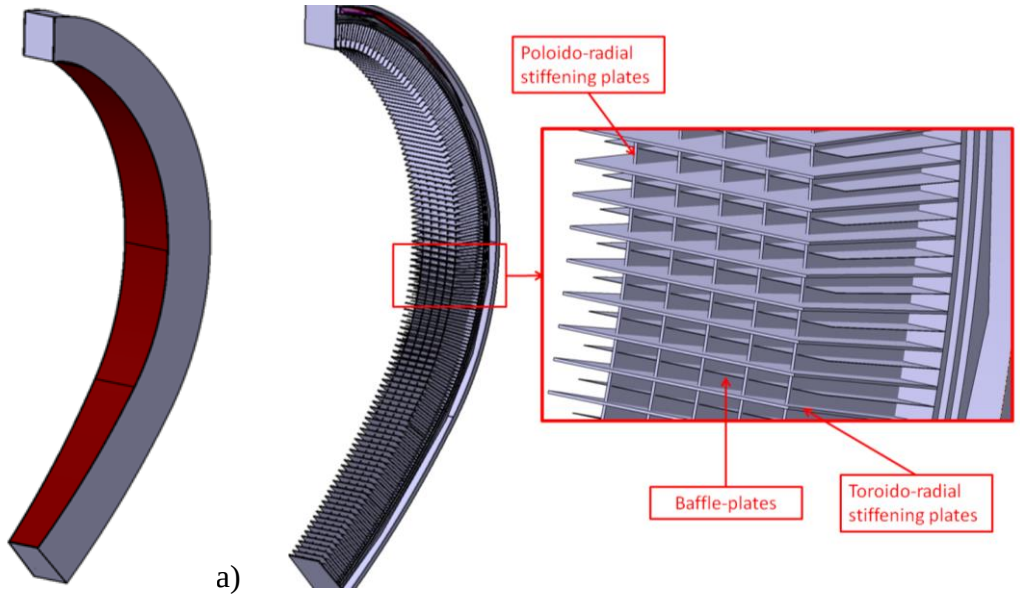

Figure 1.8: The 2016 WCLL OB segment (a) and its internal view (b); the toroido-radial stiffening plates separate the elementary cells (reproduced from [8]).

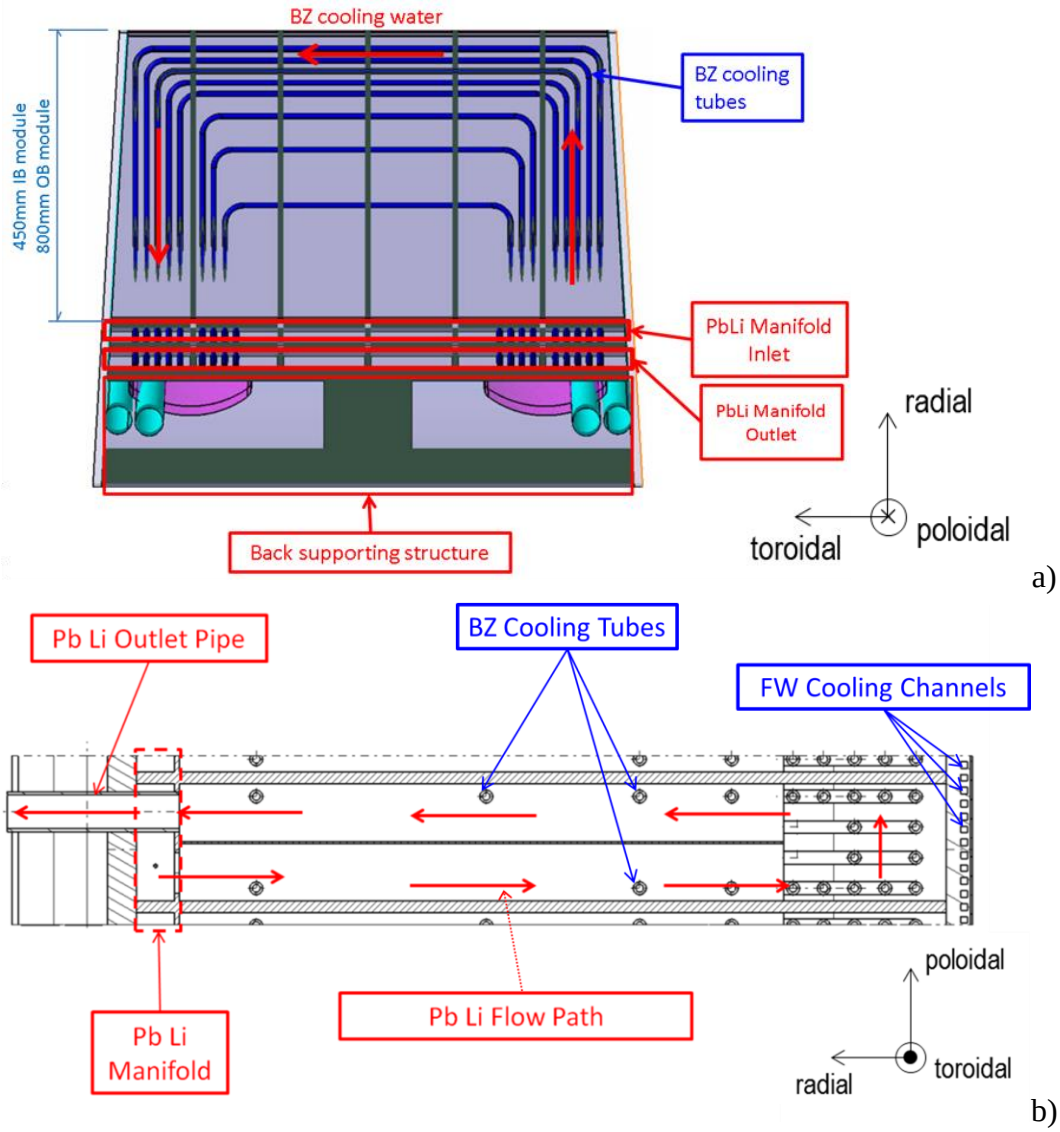

Figure 1.9: Radial-toroidal (a) and radial-poloidal (b) cross sections of the WCLL elementary cell (reproduced from [8]).

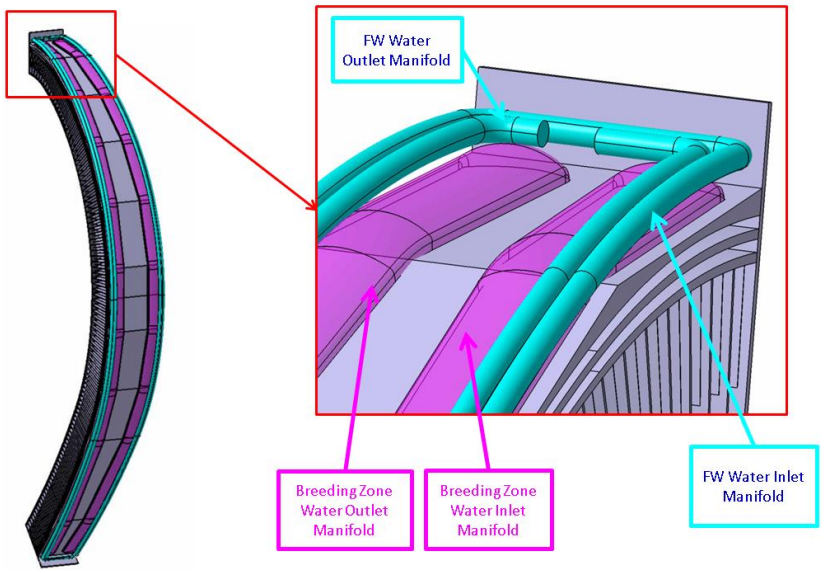

Figure 1.10: The WCLL BSS, showing the coolant manifold (reproduced from [14]).

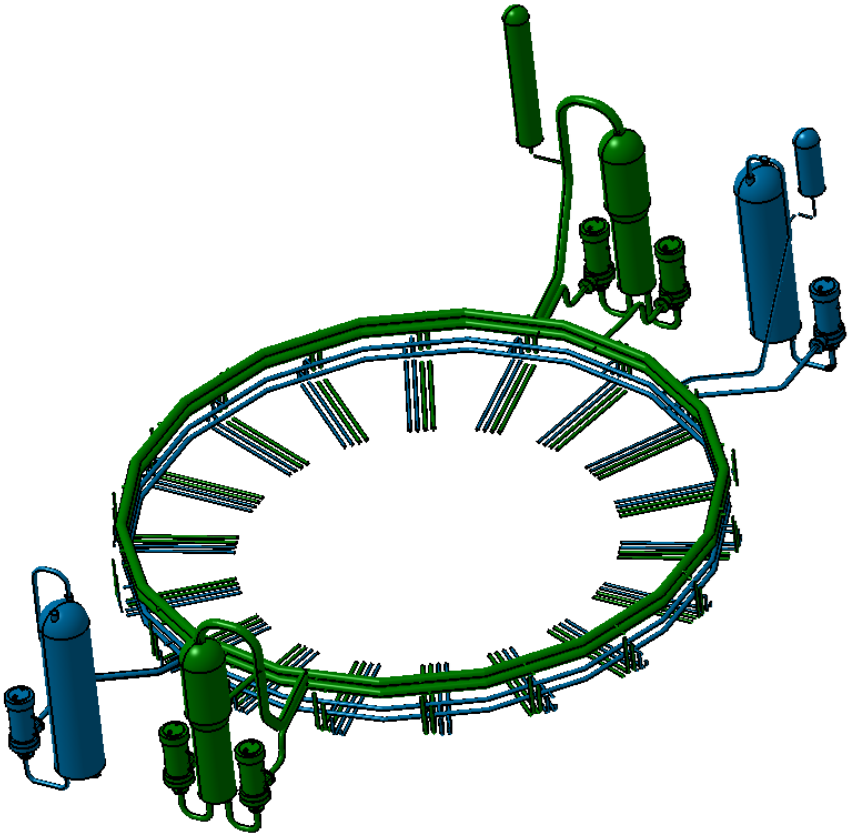

Figure 1.11: The WCLL BB PHTS; the blue components refer to the FW PHTS, whereas the green components refer to the BZ PHTS (reproduced from [15]).

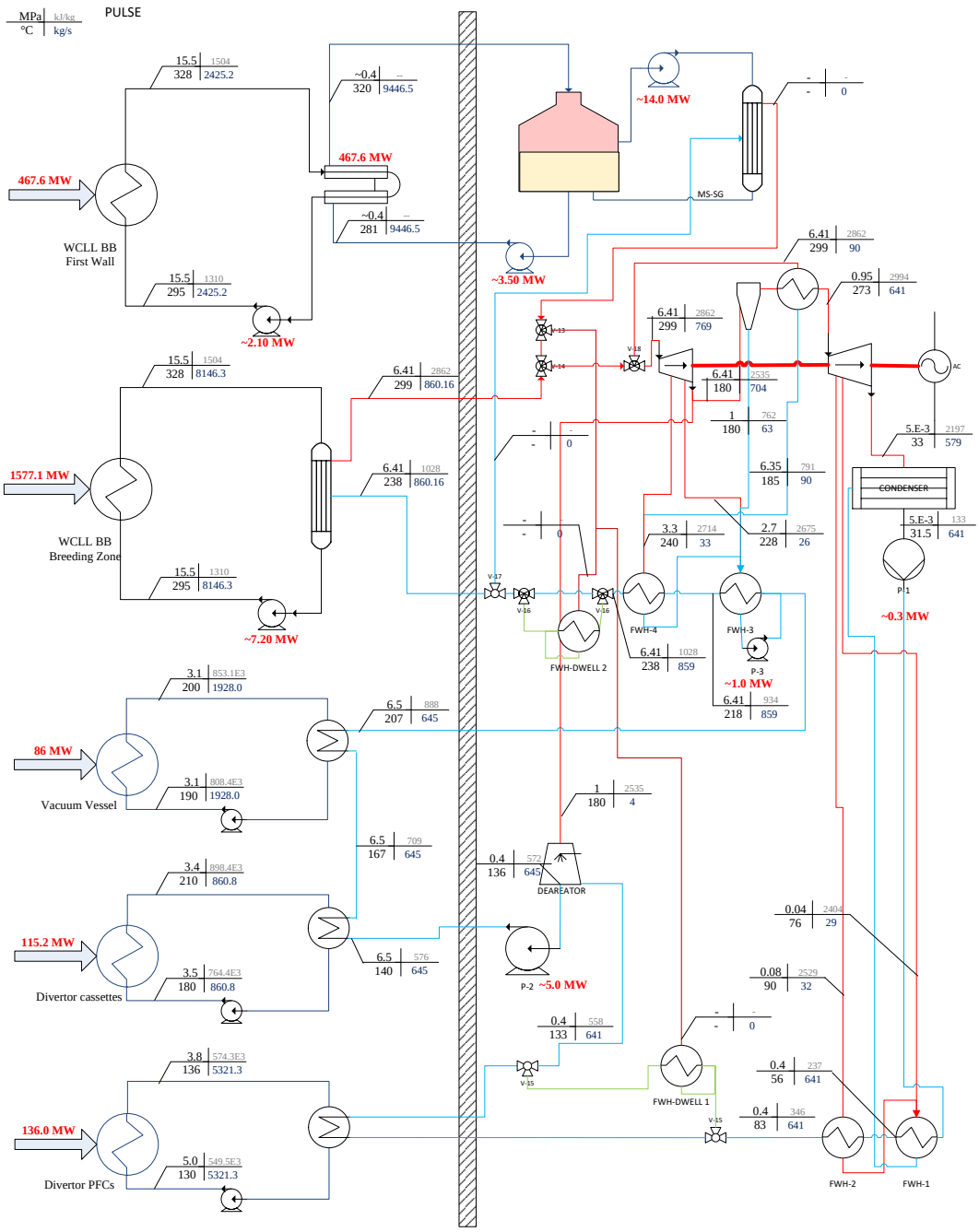

Figure 1.12: Process flow diagram of the WCLL BoP (reproduced from [15]).

1.3. The EU DEMO Vacuum Vessel Pressure Suppression System

One of the accidents which are going to be considered as Design Basis Accidents (DBAs) for the EU DEMO is the so-called in-VV Loss-Of-Coolant Accident (LOCA), which takes place when part of the blanket (or divertor) coolant is released inside the VV (it is consequently also known as Ingress of Coolant Event, ICE) causing the pressure inside the VV to increase.

Since the VV operates at very low pressures (order of mPa at most, during plasma pulse), its overpressurization must be limited below its design value, to avoid loss of radioactive inventory to the reactor building (in this sense, the VV is the primary containment barrier). To avoid this kind of transient, a VV Pressure Suppression System (VVPSS) is foreseen, which should provide a safe storage for the contaminated coolant, avoiding at the same time the VV overpressurization. This system will have of course different designs, according to the different coolants: if water is to be used, as in the WCLL BB, it will immediately flash to steam when entering the VV, and so its pressure can be reduced by condensing it back to liquid in a Suppression Pool (SP), according to the same approach used in fission Boiling Water Reactors (BWR). On the other hand, if helium will be used, it will necessarily expand, so an adequate volume (called Expansion Volume, EV) is to be provided.

To avoid the pressure increase in the VV, it will be equipped with Burst Disks (BDs), which passively open when a certain pressure inside the VV is reached; these will be bypassed by Bleed Lines (BLs), which are equipped with actively operated valves (Bleed Valves, BVs) to be opened at a lower set-point: this could be useful in case of small leakages, to avoid the rupture of the BDs which, to be replaced, would need the intervention of the Remote Maintenance (RM) system, causing the machine availability to suddenly decrease. A sketch of the EU DEMO VVPSS is reported in Figure 1.13.

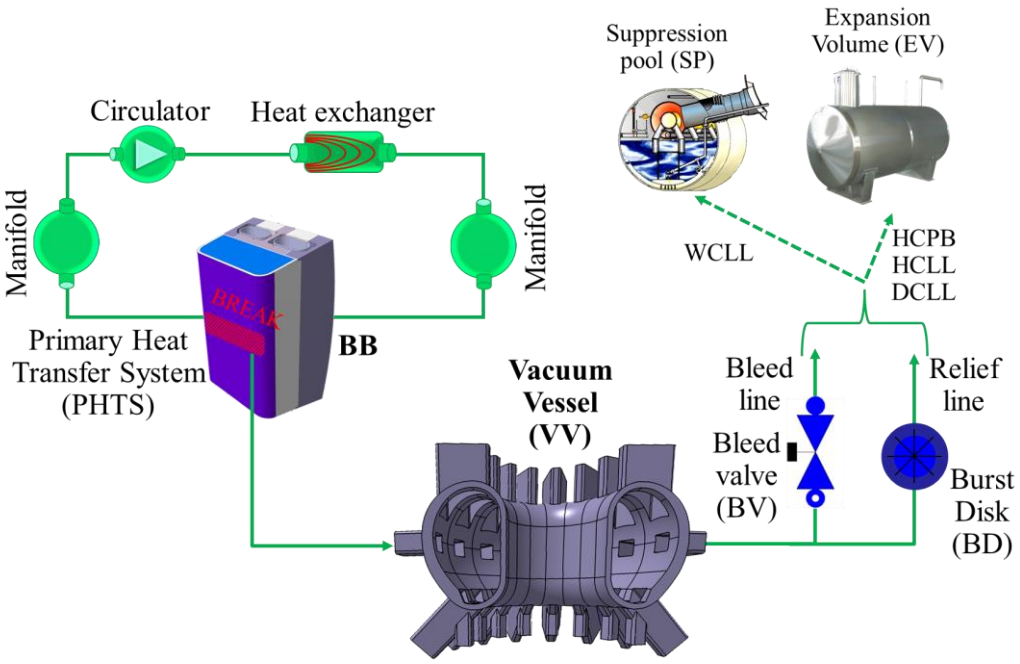

Figure 1.13: Sketch of the EU DEMO VVPSS.

1.4. Aim of the thesis

As DEMO is in its pre-conceptual design phase, its macroscopic design parameters undergo frequent changes, so that all the input data used by the designers can hardly be considered as final. In this sense, it is pointless to have very detailed models to perform precise computer simulations, which can consume a lot of time and computational power, that may become deprecated after a few months. However, computational tools are fundamental to verify the design calculations and give quick and targeted feedbacks for subsequent iterations in the design process.

This work aims to answer the above-mentioned needs, by starting the development of a new computational code, called the GEneral Tokamak THErmal-hydraulic Model (GETTHEM): it is a system-level, fast-running code for the transient thermal-hydraulic modelling of the EU DEMO PHTS and BoP, with the support of the EUROfusion Programme Management Unit (PMU). The aim is to have a fast running system tool, which includes all the components relevant for the power generation, from the in-vessel components up to the turbine, in order to rapidly analyse the effect of several parameters, and provide feedbacks on the different components to the design teams. A tool like this could also be useful in order to identify the most

critical points, which need to be investigated more in detail using other, expensive computational tools, such as 3D Computational Fluid-Dynamic (CFD) codes.

After the development and before its application, the code reliability must be properly checked by means of benchmark/validation exercises, both in normal and off-normal operating conditions. After that, it will ensure a good capability to properly reproduce the physics of the system in a possibly wide range within the relevant operating parameter space.

Chapter 2

The GETTHEM code

2.1. The programming environment

Considering the mission of the code, which was described in the previous chapter, the Modelica®[3] language version 3 [16, 17, 18, 19] was chosen as language for the GETTHEM development. Modelica® is an object-oriented, equation-based, a-causal, declarative modelling language, developed to enable simple modelling of complex systems, suitable for multiphysics simulations. Modelica® is widely employed worldwide, mainly for aerospace and mechanical applications; in the recent years, it is being applied also for the modelling of large electrical grids [20] and for the cryogenic circuit for the cooling of superconducting magnets for fusion applications [21, 22, 23]. Considering its object-oriented nature, each component is modelled in a different object.

Several compilers and modelling environments are available, both commercial and free software; the two reference implementations are Dymola [24], a commercial implementation developed by Dassault Systèmes®, and OpenModelica [25], a free and open source implementation maintained by the Open Source Modelica Consortium (OSMC).

Being written explicitly for dynamic system modelling, Modelica® models are implicitly time-dependent, with a pre-defined time variable; all the simulations are then time-dependent (of course, steady-state simulations can be performed as well,

[3] Modelica® is a trademark of the Modelica Association.

as pseudo-transient or by computing a single timestep if no time-dependent equations are present). Both algebraic and ordinary differential equations (ODEs) in time can be written (simply by using operator `der`, which defines a time derivation), leading to a set of differential and algebraic equations (DAEs). If space derivatives are also present (partial differential equations, PDEs), they must be discretised by the user with any discretisation method (such as Finite Differences, Finite Elements or Finite Volumes), leading to algebraic equations.

In view of its declarative nature, Modelica® programming paradigm is different from traditional structured programming: the developer should only write the set of equations that describes the physics of the object, rather than the algorithm to solve such equations; the Modelica® compiler then allows choosing different solvers (implicit or explicit) for the resulting sets of DAEs. Modelica® compilers perform different optimization operations on the set of DAEs, such as solving simple equations analytically, index reduction, identification of redundant function calls, and many other, in order to reduce as much as possible the dimension of the sets of DAEs to be passed to the solver. The Modelica® code is then translated into a general-purpose programming language (usually C, but also C++ and Java can be used), which is compiled and executed.

Modelica® objects may contain connectors, which allow linking several models together; moreover, each (set of) model may be contained in another model at a larger scale, and so on with (in principle) infinitely many layers, ensuring a strong modularity of the developed code.

Further information about the Modelica® language can be found in [17].

2.2. Component models

2.2.1. Modelling assumptions

Being a system-level model, all the components are modelled according to a 1D Finite Volume (FV) approach for “long” components, such as pipes and cooling channels, and a 0D lumped parameter approach for components where there is no developed fluid flow; the choice of FV is driven by the simplicity of implementation it guarantees, still maintaining the global conservation of the required physical quantities. Since the code should enable the modelling of the entire tokamak with all the cooling channels in the PHTS, some simplifying assumptions had to be made in order to maintain the code speed. To this aim, a new, fully standard-compliant

Modelica® library has been developed, simplifying in particular the computation of the fluid properties to make it faster.

When water is considered as a working fluid, it is assumed to be an incompressible[4] liquid, with no phase change; in addition, the water specific heat, the water density and the derivative of the water internal energy with respect to the temperature, at constant pressure, are supposed to be linearly dependent on the temperature. These assumptions, while allowing very fast simulations, introduce a small error within the working range, with the inaccuracy on the said variables always below 2.5 % and below 1 % on average.

The helium case is even simpler, as it is well within the ideal gas range and, consequently, its specific heats can be considered constant with practically no error, and the density inversely proportional to the temperature through the ideal gas law; the pressure dependence of the density is neglected, in view of the very small pressure variations expected in normal operation. Moreover, also the helium flow can be considered incompressible, as the flow speed in nominal conditions is always much smaller than the sound speed (i.e. the Mach number is always smaller than 0.1).

To further increase the code speed, the heat transfer coefficient between the fluid and the solid structures in the FW, as well as the solid specific heat and density, are considered constant and fixed to the nominal values; in particular, the heat transfer coefficient is computed using the Dittus-Bölter correlation at nominal average conditions; this introduces an error always smaller than 4.5 % and below 2 % on average. Actually, the heat transfer coefficient may vary along the coolant flow path also because of other phenomena (e.g. acceleration of the fluid induced by heating, onset of nucleate boiling); such phenomena are however neglected in the model, in order to preserve its fast-running nature, considering also that they would *increase* the heat transfer coefficient, and neglecting them is a conservative assumption.

Overall, the error introduced by all of these assumptions does not affect the results by more than 3 % in steady-state nominal operation.

On the other hand, such assumptions cannot be valid anymore if accidental scenarios are of interest: if thinking about a water LOCA, for instance, it is clear that, in view of the huge pressure variation, water will flash and cannot be assumed to

[4] *i.e.* the term $\frac{\partial \rho}{\partial t}$ is neglected.

be always single phase liquid; in general, the operating range of the coolants would change strongly under accidental transients, invalidating previous assumptions. As a consequence, a separated module of the code was developed, allowing fast simulations of transients such as LOCAs: in this case, rather than simplifying the coolant modelling, the geometry is to be simplified, as the interest is no more focused on the detail of each channel, leading to a 0D modelling of the PHTS. Such module of the code is based on ThermoPower [26, 27], a free and open source Modelica® library developed by Politecnico di Milano for the modelling of power generation systems. In this case, the coolant behaviour is modelled more in detail: the coolant properties are taken from the Modelica® Standard Library, which implements the ideal gas model (with NASA coefficients) for helium and the International Association for the Properties of Water and Steam (IAPWS) Industrial Formulation '97 (IF97) water model [28].

2.2.2. Model equations (nominal operation)

In this section, the equations used by the GETTHEM models are reported; such equations are valid only when modelling nominal operating scenarios, whereas the equations for the models to be used for in-VV LOCA analysis are described in section 2.2.4 below.

1D helium models

The objects for HCPB which are modelled as 1D (i.e. the cooling channels) contain the implementation of the time-dependent mass, momentum and energy conservation equations (1)-(3) for each fluid FV *i*:

$$\dot{m}_{in,i} = \dot{m}_{out,i} \tag{1}$$

$$p_{in} - p_{out} = \Delta p_{friction} + \Delta p_{loc} \tag{2}$$

$$\dot{m}_i\left(h_{out,i} - h_{in,i}\right) = \dot{Q}_{m\to f,i} \tag{3}$$

where $\dot{m}_{in/out}$ is the inlet/outlet mass flow rate, $p_{in/out}$ is the inlet/outlet pressure, $\Delta p_{friction}$ is the pressure drop due to friction, Δp_{loc} is the localized pressure drop, $h_{in/out}$ is the inlet/outlet specific enthalpy of the fluid and $\dot{Q}_{m\to f}$ is the power going from the solid to the fluid. The time-dependent term in the continuity equation (1) is missing as consequence of the incompressibility assumption mentioned above, whereas the time-dependent term in the energy equation (3) is not reported, as the heat capacity of the helium is assumed to be always negligible with respect to the

solid coupled with it. The friction and localized pressure losses are computed according to equation (4):

$$\Delta p_{friction/loc} = \Delta p_{nom} \frac{\dot{m}}{\dot{m}_{nom}} \tag{4}$$

where Δp_{nom} is the nominal pressure drop across the component and $\dot{m}_{nom}$ is the nominal mass flow rate. The linear dependence of the pressure drop on the mass flow rate is not strictly valid for turbulent flow, which is found in the HCPB BB; however, the use of a linearized model (around the operating point) enables a much faster solution of the set of equations, at the expenses of a relatively small error on the mass flow rate distribution, which is estimated to be always below 5 % in the nominal conditions foreseen for BB operation.

1D water models

For each different channel of the WCLL, 1D mass, momentum and energy conservation equations are solved in each fluid FV of the spatial discretisation; in particular, mass and momentum equations have the same form as equations (1)-(2) above, whereas the energy conservation equation has an additional term accounting for the internal energy variation, which is not negligible as in the helium case:

$$A l_i \rho_i \left.\frac{\partial e_i}{\partial T}\right|_p \frac{\mathrm{d}T_i}{\mathrm{d}t} + \dot{m}_i \left(h_{out,i} - h_{in,i}\right) = \dot{Q}_{m \to f,i} \tag{5}$$

where A is the area of the channel cross section, l is the length of the FV, ρ is the fluid density, e is the fluid internal energy, T is the temperature and t is the time. Also, the pressure losses are computed according to a quadratic equation:

$$\Delta p = \Delta p_{nom} \left(\frac{\dot{m}}{\dot{m}_{nom}}\right)^2 \tag{6}$$

1D solid models

For the model of the structures around each fluid channel, 1D FV energy conservation is solved:

$$A_m l_i \rho_m c_m \frac{\mathrm{d}T_{m,i}}{\mathrm{d}t} = \dot{Q}_{in,i} - \dot{Q}_{m \to f,i} \tag{7}$$

$$\dot{Q}_{m\to f,i} = \left(T_{m,i} - T_i\right)\Omega l_i \mathrm{HTC} \tag{8}$$

where subscript m refers to the solid, c is the specific heat, $\dot{Q}_{in}$ is the input power in the FV, Ω is the heat transfer perimeter and HTC is the heat transfer coefficient.

The solid temperature computed by such model is necessarily the volume-averaged temperature inside each FV. However, when the structural temperature is of concern, the hot-spot temperature value is a more interesting piece of information with respect to the average value: in fact, the EUROFER operating range is limited to a maximum temperature of 550 °C, to avoid a sudden reduction in its creep strength [29]. To overcome this limitation of the model, a procedure is developed in order to compute the peak temperature in the postprocessing phase, exploiting information from more detailed models such as 3D CFD, as explained in Appendix A.

0D fluid models

For the 0D models, used for components such as heat exchangers, pumps and manifolds, mass and energy conservations are enforced, according to equations (9)-(10):

$$\dot{m}_{in} = \dot{m}_{out} \tag{9}$$

$$V\rho\frac{\mathrm{d}e}{\mathrm{d}t} = \dot{m}(h_{in} - h_{out}) + \dot{Q}_{in} \tag{10}$$

where V is the volume of the 0D object.

2.2.3. Breeding Blanket components

Helium-Cooled Pebble Bed[5]

The basic building block of the HCPB BB GETTHEM model is the BM object. It contains one FW model, one BZ model and two instances[6] of BM cap model (where the word *cap* refers to the top wall of the BM); moreover, it contains the models for the BM inlet and outlet manifolds, see Figure 2.2. The caps and the BZ are cooled

[5] Part of the work described in this section was also published in [11, 29].
[6] In object-oriented programming, the word *instance* refers to each distinct use of an object.

in parallel, with the caps assumed to work as two additional cooling plates, while for the FW cooling two alternative schemes are considered [6][7]:

- Integrated (HCPB-I), where the FW is cooled in series with caps/BZ, see Figure 2.1a;
- Separated (HCPB-S), where the FW is cooled by two additional dedicated loops, see Figure 2.1b.

In the HCPB-I scheme, applicable if the FW heat load is predictable and around 0.5 MW/m² [6], the FW receives the cold helium coming from the compressor, and the BZ and caps are cooled afterwards, in series with the FW (Figure 2.2); in the HCPB-S scheme, the BM objects contain only the BZ and caps (Figure 2.3a), while the FW is cooled by two other loops (Figure 2.3b), implemented as an object completely independent from the BM one.

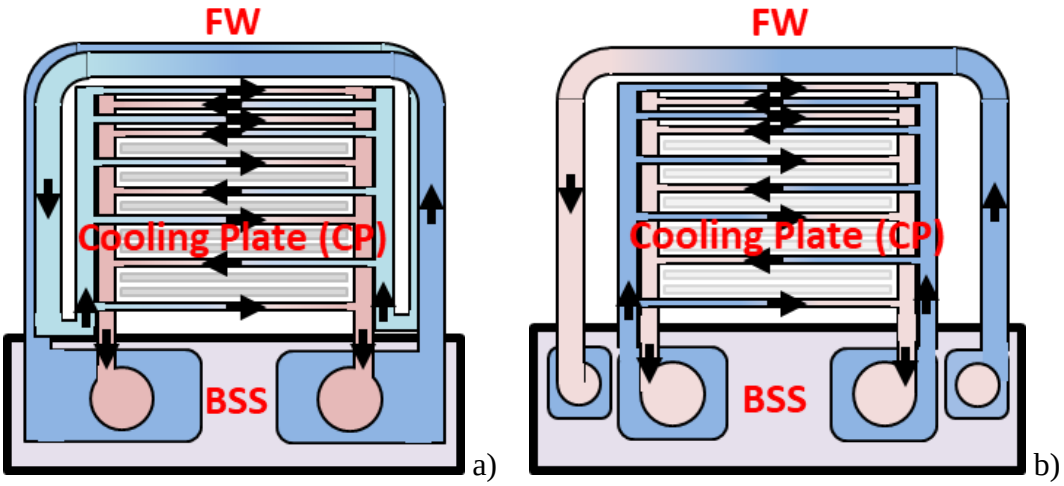

Figure 2.1: Possible alternatives for HCPB cooling: HCPB-I (a) and HCPB-S (b) (adapted from [6]).

[7] The HCPB-D, reported in [5], is hydraulically equivalent to the HCPB-S; the opportunity to have a water-cooled FW with the HCPB-D falls outside the scope of this work, so it is not considered here.

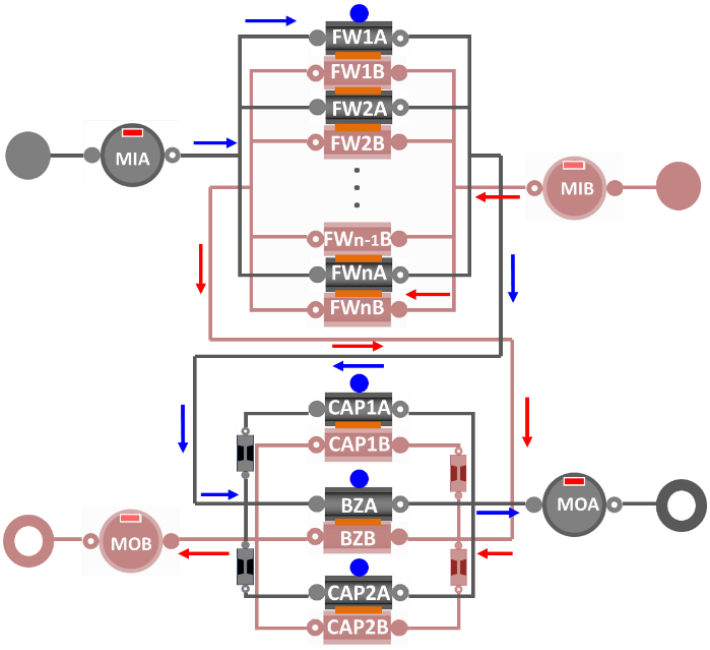

Figure 2.2: Sketch of the HCPB-I BM object (reproduced from [30]).

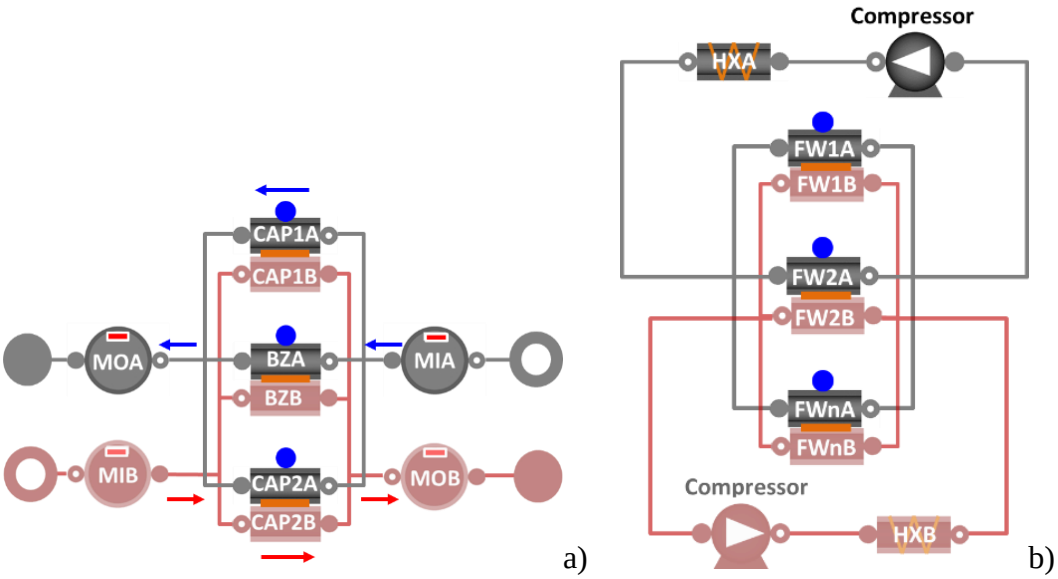

Figure 2.3: Sketch of the HCPB-S object: a) BM object for the main loops; b) object modelling the dedicated loops for FW cooling (reproduced from [30]).

Water-Cooled Lithium-Lead[8]

Since the WCLL cooling system is split in two separate loops, there is no BM object for WCLL, and the loops are directly connected to the FW and BZ objects, which are shown in Figure 2.4 and Figure 2.5. In both cases, the inlet connector of the FW/BZ is connected to the 0D model of the inlet manifold, which is in turn connected to the inlets of all the cooling channels in parallel; the channel outlets are then connected to the outlet manifold.

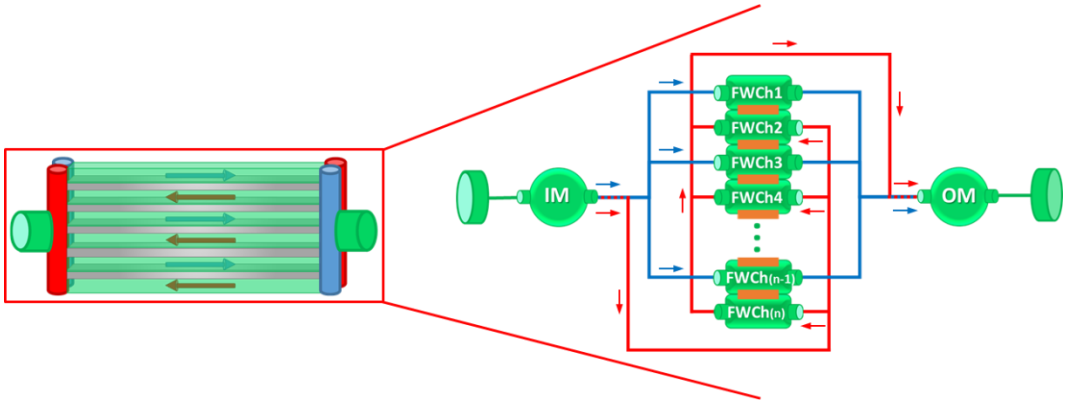

Figure 2.4: Sketch of the WCLL FW object (reproduced from [31]).

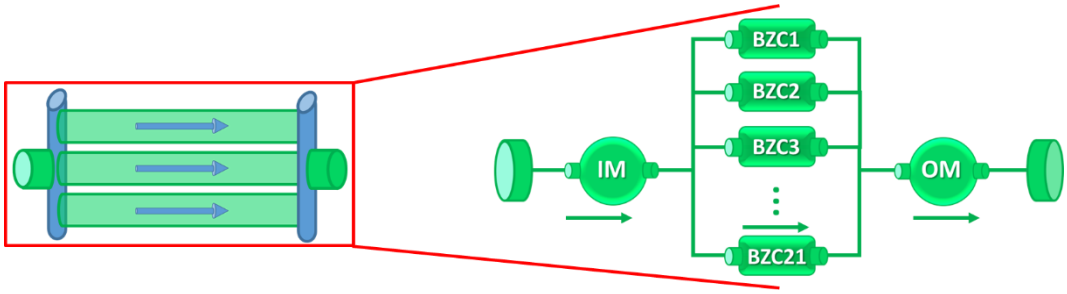

Figure 2.5: Sketch of the WCLL BZ object (reproduced from [31]).

HCPB and WCLL FW objects

The FW object contains several FW channels, including connectors for thermal coupling to the neighbouring channels in the twin circuit. A single FW channel object is composed of three channels in series: two side parts (heated by nuclear load and heat conduction from the BZ) and one front part, facing the plasma, heated by the plasma surface load, by nuclear heating and by conduction from the BZ. The

[8] Part of the work described in this section was also published in [30].

pipe bends are accounted for only as localized pressure drops. A schematic of a single FW channel object is shown in Figure 2.6 for the HCPB and in Figure 2.7 for the WCLL; in the WCLL case, an orifice model (i.e. a localized pressure drop) is added upstream the inlet of the channel, in order to allow redistributing the mass flow rate.

The FW channel models include also the solid EUROFER structures surrounding the channels, which are modelled as the channel walls; the solid volume surrounding each channel is split in two parts, see Figure 2.8, and each one is discretized using 1D FV in the flow direction. Inside each solid volume, equations (7) and (8) are solved: the solid transfers heat with the adjacent fluid volume, and is coupled with a conductive resistance with the solid volume belonging to the neighbouring channel, see Figure 2.8.

The parameters that can be tuned for both FW objects are reported in Table 2.1. The nominal values of mass flow rate and pressure losses are used inside equations (4) and (6) to compute the actual pressure drop within each channel; the wall thermal conductance is computed as $k_m/l_{\perp,m}$, where k_m is the metal thermal conductivity and $l_{\perp,m}$ is the length of the metal portion in the direction perpendicular to the fluid flow, where the two channels are coupled; finally, the wall heat capacity is computed as $c_m V_m \rho_m$, where c_m is the metal specific heat, V_m is the volume of the wall FV and ρ_m is the metal density.

The driver for the FW model is the heat load, i.e. the $\dot{Q}_{in,i}$ appearing in equation (7). This value can be different for all the channels and for all the FVs along a channel; starting from the total BM load, its distribution must be provided as a time-dependent 2D array, with (Nch, 3×Nv) elements, in terms of total input power (measured in W).

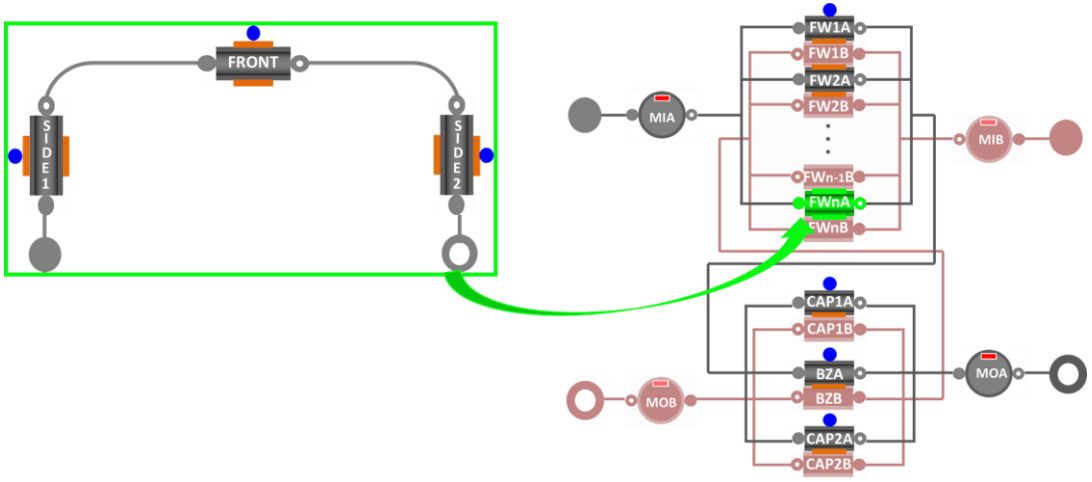

Figure 2.6: Sketch of a single HCPB FW channel object and relative position within the HCPB BM object. The orange rectangles represent the ports for the thermal coupling, while the blue circles represent the ports for the input loads (reproduced from [30]).

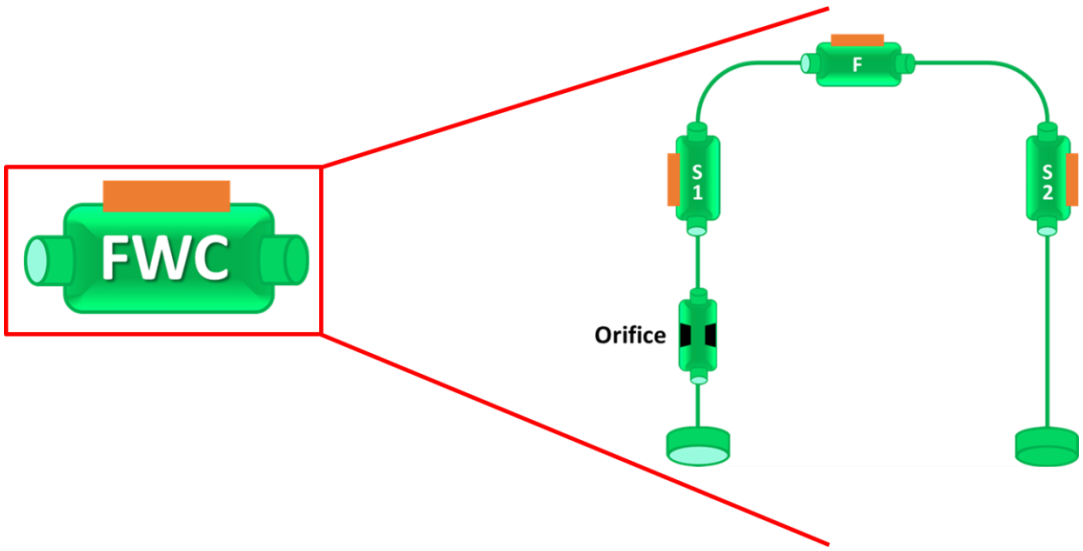

Figure 2.7: Schematic of a single WCLL FW channel object, including the inlet orifice. The orange rectangles represent the ports for the thermal coupling (reproduced from [31]).

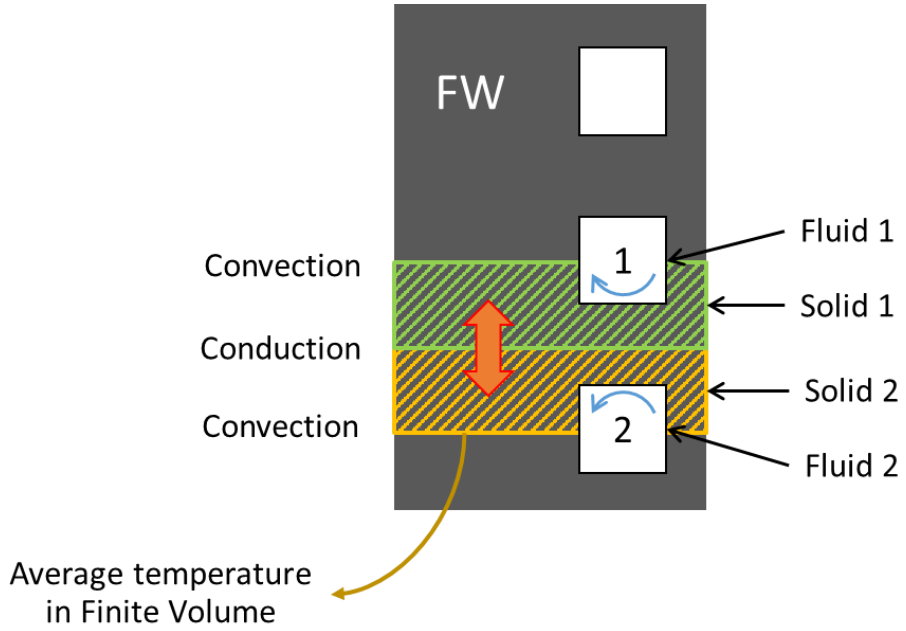

Figure 2.8: Definition of the solid domain in the FW objects.

Table 2.1: Input parameters of the HCPB and WCLL FW objects.

Name	***Description***	***Type***	***Unit***
Nch	Number of FW cooling channels	Scalar	-
Nv	Number of FVs in each portion of each channel	Scalar	-
dpnom	Nominal pressure loss across the FW	Scalar	Pa
dpnomOrifice (WCLL only)	Nominal pressure loss across the orifices	Vector (Nch elements)	Pa
wnom	Nominal mass flow rate	Vector (Nch elements)	kg/s
lambda	Heat transfer coefficient	Scalar	W/(m² K)
L_S	Length of the side portions of the channels	Vector (Nch elements)	m
L_F	Length of the front portions of the channels	Vector (Nch elements)	m
G_S	Thermal conductance of side channels' walls	Vector (Nch-1 elements)	W/K
G_F	Thermal conductance of front channels' walls	Vector (Nch-1 elements)	W/K
A	Cross section of the channels	Vector (Nch elements)	m²
Cm_S	Heat capacity of side channels' walls	Vector (Nch elements)	J/K
Cm_F	Heat capacity of front channels' walls	Vector (Nch elements)	J/K

WCLL BZ object

The WCLL BZ object, reported in Figure 2.5, contains a set of 1D channel models, according to the same scheme as in Figure 2.7; in this case, since the thermal coupling with the LiPb flowing outside the channels was not accounted for so far, all the channels are considered independent. The input parameters for the BZ objects are reported in Table 2.2. As for the FW, the nominal values of mass flow rate and pressure losses are used inside equation (6) to compute the actual pressure drop within each channel; since no thermal coupling between adjacent channels is accounted for, there are no parameters related to the solid structures or the heat transfer between solid and fluid.

Also in this case the driver is the heat load $\dot{Q}_{in,i}$, to be provided as a time-dependent 2D array, with (Nch, 3×Nv) elements, in terms of total input power (measured in W).

Table 2.2: Input parameters of the WCLL BZ object.

Name	***Description***	***Type***	***Unit***
Nch	Number of FW cooling channels	Scalar	-
Nv	Number of FVs in each portion of each channel	Scalar	-
dpnom	Nominal pressure loss across the FW	Scalar	Pa
dpnomOrifice	Nominal pressure loss across the orifices	Vector (Nch elements)	Pa
wnom	Nominal mass flow rate	Vector (Nch elements)	kg/s
L_S	Length of the side portions of the channels	Vector (Nch elements)	m
L_F	Length of the front portions of the channels	Vector (Nch elements)	m
A	Cross section of the channels	Vector (Nch elements)	m^2

HCPB BZ and BM cap objects

Inside the HCPB BZ object (Figure 2.9a) there are several instances of CP objects for the CP modelling. Each CP object (Figure 2.9b) contains models for the cooling channels, as well as connectors for inter-channel coupling with the countercurrent circuit, inside the same CP (the heat transfer among adjacent CPs through the Li_4SiO_4 and Be pebble beds is currently neglected).

The BM cap object (Figure 2.10) is structurally identical to the CP; connectors for thermal coupling between channels in the twin circuits are provided inside the cap objects. As with the WCLL FW, an orifice model (i.e. a localized pressure drop) is added upstream the cap channels, see Figure 2.2.

Similarly to the FW objects, the solid structures are modelled in the HCPB CP objects as the channel walls, according to a 1D FV approach in the flow direction. Considering the presence of the dummy channels, as explained in section 1.2.1 above (see Figure 1.6), only the solid volume in between two active (i.e. non-dummy) channels is split in two ways, depending on the number of dummy channels, as shown in Figure 2.11. The surfaces of the dummy channels are assumed as adiabatic.

Also in this case the driver is the heat load $\dot{Q}_{in,i}$, to be provided as a time-dependent 2D array, with (Nch, Nv) elements, in terms of total input power (measured in W).

The input parameters for the HCPB CP and cap objects are reported in Table 2.3.

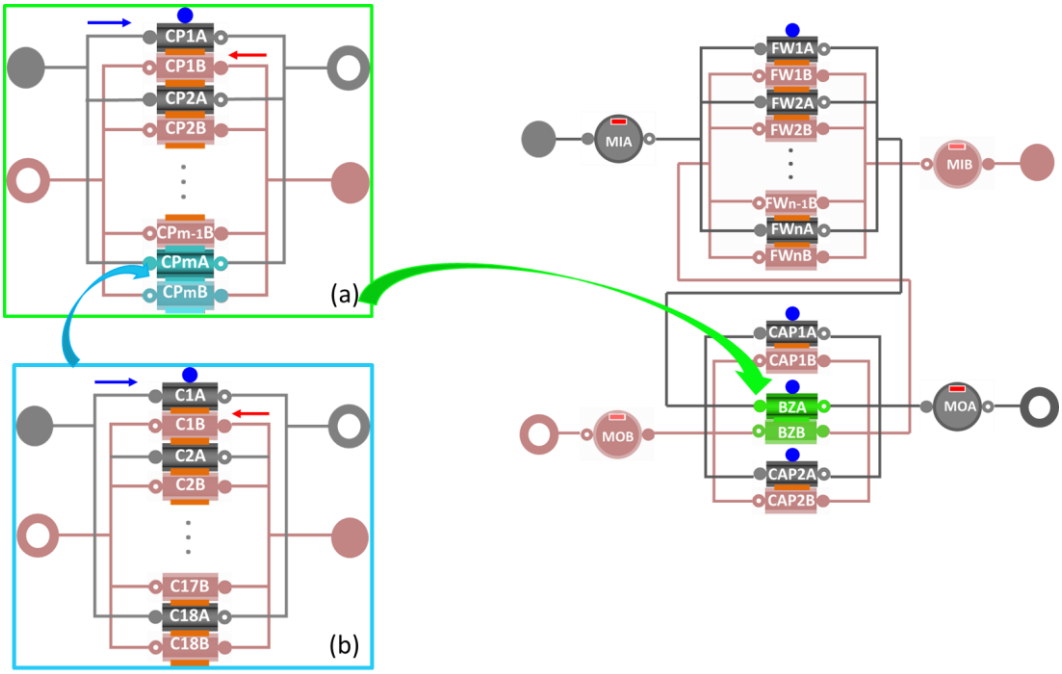

Figure 2.9: Sketch of a HCPB BZ object and its position in the HCPB BM object: a) the BZ object contains several CP objects; b) each CP object contains several cooling channels ("C" objects). The orange rectangles represent the ports for the thermal coupling, while the blue circles represent the ports for the input loads (reproduced from [30]).

Manifolds

All the manifolds inside the BM, as well as the ex-vessel manifolds, are modelled using 0D objects according to equations (9)-(10), as the presence of many inlets and outlets does not allow the flow to fully develop. Heat loads and pressure drops are neglected. For these 0D lumped parameter models, the only parameter is the manifold volume.

A more detailed, 1D model of the manifolds in the HCPB BSS is nevertheless under development [32], exploiting the results of 3D CFD simulations; such model should also be experimentally validated in the HELOKA facility at KIT.

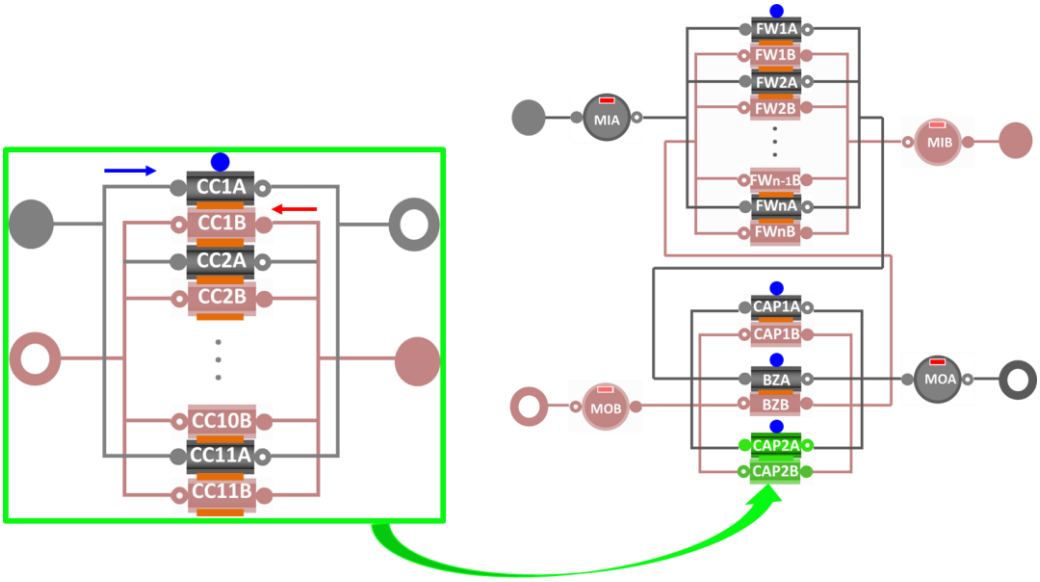

Figure 2.10: Sketch of a HCPB BM cap object, containing several cooling channels ("CC" objects) and its position in the HCPB BM object (reproduced from [30]).

Table 2.3: Input parameters of the HCPB CP and cap objects.

Name	***Description***	***Type***	***Unit***
Nch	Number of cooling channels per CP	Scalar	-
Nv	Number of FVs in each channel	Scalar	-
dpnom	Nominal pressure loss across the FW	Scalar	Pa
dpnomOrifice (cap only)	Nominal pressure loss across the orifices	Vector (Nch elements)	Pa
wnom	Nominal mass flow rate	Vector (Nch elements)	kg/s
lambda	Heat transfer coefficient	Scalar	W/(m² K)
L	Length of the channels	Vector (Nch elements)	m
G	Thermal conductance of the channels' walls	Vector (Nch-1 elements)	W/K
A	Cross section of the channels	Vector (Nch elements)	m²
Cm	Heat capacity of the channels' walls	Vector (Nch elements)	J/K

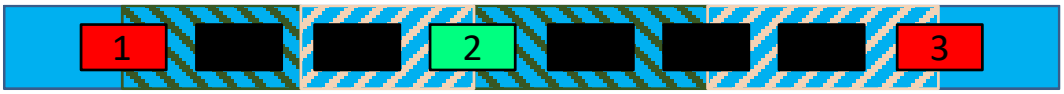

Figure 2.11: Cross section of a CP, showing the split of the solid volume between adjacent channels, in the two possible cases: when the number of dummy channels between two active channels is even or 0 (as for channels 1-2), and when it is odd (as for channels 2-3). The colour code is the same as Figure 1.6 (reproduced from [13]).

2.2.4. Vacuum Vessel Pressure Suppression System components[9]

The GETTHEM models for the EU DEMO VVPSS (Figure 1.13) components are developed with the aim of allowing a rapid modelling of an in-VV LOCA, caused by a break in the FW which translates into a release of the FW coolant inside the VV. Because of the huge pressure difference between the PHTS (at 15.5 MPa for water or 8 MPa for helium) and the VV (~mPa at maximum), a break in the FW necessarily produces choked flow and, in the case of water, also flashing. Note that the presence of choked flow in fact limits the fluid velocity at the break, thus de-coupling the VV dynamics from the PHTS dynamics; the use of isolation valves (IVs) in the BB cooling loops is currently under investigation by the EUROfusion Work Package BoP, in order to limit the inventory of released materials.

Inside the VV, heat transfer between the coolant and the solid structures takes place; due to the high temperatures on the BB and VV structures, ice formation (in the case of water) on the VV walls is not taken into account [33]. After the break, the BB coolant rapidly fills the VV, increasing its pressure, which reaches the set point value for the operation of the BVs in a relatively short time.

At this point, the BVs open and start discharging the coolant inside the EV or SP, but, being dimensioned for small leakages, they may not be effective in removing the coolant from the VV if a large in-vessel break occurs, and the pressure in the VV continues increasing. After some time, also the BDs open and the coolant is removed from the VV also by the Relief Lines (RLs). Depending on the relative sizes of break and of the RLs, the pressure may continue to increase inside the VV while the coolant flow rate to the EV/SP increases, finally reaching and overcoming the flow rate entering the VV from the PHTS (which is on the other hand decreasing as the PHTS empties) and thus effectively reducing the pressure inside the VV. As with the break, choked flow occurs at the BDs and BVs, at least during the initial part of the transient, when the pressure difference between the VV and the EV/SP

[9] Part of the work described in this section was also published in [34, 35].

is very large. After some time, the pressures will be more similar and the flow will not be choked anymore; the time when this limit is passed depends substantially on the type of valve used.

Finally, in the EV and SP, helium expansion or vapour condensation will take place, respectively. Depending on the design of the VVPSS, the EV and SP may have some cooling strategies in order to reduce the temperature and pressure reached at the end of the transient (*e.g.* presence of room-temperature water inside the EVs or external cooling by natural convection) – this may be particularly useful for the helium EV, in order to reduce its temperature and consequently its volume, while at the same time removing some of the radioactive elements (such as tritium).

In order to have a fast model, all the components (including the PHTS) are modelled with a 0D lumped-parameters approach; the only exception is the RL model, which is a 1D FV fluid flow model with a small number of nodes, as neglecting the pressure drop in the RL would result in a non-conservative assumption. Although the 1D model of the PHTS presented above might be used, the choice of a 0D model for the in-VV LOCA analyses is justified considering the choked flow occurring at the break, which, by limiting the flow rate, makes the timescale relevant for 1D localized effects in the PHTS much larger than the characteristic times of the transient.

All the models which are presented in the following are directly taken or based on the mentioned ThermoPower library; further details on such models may then be found in [26, 27]; although the models share the same structure, the different behaviour of water and helium during a LOCA calls for a different modelling of the phenomena; hence, the models are presented separately, starting with the models for the HCPB and continuing with the models for the WCLL.

PHTS, VV and EV models for the HCPB

The PHTS, VV and EV are modelled as 0D constant-volume tanks. In these models, conservation of fluid mass and energy are imposed using equations (11) and (12), respectively:

$$\frac{\mathrm{d}m}{\mathrm{d}t} = \sum \dot{m}_{in} - \sum \dot{m}_{out} = V\frac{\partial \rho}{\partial t} \tag{11}$$

$$\frac{\mathrm{d}E}{\mathrm{d}t} = \frac{\partial (me)}{\partial t} = \sum \dot{m}_{in} h_{in} - \sum \dot{m}_{out} h_{out} - \dot{Q}_{ext} \tag{12}$$

where V is the volume, m and E are the total mass and energy inside the volume, respectively, $\dot{m}_{in/out}$ are the inlet/outlet mass flow rates, ρ is the helium density, e is the helium specific internal energy and $h_{in/out}$ are the helium specific enthalpies at inlet/outlet. The specific kinetic and potential energy terms at inlet/outlet are neglected, and the control volume is considered fixed (i.e., no variation of potential and kinetic energy inside the control volumes are computed). Moreover, no mechanical organs are present in the model and no phase change may happen, since the working fluid is a homogeneous gas. The models include in principle the possibility to apply external thermal sources or sinks $\dot{Q}_{ext}$ on all the components, which may represent, for instance, the decay heat deposition in the BB structures and in-VV cooling loop or the effect of a cooling strategy in the EV, such as the above-mentioned water mass.

At the start of the simulation, all the volumes are assumed to be filled with helium at the initial conditions of pressure and temperature.

Break and pressure drop models for the HCPB

The break in the FW is modelled as a 0D localized pressure drop, solving equation (13):

$$\dot{m} = A\sqrt{\frac{2\rho\Delta p_{eff}}{K}} \tag{13}$$

where A is the cross section of the break, K is the localized pressure loss coefficient, ρ is the helium density and Δp_{eff} is the effective pressure loss which is computed in order to account for choked flow: if $p_{in}/p_{out} < \left(p_{in}/p_{out}\right)_{crit}$ then $\Delta p_{eff} = p_{in} - p_{out}$, otherwise $\Delta p_{eff} = p_{in} - p_{crit}$. The only input parameters for this model are A and K, while the critical pressure ratio $\left(p_{in}/p_{out}\right)_{crit}$ is a characteristic of the fluid which depends on the specific heats at constant pressure and volume only; the values of K used in the present work are all taken from literature, as referenced in sections 3 and 4.3 below.

Burst disk and bleed valve models for the HCPB

The BDs and BVs are modelled as 0D valves (according to the ANSI/ISA-75.01 standard [34]) that open when the pressure drop across the component is higher than a threshold value Δp_{thresh}, according to equation (14):

$$\dot{m} = \begin{cases} 0 & until\ \Delta p < \Delta p_{thresh} \\ AY\sqrt{\rho x_{eff} p_{in}} & when\ \Delta p \geq \Delta p_{thresh} \end{cases} \tag{14}$$

where Δp_{thresh} and A are parameters which can be set independently for each instance of the model, and p_{in} is the pressure at inlet; the compressibility factor Y and the effective pressure drop ratio x_{eff} are determined according to equations (15) and (16), respectively:

$$Y = 1 - \frac{|x_{eff}|}{3F_k x_T} \tag{15}$$

$$x_{eff} = \begin{cases} \dfrac{\Delta p}{p_{in}} & if\ \dfrac{\Delta p}{p_{in}} < F_k x_T \\ F_k x_T & if\ \dfrac{\Delta p}{p_{in}} \geq F_k x_T \end{cases} \tag{16}$$

where the ratio of specific heat factor F_k is defined as $\gamma/1.4$ ($\gamma = c_p/c_v$is the ratio of specific heats of the gas) and the terminal pressure drop ratio x_T is a parameter depending on the valve type. The product $F_k x_T$ is called *critical ratio*.

The valves are assumed to open instantaneously; this assumption can be easily relaxed, although the effect of a delayed opening of the valve is negligible considering the relevant timescales of the process. After being opened, they cannot close, even if the pressure drop falls again below the threshold.

Relief line model for the HCPB

As mentioned the RLs are modelled with a 1D FV approach, using only few nodes to avoid slowing down the model. It solves the dynamic mass, momentum and energy conservation equations, as reported in equations (17)-(19):

$$\dot{m}_{in} - \dot{m}_{out} = \sum_i \frac{\mathrm{d}m_i}{\mathrm{d}t} = A \sum_i l_i \left(\left.\frac{\partial \rho_i}{\partial p}\right|_T \frac{\mathrm{d}p_i}{\mathrm{d}t} + \left.\frac{\partial \rho_i}{\partial T}\right|_p \frac{\mathrm{d}T_i}{\mathrm{d}t} \right) \tag{17}$$

$$\frac{L}{A}\frac{\mathrm{d}\dot{m}}{\mathrm{d}t} + p_{out} - p_{in} + \Delta p_{friction} = 0 \tag{18}$$

$$A l_i \rho_i c_{v_i} \frac{\mathrm{d}T_i}{\mathrm{d}t} + \dot{m}_i \left(h_{out,i} - h_{in,i}\right) = \dot{Q}_{in,i} \quad \forall i \tag{19}$$

where c_v is the helium specific heat at constant volume and the friction term is computed (assuming turbulent flow) using Colebrook's correlation.

PHTS and VV models for the WCLL

The PHTS and VV are modelled as 0D constant volume tanks also in the water case (but including models for the metal walls), in which mass and energy conservation equations in the fluid (20)-(21) and the energy conservation equation in the solid (22) are imposed:

$$\frac{\mathrm{d}m}{\mathrm{d}t} = \sum \dot{m}_{in} - \sum \dot{m}_{out} = V\left(\frac{\partial \rho}{\partial p}\Big|_h \frac{\mathrm{d}p}{\mathrm{d}t} + \frac{\partial \rho}{\partial h}\Big|_p \frac{\mathrm{d}h}{\mathrm{d}t}\right) \tag{20}$$

$$\begin{aligned}\frac{\mathrm{d}E}{\mathrm{d}t} = h\frac{\mathrm{d}m}{\mathrm{d}t} + m\frac{\mathrm{d}h}{\mathrm{d}t} - V\frac{\mathrm{d}p}{\mathrm{d}t} \\ = \sum \dot{m}_{in}h_{in} - \sum \dot{m}_{out}h_{out} + S(T_m - T_w)\mathrm{HTC}\end{aligned} \tag{21}$$

$$C_m \frac{\mathrm{d}T_m}{\mathrm{d}t} = S(T_w - T_m)\mathrm{HTC} + \dot{Q}_{ext} \tag{22}$$

where HTC is the heat transfer coefficient between walls and fluid (a parameter), S is the surface area of the walls (a parameter), $T_{m/w}$ is the temperature of wall/water, respectively, $\dot{Q}_{ext}$ is the external heat source/sink and C_m is the wall heat capacity.

The presence of two-phase state is considered by the evaluation of the water quality from equation (23):

$$x = \frac{h - h_l}{h_v - h_l} \tag{23}$$

where x is the water quality and $h_{v/l}$ is the specific enthalpy at vapour/liquid saturations conditions (dew/bubble point).

Break and isolation valve model for the WCLL

As described above, choked flow of water occurs across the break, leading to flashing as the downstream pressure is much lower than the saturation pressure. Consequently, a model for a valve for flashing liquid is used, according to the ANSI/ISA-75.01 standard [34], both for IV and break. The model solves the following equations:

$$\dot{m} = A\sqrt{\rho \Delta p_{eff}} \tag{24}$$

$$\Delta p_{eff} = \begin{cases} p_{in} - p_{out} & if\ (p_{in} - p_{out}) \leq \Delta p_{ch} \\ \Delta p_{ch} & if\ (p_{in} - p_{out}) > \Delta p_{ch} \end{cases} \quad (25)$$

$$\Delta p_{ch} = 0.81(p_{in} - F_F p_v) \quad (26)$$

$$F_F = 0.96 - 0.28\sqrt{\frac{p_v}{p_c}} \quad (27)$$

where Δp_{ch} is the choked pressure drop, F_F is the liquid critical pressure ratio factor, p_v is the vapour pressure of the liquid at the inlet temperature, p_c is the critical pressure of the liquid (which, for water, is 22.1 MPa). In the break model, the valve is followed by a localized pressure drop, modelled as described below[10].

Pressure drop, burst disk, bleed valve models for the WCLL

The models used for the pressure drop, BD and BL share the same structure used for helium: consequently, also the water pressure drop model solves equation (13) above, while BD and BL models solve equations (14)-(16) above (as the mentioned ANSI/ISA standard does not distinguish between two phase or steam flows and gas flows [34]).

Relief line model for the WCLL

As for the helium model, the RLs are modelled with a 1D FV approach, solving the dynamic mass, momentum and energy conservation equations, as reported in equations (28)-(30):

$$\dot{m}_{in} - \dot{m}_{out} = \sum_i \frac{\mathrm{d}m_i}{\mathrm{d}t} = A \sum_i l_i \left(\left.\frac{\partial \rho_i}{\partial p}\right|_h \frac{\mathrm{d}p_i}{\mathrm{d}t} + \left.\frac{\partial \rho_i}{\partial h}\right|_p \frac{\mathrm{d}h_i}{\mathrm{d}t} \right) \quad (28)$$

$$\frac{L}{A}\frac{\mathrm{d}\dot{m}}{\mathrm{d}t} + p_{out} - p_{in} + \Delta p_{friction} = 0 \quad (29)$$

$$A l_i \rho_i \frac{\mathrm{d}h_i}{\mathrm{d}t} + \dot{m}_i \left(h_{out,i} - h_{in,i}\right) - A l_i \frac{\mathrm{d}p_i}{\mathrm{d}t} = \dot{Q}_{in,i} \quad \forall i \quad (30)$$

[10] Note that this is different from the helium case, where the break was modelled as a pressure drop only: this is needed as the water pressure drop model cannot account for choked flow and flashing.

Suppression Pool model

The SP is modelled as a 0D constant volume tank containing a two-phase mixture always in equilibrium conditions (i.e. the temperature of the coolant inside the SP is always the saturation temperature). Inside this volume, conservation of mass and energy are imposed, as per equations (31) and (32) shown below:

$$\sum \dot{m}_{in} = \frac{\mathrm{d}V_l}{\mathrm{d}t}\rho_l + V_l\frac{\partial \rho_l}{\partial p}\frac{\mathrm{d}p}{\mathrm{d}t} + \frac{dV_v}{dt}\rho_v + V_v\frac{\partial \rho_v}{\partial p}\frac{\mathrm{d}p}{\mathrm{d}t} \tag{31}$$

$$\sum \dot{m}_{in}h_{in} + \dot{Q}_{ext} = m_l\frac{\partial h_l}{\partial p}\frac{\mathrm{d}p}{\mathrm{d}t} + \frac{\mathrm{d}m_l}{\mathrm{d}t}h_l + m_v\frac{\partial h_v}{\partial p}\frac{\mathrm{d}p}{\mathrm{d}t} + \frac{\mathrm{d}m_v}{\mathrm{d}t}h_v \tag{32}$$

where $V_{l/v}$ is the volume occupied by the liquid/vapour phase, $\rho_{l/v}$ is the density of the saturated liquid/vapour and $m_{l/v}$is the mass of the liquid/vapour phase.

The sum of the first two terms on the right-hand side of equation (31) represents the variation of the mass of liquid in the SP: the first term is the contribution due to the variation of liquid volume inside the tank (considering the density constant) and the second term takes into account the variation of density (considering the liquid volume constant). The same approach is followed in the last two terms of equation (31) for the vapour phase. Simultaneously, the first two terms on the right-hand side of equation (32) represent the variation of energy stored in the liquid phase, decomposed in two terms: the first one accounts for the variation of specific enthalpy, while the second one for the variation of the stored mass. The same approach is also followed for the vapour phase, leading to the last two terms of equation (32).

Finally, equation (33) evaluates the vapour quality in the SP:

$$x = \frac{m_v}{m_v + m_l} \tag{33}$$

It is important to note that the assumption of thermodynamic equilibrium in the SP is non-conservative. In fact, this is equivalent to assume that a fraction of the steam that reaches the SP condenses immediately at contact with water, until the inlet mixture reaches the same thermodynamic condition of the SP (i.e. infinite condensation rate). On the other hand, this does not affect sensibly the computation of the mass flow rate from the VV to the SP that, in turn, is one of the main drivers for the pressure evolution in the VV (which is the object of the present work); this assertion is also verified looking at the validation results, see section 3.4 below.

2.3. Component assembly

2.3.1. Modules for HCPB and WCLL nominal operation analysis[11]

To build the complete model for the transient analyses in nominal operation, the different models are assembled together: for the HCPB, considering the mentioned alternatives HCPB-I and HCPB-S, two different solutions are possible, according to the scheme under investigation. For the HCPB-I, 7 instances of BM objects are connected in a parallel to the inlet and outlet manifolds (MI/MO), which are in turn connected to the cooling trains (i.e. compressor and heat exchanger), see Figure 2.12. For the HCPB-S, instead, two different loops are to be used: the BZ loop has the same structure as in Figure 2.12 (but the BM model now contains only BZ and caps, as in Figure 2.3a), while an additional loop is used for the FW cooling, as in Figure 2.3b.

For the WCLL, as mentioned, two different loops are anyway foreseen for FW and BZ cooling; since the two loops are assumed to be independent (the coupling is provided by the LiPb which is not modelled, see section 2.2.3 above), two separate objects are used, as sketched in Figure 2.13. The FW (or BZ) object is then simply connected to the cooling train model, including a pump and a HX (for the FW loop) or a steam generator (for the BZ loop).

In both cases, the ex-vessel components have not been developed yet, so they are currently substituted by fixed pressure boundary conditions (BCs), as shown in Figure 2.12 and Figure 2.13.

[11] Part of the work described in this section was also published in [11, 29, 30].

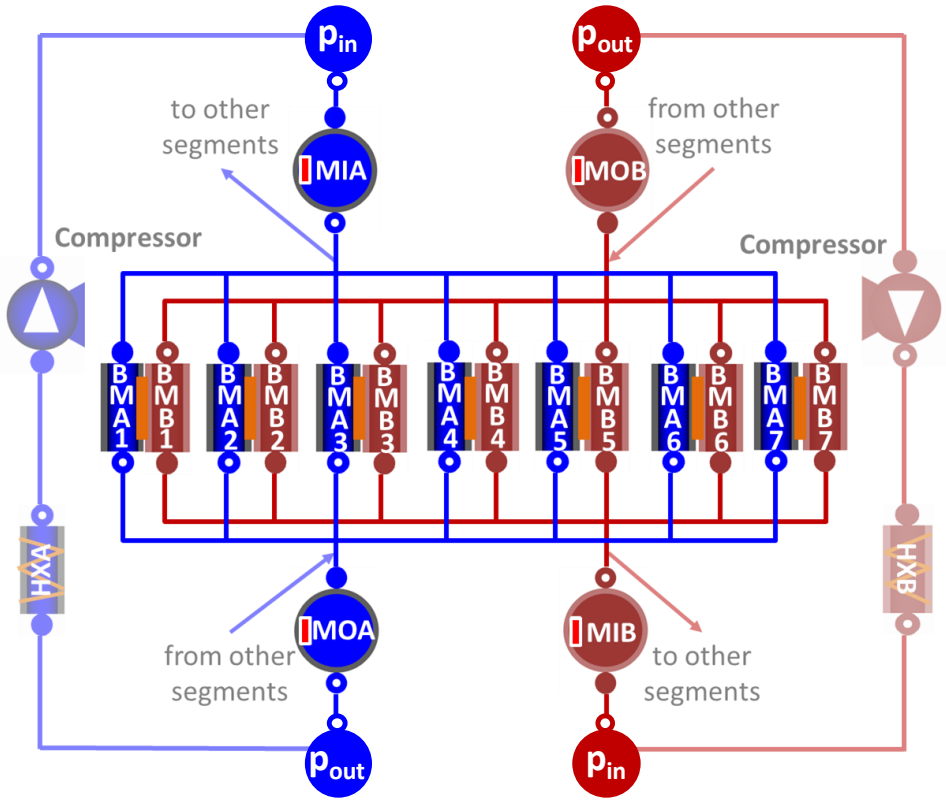

Figure 2.12: GETTHEM model of the HCPB-I cooling system: the ex-vessel components (greyed-out), not yet modelled, are substituted by fixed pressure BCs (represented by the circles p_{in}/p_{out}). MIA/MIB: Inlet Manifold, loop A/B; MOA/MOB: Outlet Manifold, loop A/B (reproduced from [13]).

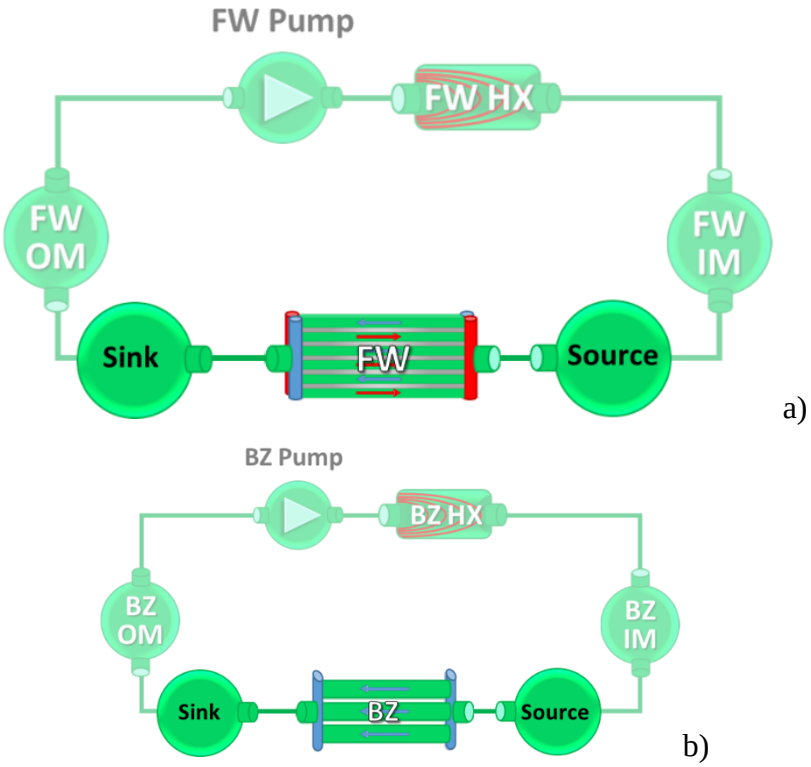

Figure 2.13: GETTHEM model of the WCLL cooling systems: FW PHTS (a) and BZ PHTS (b). The ex-vessel components (greyed-out), not yet modelled, are substituted by fixed pressure BCs (represented by the circles "Source"/"Sink").

2.3.2. Vacuum Vessel Pressure Suppression System module[12]

In a similar fashion, the models described in section 2.2.4 above are connected together in order to build the complete module for the in-VV LOCA analysis, including the VVPSS model. According to the system layout as shown in Figure 1.13, the PHTS 0D model is connected through the break model to the VV model which, in turn, is connected to the VVPSS by the BDs and BVs, both attached to the RLs. Finally, the 1D RL models are attached to the final sink, which is the EV for the HCPB and the SP for the WCLL. The two models are reported in Figure 2.14.

[12] Part of the work described in this section was also published in [34, 35].

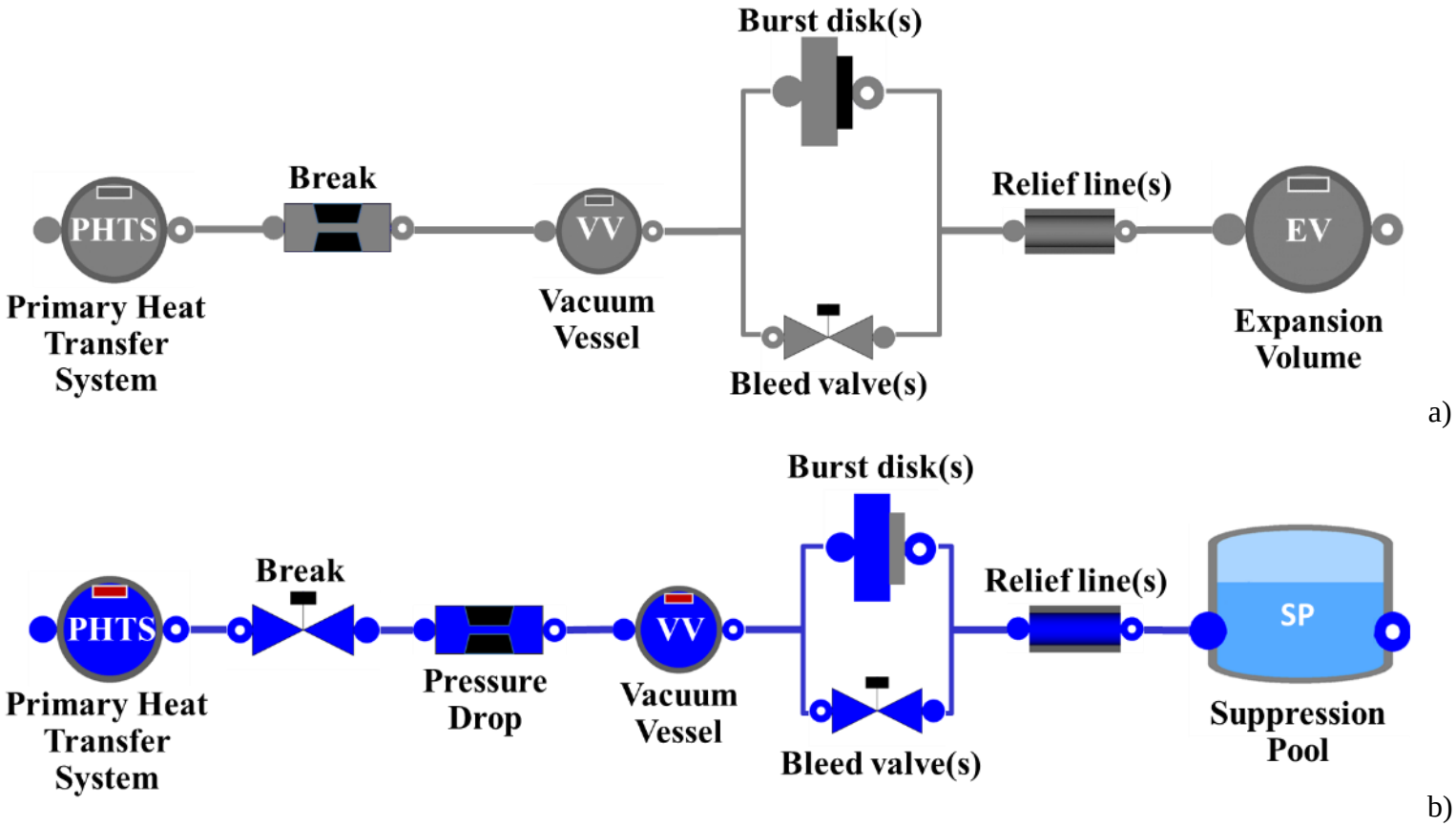

Figure 2.14: GETTHEM models for the in-VV LOCA analysis, for the HCPB (a) and the WCLL (b) (adapted from [35, 36]).

In the case of the HCPB, considering that different loops are available to cool the FW, the case where the coolant is released by more than one loop is also considered; to this aim, two instances of PHTS and break models are used, see Figure 2.15, and the size of PHTS and break are determined according to the initiating event. Also, for the WCLL, the opportunity to have IVs is taken into account: for such scenarios, the PHTS model is split in two parts connected by an IV model, as shown in Figure 2.16; the size of the two PHTS objects is in this case determined based on the position of the IVs. The use of IVs for the helium-cooled BB concepts is not currently considered, as several analyses with different codes [35, 37, 38, 39, 40] have shown that the timescales in this case are too fast for any active system to intervene.

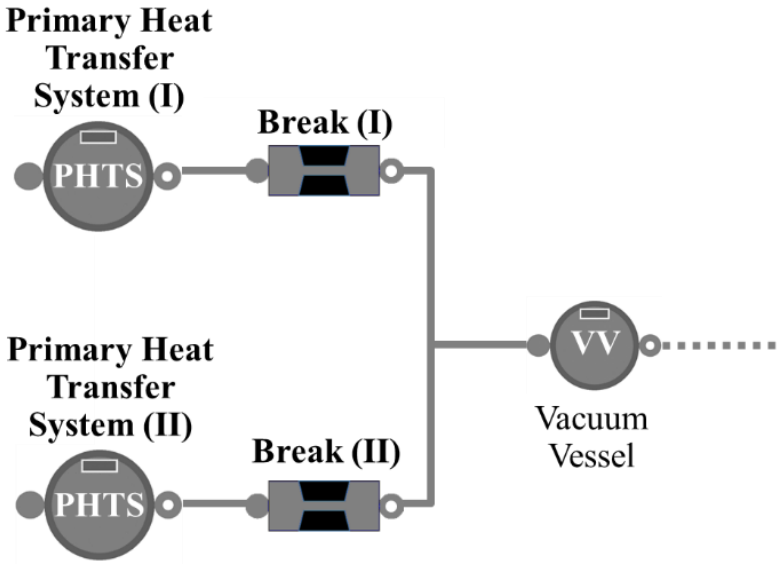

Figure 2.15: Detail of the GETTHEM model for helium in-VV LOCA analysis, when coolant is released by two loops. Downstream the VV, the model is identical to that sketched in Figure 2.14a.

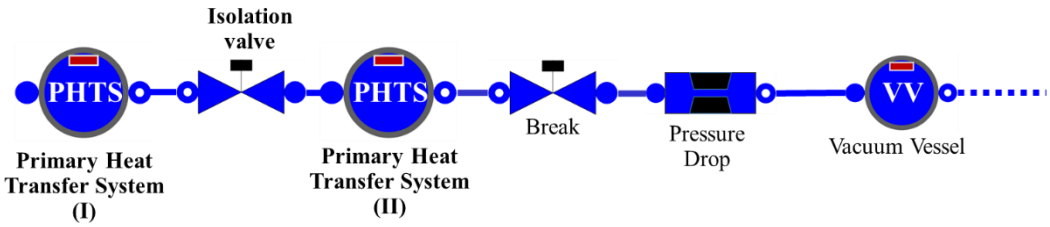

Figure 2.16: Detail of the GETTHEM model for water in-VV LOCA analysis, when IVs are present. Downstream the VV, the model is identical to that sketched in Figure 2.14b.

Chapter 3

GETTHEM benchmark and validation

Before any newly developed model can be trustfully applied to any kind of real system, it is mandatory to check if its computations are comparable in some way with the actual phenomena it is modelling. This comparison should be done against experimental results, if available, in order to directly have an idea of the accuracy of the model with respect to the physical phenomenon; this procedure is called *(experimental) validation*.

On the other hand, however, experimental results may not be available due to different reasons (phenomenon hard or expensive to reproduce, unavailability of the hardware, …); in this cases, the model capabilities can still be checked against other models which may already have been validated. This procedure is called *benchmark.*

In this section, the benchmark of the developed GETTHEM models against other tools, which are well-known in the nuclear field, is presented, both under nominal operation and accidental transients; for the case of a water in-VV LOCA, the model validation against experimental results is presented as well. A verification of the 1D fluid water model is reported in Appendix B.

3.1. Benchmark in normal operation: HCPB[13]

The GETTHEM model of the HCPB cooling system is benchmarked against the 3D CFD study performed by the HCPB design team, described in [7] and detailed in [12, 41, 42], see Figure 3.1.

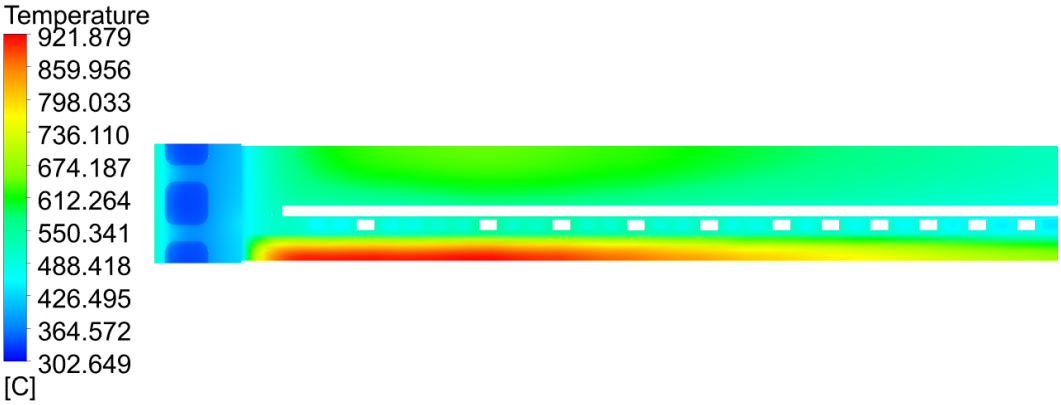

Figure 3.1: Results of the HCPB 3D CFD study (reproduced from [41]).

Considering the computational burden needed for 3D CFD simulations, the mentioned CFD analysis was carried out on a unit slice at the midplane of the OB4 BM (including one and "two halves" of FW channels and one CP, as shown in Figure 3.2), with symmetry conditions on the top and bottom surfaces. In order to be consistent with the CFD analysis, only the GETTHEM results at the OB4 mid-plane are here compared with the CFD results. It is also important to recall that GETTHEM does not model the Be and Li_4SiO_4 layers, as well as the purge gas duct used to collect the tritium produced therein; in particular, the first ones do not affect the steady-state temperature, whereas the effect of the latter was shown in [42] to be negligible. In addition, no coupling between FW and CP is accounted for in GETTHEM, to avoid excessive computational efforts.

The heat load drivers for this benchmark are the plasma surface heating on the FW, assumed to be poloidally uniform and equal to 500 kW/m², plus the power generation in the BZ, computed by neutronic analyses and having a radial distribution according to a radial power peaking factor $f_p^Q(r) = \frac{Q(r)}{\overline{Q}}$ (reported in Figure 3.3), where $Q(r)$ is the radial profile of the power generation and $\overline{Q}$ is the average power generation.

[13] Part of the work described in this section was also published in [11].

The CFD results are here postprocessed by computing the volume-averaged temperature in the EUROFER around each CP cooling channel; such temperature value is compared with the average EUROFER temperature computed by GETTHEM. The result is shown in Figure 3.4, including the error bars which, for GETTHEM, refer to the 3 % error estimation mentioned in section 2.2.1 above, whereas for the CFD refer to an estimated maximum error of 5 K, as reported in [12]. The mass flow rate distribution among the channels is obtained in GETTHEM introducing orifices at the inlet of the channels, and setting their localised pressure drop coefficients in order to reproduce the mass flow rate distribution (as the manifold model in GETTHEM is 0D, it could not produce different mass flow rates to the channels). This has the aim to minimize the hydraulic differences between the two models, to have a fair benchmark on the thermal prediction and, in particular, on the hotspot temperature estimation.

Figure 3.4 shows that, while the CFD temperature distribution is non-monotonic (despite the power generation profile is exponentially decreasing from the FW to the BSS, Figure 3.3), the GETTHEM one is monotonically decreasing following the power generation. The non-monotonic behaviour of the CFD curve can be due to several reasons: the first local minimum found in channels 5-6 lies in the region close to the FW, so that part of the heat deposited in the BZ is conducted to the FW and removed by its cooling channels. The local maximum found in channels 14-15 is due to how the coolant distributes among the cooling channels (see the mass flow rate distribution reported in Figure 3.4), which has a minimum in that region, causing a reduction of the cooling power. The last local maximum in channels 25-26 is located in a region where the active cooling channels suddenly rarefy, i.e. where the number of dummy channels between active ones rises from one to three (see also Figure 1.6).

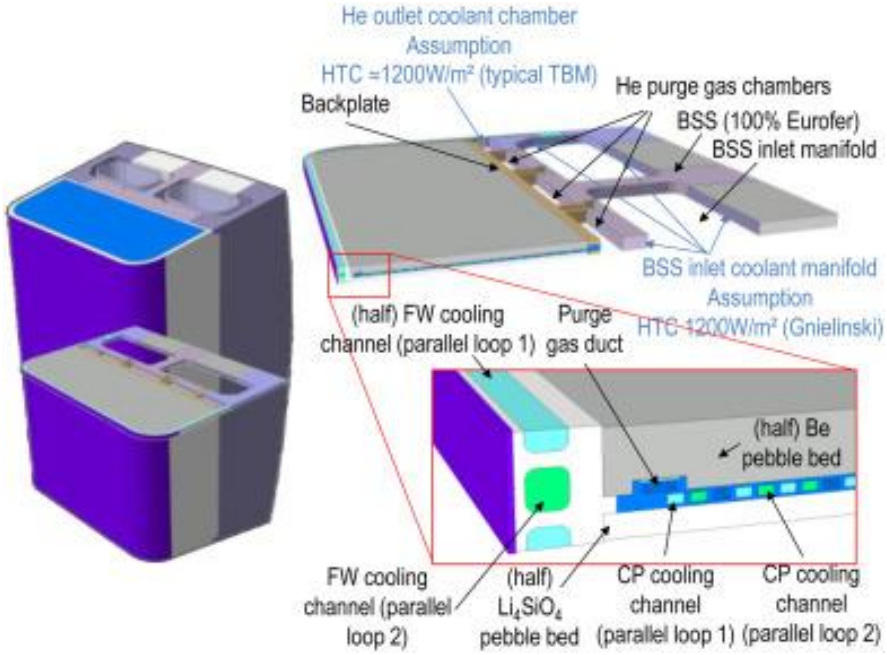

Figure 3.2: HCPB CFD computational domain (reproduced from [7]).

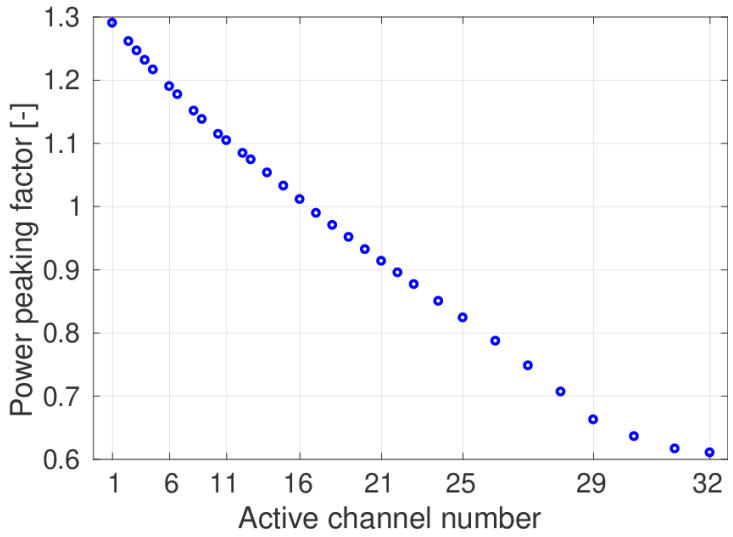

Figure 3.3: Radial distribution of the power peaking factor for the HCPB BZ heat load (reproduced from [13]).

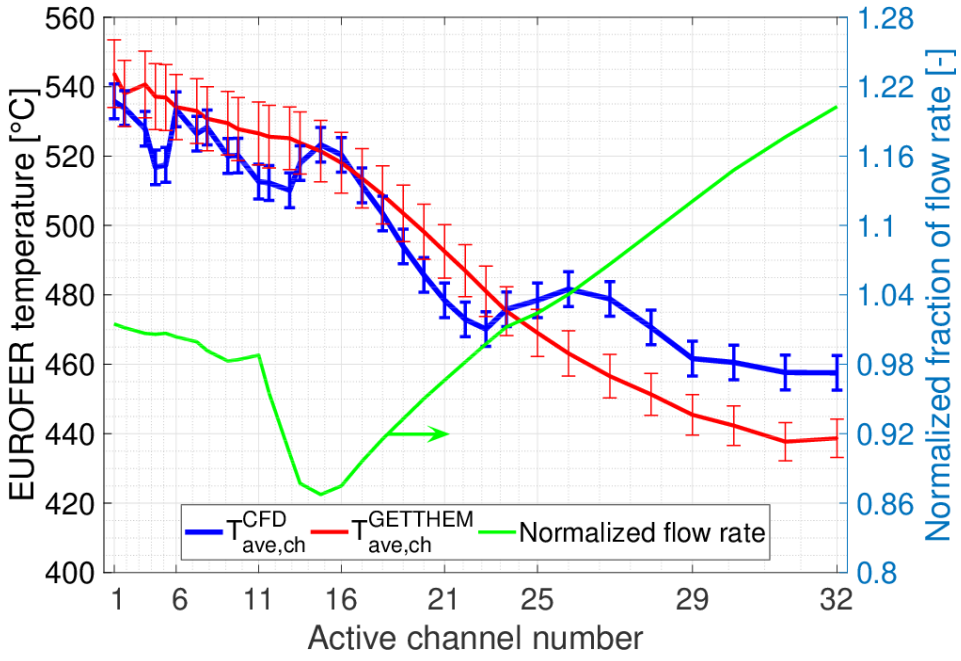

Figure 3.4: Left axis: radial distribution of the average temperature in the EUROFER surrounding the CP cooling channels, as computed by CFD (thick blue line) and GETTHEM (thin red line); right axis: radial distribution of the He mass flow rate (normalized to the average) among the CP cooling channels (GETTHEM and CFD curves are superimposed, hence only one is shown). Reproduced from [13].

The temperature profile computed by GETTHEM, on the other hand, must follow the power generation profile, and consequently it is monotonically decreasing from the FW towards the BSS. The first minimum discussed above cannot be present in the GETTHEM results, as the coupling with the FW cooling system is not accounted for. The maximum in channel 15 is also not present, despite the fact that GETTHEM computes the same mass flow rate distribution as the CFD; the reason behind such discrepancy is explained considering that in the CFD model a mass flow rate reduction has two effects (with the same sign) on the solid temperature: from an energy balance point of view, a lower mass flow rate means a larger coolant temperature increase; on the other hand, it also reduces the HTC between solid and fluid, further increasing the solid temperature. The effect on HTC cannot be seen in the GETTHEM results, as the HTC is assumed constant (see section 2.2.1 above). The third maximum found in the CFD results cannot be found in GETTHEM as well, since the thermal resistance used to couple adjacent channels is computed only according to the EUROFER volume around the channel (i.e. the dummy channels are not modelled, as mentioned); this also explains the larger discrepancy between the two studies closer to the BSS: the larger number of dummy channels makes the

lumped-parameter modelling used by GETTHEM a worse approximation of the 3D heat conduction.

In any case, the relative discrepancy between the two models is always smaller than 10 % and below 5 % on average. Moreover, this error is larger in the region close to the BSS, where the solid temperature is expected to be lower, for the reasons discussed above.

The GETTHEM results are then postprocessed to reconstruct the hot-spot solid temperature, by applying a shape factor (determined from the reference 3D CFD study) as described in Appendix A.

The hot-spot temperatures in the FW and BZ regions as predicted by GETTHEM are compared in Table 3.1 to the hot-spot temperatures computed by CFD, showing an error below 1 %; in the same table, also the accuracy of GETTHEM for the coolant thermal-hydraulics is evident.

Table 3.1: Benchmark of GETTHEM calculations against 3D CFD on the HCPB; the discrepancy is computed with respect to the temperature increase (reproduced from [13]).

Variable	***GETTHEM***	***CFD*** [12, 42]	***Discrepancy***
$T_{\mathrm{He,out}}$	466 °C	471.2 °C	3 %
$T_{\mathrm{max,EUROFER,FW}}$	515 °C	514.4 °C	0.3 %
$T_{\mathrm{max,EUROFER,BZ}}$	554 °C	556.6 °C	1 %

3.2. Benchmark in normal operation: WCLL[14]

Concerning the WCLL normal operating conditions, the GETTHEM models for the BZ are compared against the 3D CFD studies [43, 44] performed by the WCLL design team [31]. The reference CFD study focused on the BZ of a single elementary cell, see Figure 3.5; in particular, the simulation included the LiPb, water (both in the BZ and FW loops) and solid structure domains, with the power generation inside the LiPb computed from a neutronic calculation; the load to the FW was also considered, due to a heat flux from the plasma equal to 500 kW/m², plus a nuclear load on the FW (the Nuclear Wall Load, NWL) determined again from neutronic analyses. The presence of both loops and LiPb means that, in principle, some of the power deposited in the BZ may be removed by the FW loop or vice-versa, or even by the LiPb itself.

[14] Part of the work described in this section was also published in [30].

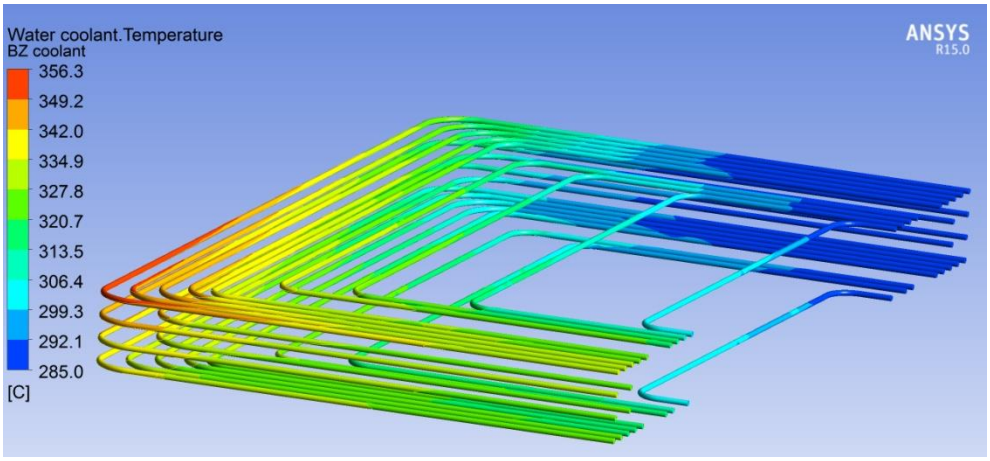

Figure 3.5: Results of the WCLL 3D CFD study (reproduced from [14]).

Since GETTHEM does not model the LiPb, the latter is only accounted for as a power source to the coolant flowing inside the channels. Consequently, the two loops are completely independent (as described in section 2.2.3 above), meaning that in GETTHEM all the power generated in the BZ is removed by the BZ water and not by the LiPb, and also that no heat is transferred to the FW loop.

According to [44], the total BZ heat load on the elementary cell is 283 kW, distributed in the radial direction as an exponential *in the LiPb*, with a peaking factor defined as $e^{-\lambda r}$, where r is the radial coordinate centred on the FW and the factor λ is estimated as $2\ln(10)$ m^{-1}, from the total neutron flux reported in [44], leading to the peaking factor distribution as in Figure 3.6a. The flowing LiPb actually modifies this power distribution in the radial direction, but, since this cannot be modelled in GETTHEM, it is not considered here, thus introducing another difference with respect to the reference CFD calculation.

Since the channels inside the BZ region are distributed unevenly in order to have more cooling power close to the plasma, the load *to each channel* has then been scaled according to the LiPb volume around it, leading to the power distribution reported in Figure 3.6b (resulting in a distribution that does not follow an exactly exponential behaviour).

The imposed BCs are of inlet pressure and temperature and outlet pressure. In particular, at the inlet the nominal values of pressure and temperature have been set (p = 15.5 MPa, T = 285 °C), while at the outlet the pressure value has been imposed in order to reproduce the nominal pressure drop expected within the BZ in nominal conditions, equal to 7.7 kPa [44].

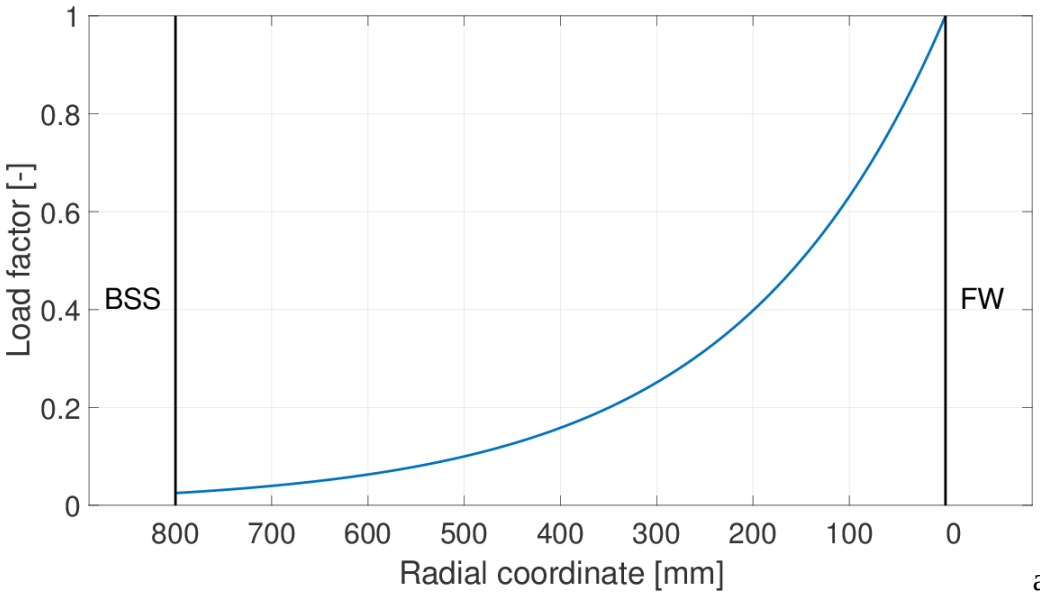

a)

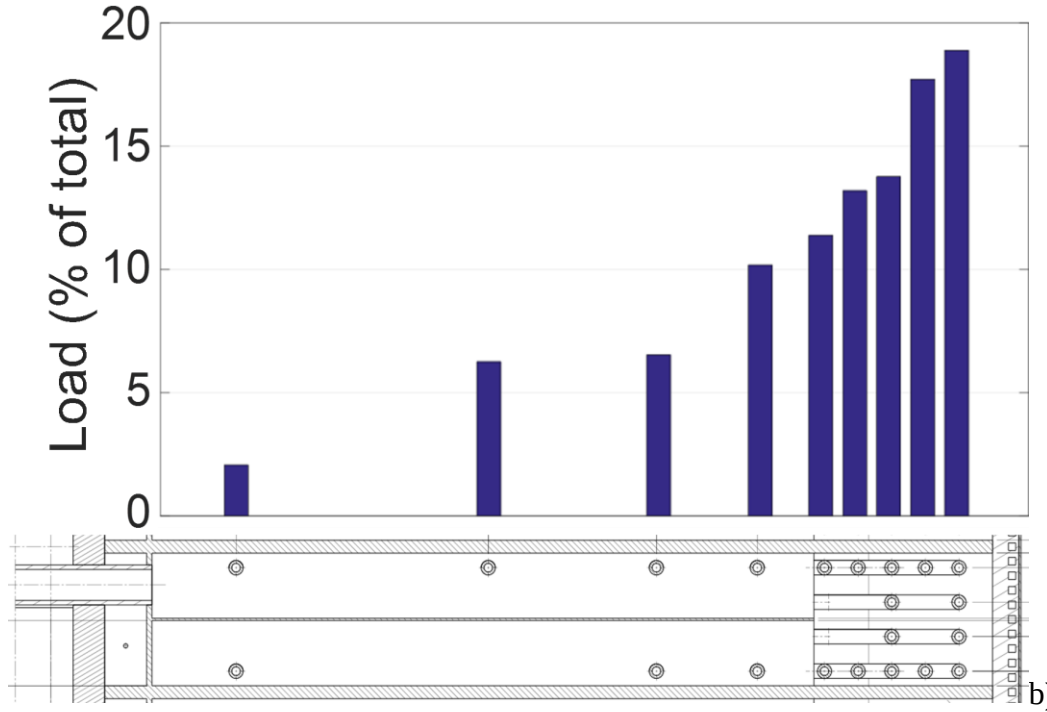

b)

Figure 3.6: a) Distribution of the WCLL power peaking factor derived from neutron flux; b) resulting radial power distribution in a WCLL elementary cell (adapted from [31]).

Finally, in the reference CFD calculation the mass flow rate distribution among the 21 channels of the elementary unit is uniform and each of them carries 50 g/s; in GETTHEM, the same result was achieved by suitably setting the nominal pressure drop of the orifices at the inlet of the channels. Of course, this is sub-optimal

from the temperature distribution point of view, as the most loaded channels will need a larger cooling power to maintain the same outlet temperature of the least loaded (and, consequently, a larger flow rate). However, since the aim at this point is only to verify the capabilities of the tool, a uniform flow rate distribution has been used.

Figure 3.7 reports the temperature distribution along the flow path for four selected channels of the elementary unit. As expected, the temperature increase is different from channel to channel: in fact, the channels face different heat loads $\dot{Q}_{in}$, as per Figure 3.6, but have the same flow rate $\dot{m}$; looking at the steady-state energy balance $\dot{Q}_{in} = \dot{m}(h_{out} - h_{in})$ it is evident how the outlet enthalpy h_{out} (and, consequently, the outlet temperature) must be different for the different channels. Anyway, the temperature always remains below the saturation point, which, at 15.5 MPa, is ~344 °C.

The part of the channels running in the toroidal direction, being closer to the plasma, experiences a higher heat load; this becomes of course more evident as the channels get closer to the plasma side (and, consequently, longer), as it is evident for instance for channel #8, which shows a larger slope in its central part.

Figure 3.8 reports the 2D temperature distribution in the radial-toroidal plane, showing how the coolant temperature is in general increasing as the channels get closer to the plasma; however, it is also evident how the outlet temperature is far from being uniform, with some channels overcooling the BZ and some others reaching much higher temperatures.

These results reflect with acceptable accuracy those of the CFD reference case, as reported by Table 3.2, thus confirming at least qualitatively the validity of the model, which gives an error of ~8 % on average on the outlet temperature. This error is partly due to the simplifying assumptions done for the computation of the fluid property, but the most important error source is certainly the approximation on the heat load described above; in fact, the radial distribution of the power used in this simulation is a very rough approximation of the power transferred to the coolant. The flowing LiPb changes the exponential behaviour at least because of two effects: first, it will have different temperature values along its path, because of heat advection; second, its flow through the bank of tubes of the elementary cell will affect its heat transfer coefficient with the water tubes, because of its different speed and thermophysical properties. Consequently, a heat load distribution better

representing the actual heat transfer between the LiPb and the coolant would improve the overall code performances. Moreover, GETTHEM tends to underestimate the outlet temperature: this is justified by the fact that, in the reference CFD simulation, the LiPb outlet temperature is ~315 °C, lower than the inlet temperature of 326 °C (which is also the design LiPb outlet temperature) [45], meaning that the power seen by the water is actually larger than the external heat generation, as the LiPb is overcooled. This effect cannot be seen by GETTHEM, as it does not model the LiPb.

For the model verification, the results highlight the energy conservation in GETTHEM: in fact, the total power to the coolant at steady-state, computed as $\sum_j \dot{m}_j(h_{out,j} - h_{in})$, where the index j counts the channels, is exactly equal to the 283 kW of power in input.

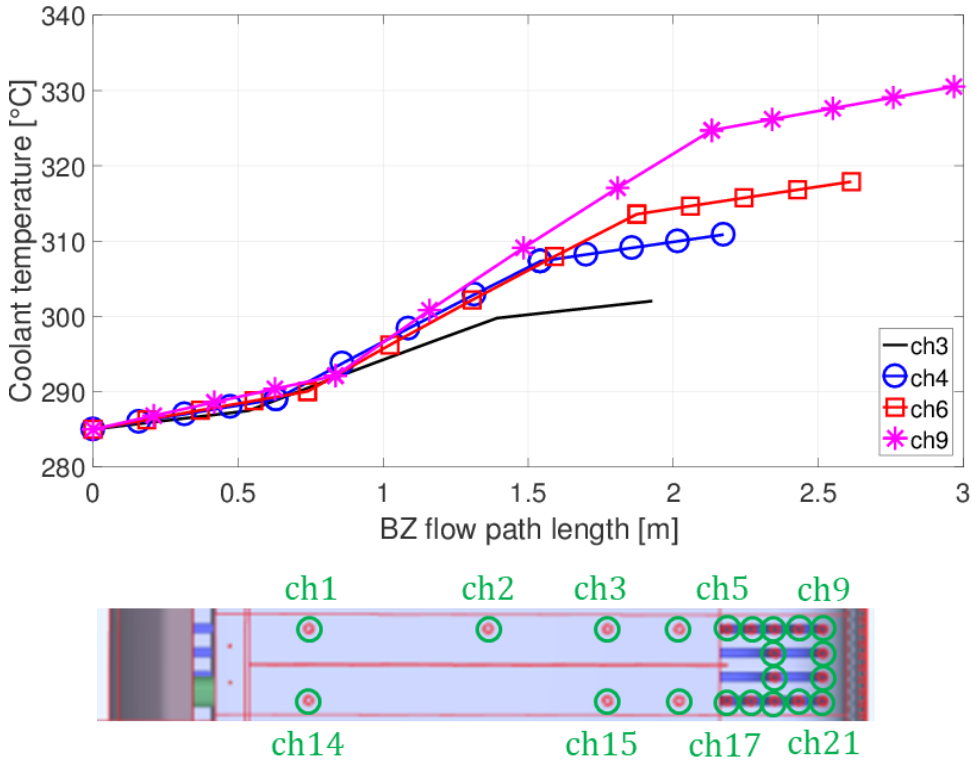

Figure 3.7: Computed 1D profile along four selected cooling channels out of the 21 of an elementary unit of the WCLL OB segment (adapted from [31]).

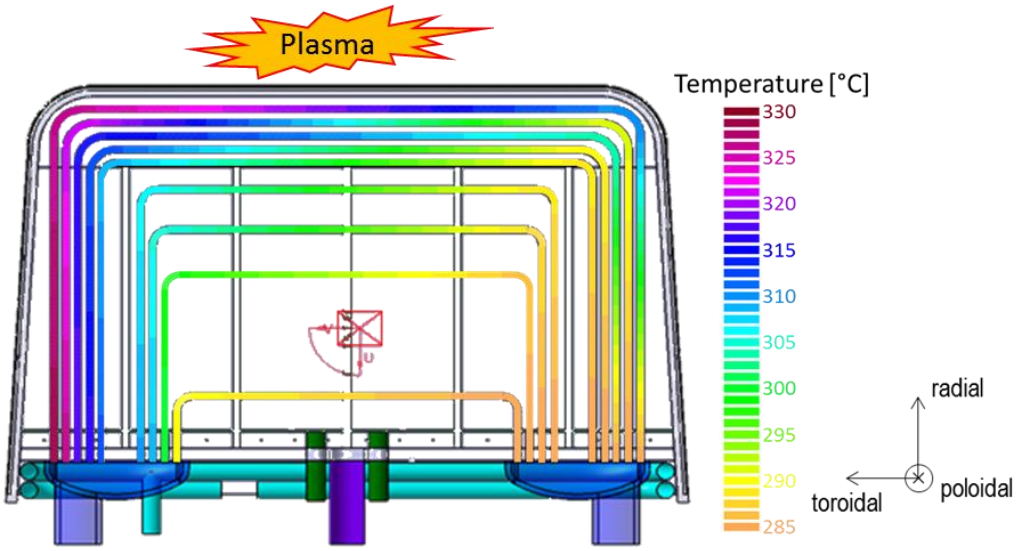

Figure 3.8: Distribution in the radial-toroidal plane of the coolant temperature for an elementary unit of the WCLL OB segment (adapted from [31]).

Table 3.2: Comparison between the WCLL BZ outlet temperatures computed by GETTHEM and those obtained by CFD (adapted from [31]).

Channel	***GETTHEM temperature increase [°C]***	***CFD model temperature increase [°C]*** [44]	***Relative error in temperature increase [%]***
1-14	5.9	5.4	9.5
2	16.0	16.2	-1.2
3-15	24.3	21.6	13
4-16	25.3	28.3	-11
5-17	28.1	33.0	-15
6-18	32.2	30.2	6.7
7-10-12-19	33.4	35.1	-4.6
8-20	42.1	40.7	3.4
9-11-13-21	44.6	50.6	-12

3.3. Benchmark in accidental conditions: HCPB[15]

The VVPSS model for the HCPB described in section 2.3.2 above is initially calibrated against the results coming from the first scenario simulated in [39] by Sapienza Università di Roma with the validated CONSEN code; the only difference between the two models is how BVs and BDs are modelled.

For the calibration phase, the critical ratio $F_k x_T$ of the GETTHEM BD and BL models is tuned in order to reproduce in the best possible way the evolution of the pressure inside the VV. Successively, the calibrated parameters of the model are frozen and the GETTHEM model is benchmarked against CONSEN with the results obtained for a different scenario, reported in [39]. Table 3.3 shows the value of the input parameters which are kept constant in both the situations mentioned above (calibration and benchmark scenarios), as used in CONSEN and GETTHEM codes.

Table 3.3: Value of the parameters used in the CONSEN in-VV LOCA analysis for helium-cooled BBs [39] (reproduced from [35]).

PHTS	
Volume [m³]	2325
Initial pressure [MPa]	8
Initial temperature [K]	673
Break	
Cross section [m²]	0.2
Localized pressure loss coefficient	5
VV	
Volume [m³]	2243
Initial pressure [μPa]	5
Burst disks	
Opening differential pressure* [MPa]	0.15
Localized pressure loss coefficient	3.5
Bleed valves	
Opening differential pressure* [MPa]	0.09
Localized pressure loss coefficient	3.5
EV	
Volume [m³]	120000
Initial pressure [kPa]	4.2

* These values are assumed to be equal to the ITER VVPSS.

[15] Part of the work described in this section was also published in [34].

The only parameters that differ between the two scenarios analysed here are the break size and the number of BLs and RLs, as well as their cross section (see Table 3.4). In the calibration scenario, these parameters are assumed to have the same values as in the ITER VVPSS, while in the benchmark scenario the total flow area is designed in order to ensure a maximum pressure value inside the VV lower than the pressure limit (0.2 MPa) [39].

All the data relative to CONSEN in the following results are extracted from the digitalization of the figures in [39].

Table 3.4: Value of the parameters used in the helium in-VV LOCA calibration and benchmark scenarios (reproduced from [35]).

	Calibration scenario*	***Benchmark scenario***
Bleed lines		
Number	2	1
Cross section [m²]	0.1	1.5
Relief lines		
Number	1	1
Cross section [m²]	1	6.5

* These values are assumed to be equal to the ITER VVPSS.

3.3.1. Calibration results

Figure 3.9 and Figure 3.10 show the comparison between GETTHEM and CONSEN in terms of evolution of the pressure and temperature, respectively, as computed inside the three considered volumes (PHTS, VV and EV) during the transient until steady state is reached.

The maximum pressure value reached inside the VV is 911 kPa at 3.6 s from the break, whereas the steady state pressure value (which is, as expected, equal for all the three volumes) is 150 kPa; this pressure value confirms what was expected from the analytical estimation performed in [39]. The transient lasts about 80 s. As mentioned, in this scenario the parameters of the GETTHEM BD and BL models have been calibrated in order to reproduce as well as possible the CONSEN results during all the transient; consequently, the two models predict the same peak and steady-state pressure, with an error at peak below 0.2 %. In addition, the time when the peak is reached is correctly reproduced by GETTHEM. The transient is predicted to be faster by GETTHEM, with an error on the timescale of the VV pressure decay smaller than 9 %, which anyway translates to a slight underestimation of the

overall duration of the transient (below 1 %). This is due to the different model used for the BDs and BLs, which are modelled as localised pressure drops in CONSEN, while they are modelled as valves inside GETTHEM.

The temperature evolution is again very similar in the two codes. The maximum temperatures reached in VV and EV are 1125 K and 1016 K, respectively. The peak temperature in the VV is found at ~0.1 s after the break, while in the EV it is reached after ~3.6 s. The steady-state temperature value reached in the VV is ~200 K, while the EV settles at 739 K. Of course, the three volumes reach three different values of temperature, as they have the same pressure but different volumes, thus reaching different temperatures as per the ideal gas law. The same error on the transient time-scale is found here, although it is less evident if looking at the overall transient duration, as GETTHEM temperature evolution is almost overlapping with the CONSEN one.

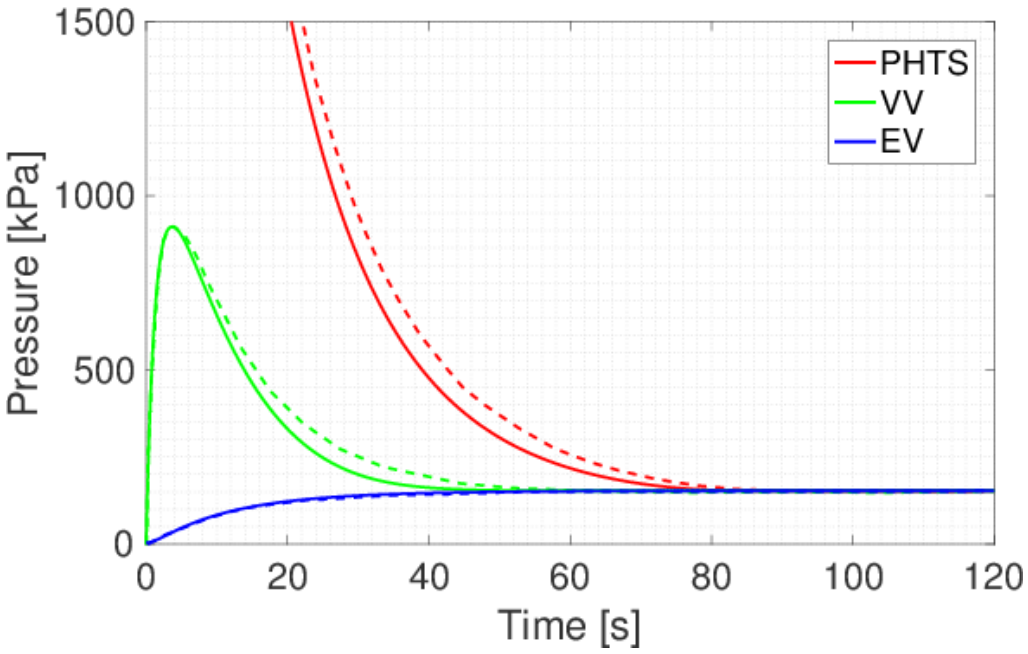

Figure 3.9: Evolution of the pressure in the three volumes of the helium VVPSS model in the calibration scenario, for GETTHEM (solid lines) and CONSEN (dashed lines). Reproduced from [35].

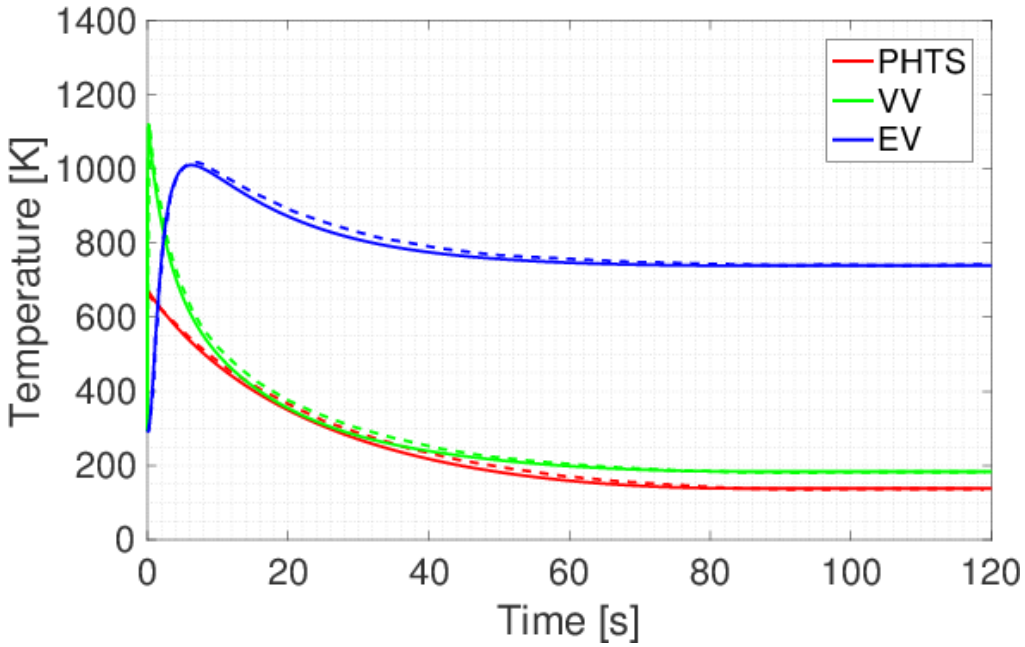

Figure 3.10: Evolution of the temperature in the three volumes of the helium VVPSS model in the calibration scenario, for GETTHEM (solid lines) and CONSEN (dashed lines). Reproduced from [35].

The chosen value of the parameter $F_k x_T$, which minimized the differences between CONSEN and GETTHEM prediction on the pressure behaviour in the VV, is 0.777. The effect of the calibration parameter is reported in Figure 3.11, where the relative error on the peak VV pressure is reported as a function of the parameter. The error is computed as $\epsilon = \frac{\left|p_{VV,peak}^{GETTHEM} - p_{VV,peak}^{CONSEN}\right|}{p_{VV,peak}^{CONSEN}}$; the peak VV pressure is used as variable to check the error, as it is the most important quantity for such analyses.

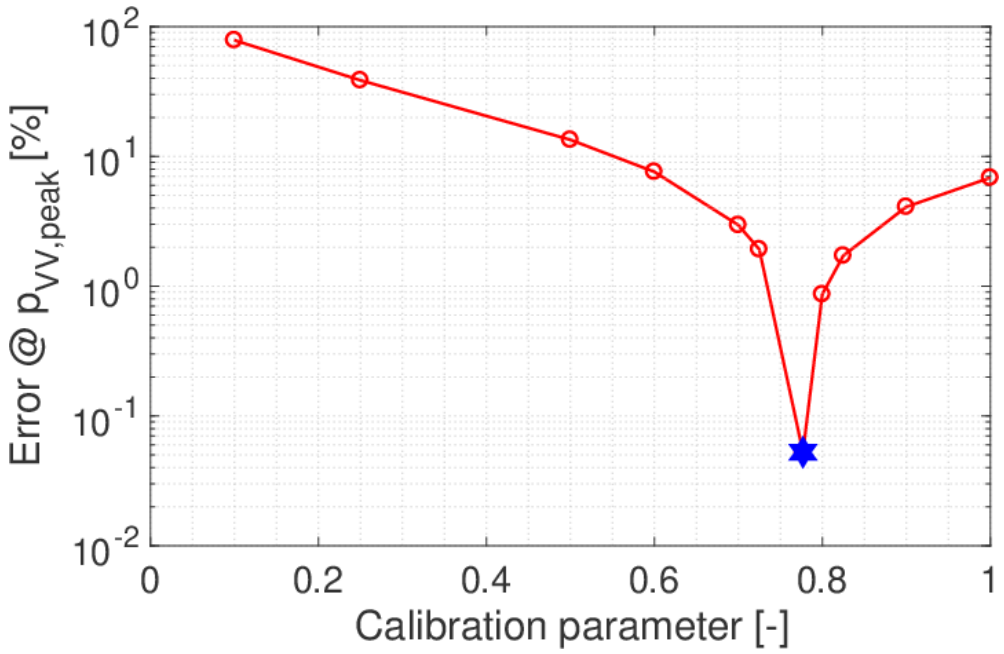

Figure 3.11: Effect of the calibration parameter on the peak VV pressure.

3.3.2. Benchmark results

For the benchmark scenario, the BD and BV parameters are frozen in GETTHEM from the calibration scenario (*i.e.*, the value of $F_k x_T$ is kept unchanged). As mentioned, the only differences in the parameters with respect to the previous scenario are the number of BLs and RLs and their cross sections, which are set equal to the values computed in [39] with the aim of limiting the pressure peak in the VV to its maximum allowable pressure of 200 kPa; Table 3.4 shows the input parameters used in the benchmark scenario. It is important to point out that this exercise has the only objective of verifying the tool, as the chosen cross sections for BLs and RLs are too large to be actually feasible.

As already done for the previous scenario, the comparison between GETTHEM and CONSEN codes for the benchmark scenario are reported in terms of pressure (Figure 3.12) and temperature (Figure 3.13) in the PHTS, VV and EV volumes. As expected, the maximum pressure value reached in the VV is 200 kPa at 1.2 s. The pressure undershoot in the VV after the peak is overestimated by the GETTHEM code in the period between ~5 s and ~15 s, reaching a local minimum value of pressure equal to 125 kPa at 11.8 s; this is again due to the underestimation of the VV pressure decay characteristic timescale already highlighted in the calibration scenario, caused by the different models adopted for BDs and BLs in the two codes,

which, in turn, cause the VV pressure to decay much faster in the GETTHEM analysis than in the CONSEN one. The steady state pressure value in the VV, and in the other components which are in equilibrium, is ~150 kPa, well in agreement with the CONSEN results. This value does not differ from the calibration scenario, as it was expected: in fact, it depends only on the total mass inside the system and on the total volume, and these two parameters were maintained constant.

Figure 3.12 also highlights the effect of the calibration parameter: it is here clearly evident how, also for the benchmark scenario, even a small deviation from the optimum value identified above causes a large error on the peak VV pressure.

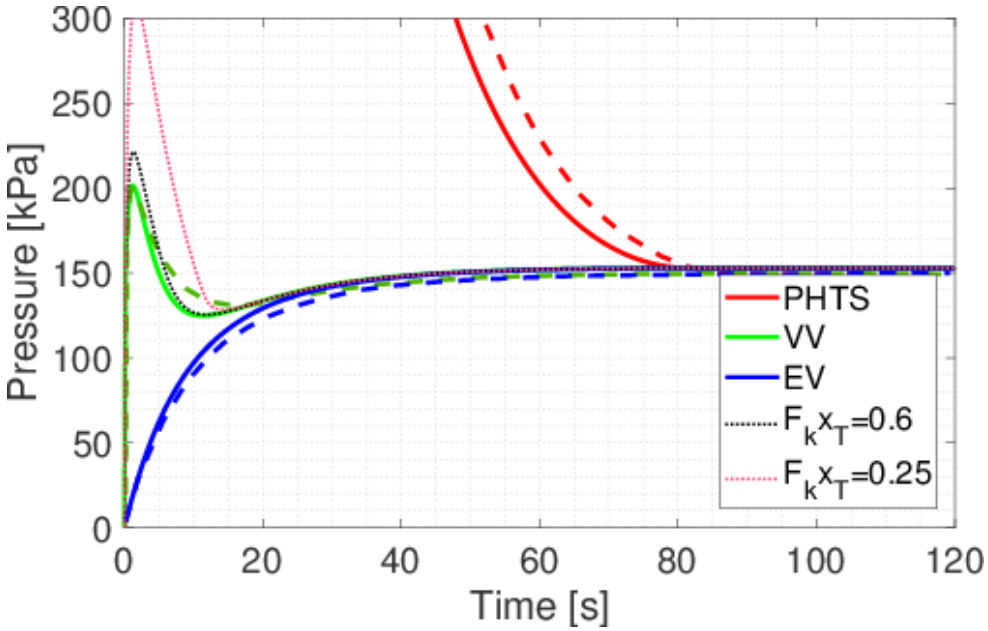

Figure 3.12: Evolution of the pressure in the three considered volumes in the helium benchmark scenario, for GETTHEM (solid lines) and CONSEN (dashed lines). The black and pink dotted lines represent the VV pressure evolution with sub-optimal values of the calibration parameter (adapted from [35]).

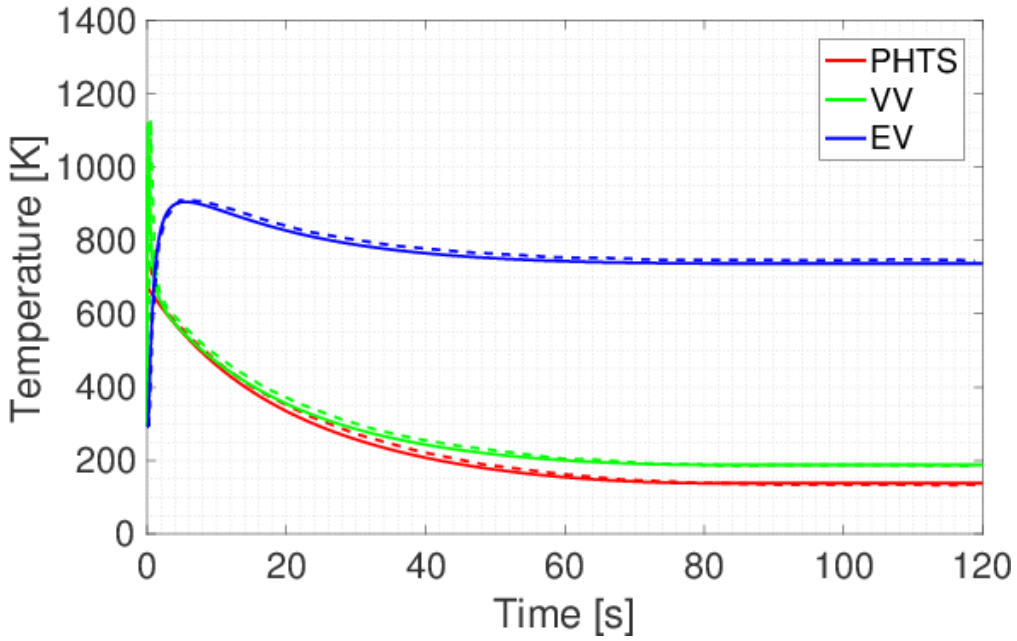

Figure 3.13: Evolution of the temperature in the three considered volumes in the helium benchmark scenario, for GETTHEM (solid lines) and CONSEN (dashed lines). Reproduced from [35].

The comparison of the results shows a good agreement of the pressure and temperature peak values, both within the 1 % of discrepancy if compared to CONSEN results. The timing of the pressure and temperature peaks in the VV are also well reproduced. The overall duration of the transient is slightly underestimated also in the benchmark scenario, with an error comparable with the calibration scenario (~2 %). This underestimation is again due to the different models adopted for the BD and BL, leading in GETTHEM to an overestimation of the mass flow rate removed from the VV with respect to CONSEN in the initial phases of the transient, as also highlighted by Figure 3.14, where the evolution of the mass flow rates is compared for the two codes. This underestimation of the characteristic timescale, however, does not affect significantly the temperature evolution, as already found in the calibration scenario: in fact, the prediction of the temperature evolution given by GETTHEM are in excellent agreement with the CONSEN one.

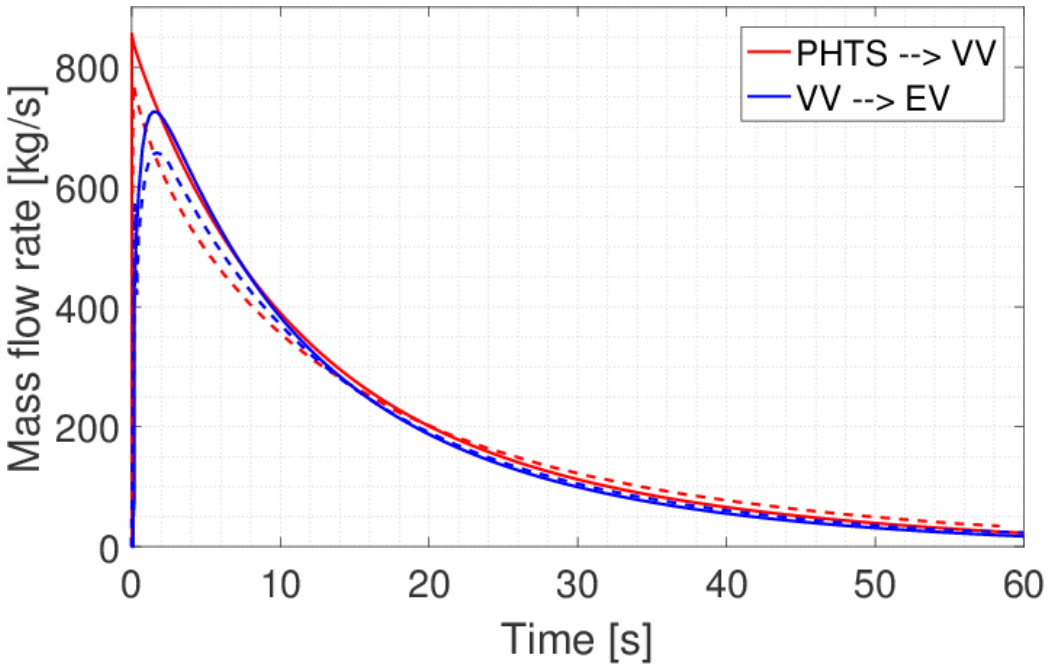

Figure 3.14: Evolution of the mass flow rate from PHTS to VV and from VV to EV, for the helium benchmark scenario, for GETTHEM and CONSEN models (solid lines: GETTHEM; dashed lines: CONSEN).

3.4. Validation in accidental conditions: water model[16]

For the check of the VVPSS GETTHEM model in the water-cooled BB case, a validation is performed, against experimental data from the experimental campaigns led in Japan between March 2000 and November 2001 at the Inlet Coolant Events test facility (ICE facility) [46]. The ICE facility was built in order to perform experimental validation of codes against ICE accidents in water-cooled tokamaks, with ITER as target.

3.4.1. Description of the ICE facility

The circuit of the ICE facility is shown in Figure 3.15. The PHTS is simulated by an electric boiler, which is a cylindrical tank with a volume of 0.63 m^3; the coolant inside the boiler can be pressurized by N_2. The boiler is connected by three nozzles to a metallic tank (0.5 m^3) representing the Plasma Chamber (PC); the lines connecting the boiler to the nozzles can be inactivated using valves, in order to change

[16] Part of the work described in this section was also published in [35].

the discharge cross section. The nozzles have a hydraulic diameter of 10 mm; the PC can be heated externally by electric heaters [46].

The PC is connected to another tank, representing the VV (0.1 m³), through a metallic plate called “Divertor”, with 12 rectangular holes (5×80 mm²). Finally, the PC is connected by three relief lines (diameter 49.5 mm) to the Suppression Tank (ST), with a volume of 0.93 m³ and a maximum water storage of 0.5 m³ [46].

The validation is performed against the case 4 of the 2000 experimental test campaign, whose parameters are described in Table 3.5. The results on several other cases tested were available; however, PC, Divertor and VV were heated externally but no data on the heating processes were available, limiting the number of cases available to validate the code.

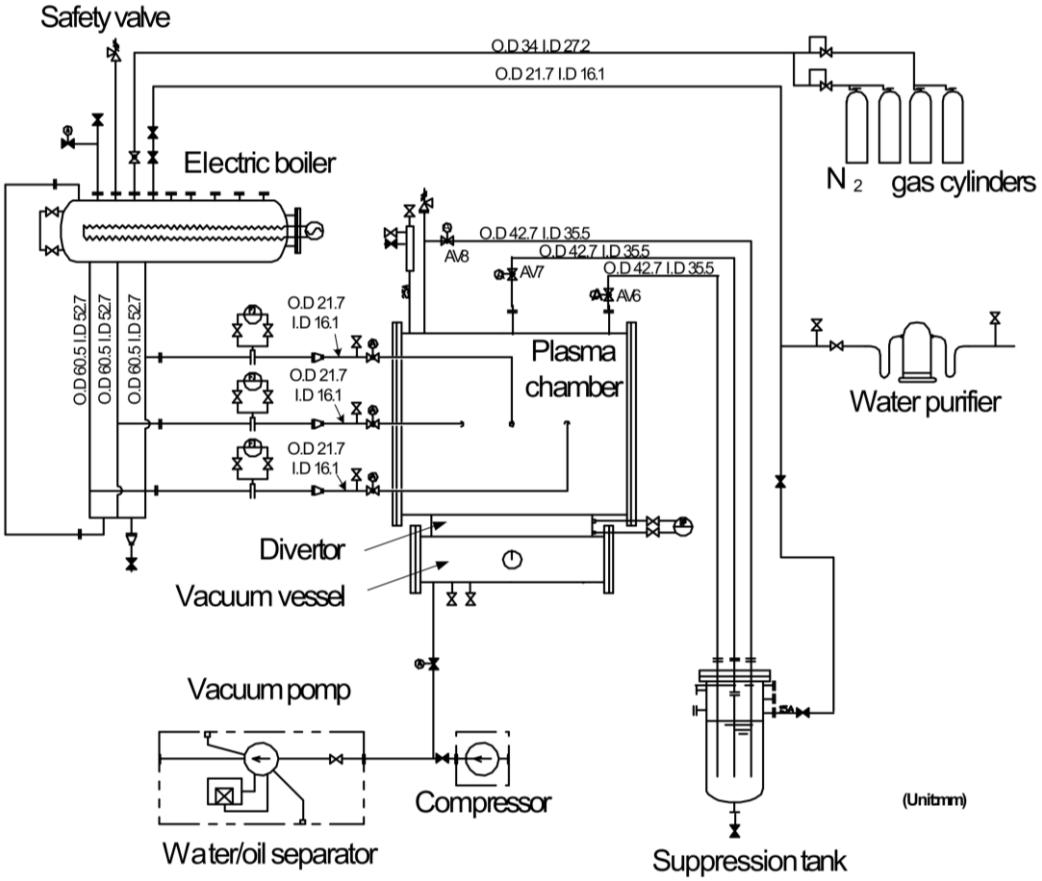

Figure 3.15: ICE test facility (reproduced from [47]).

3.4.2. GETTHEM ICE facility model

The GETTHEM model of the ICE facility, used for the validation, is reported in Figure 3.16. Although the model is different from the model reported in section 2.3.2 above (see Figure 2.14b), the same components are used and only the parameters were changed. The only exception is the boiler: in fact, even with N_2 injection active, the pressure within the boiler was not constant during the experiment; so, the boiler is modelled as an ideal pressure source in which the pressure and enthalpy evolution are set as BCs in order to match the ICE experimental data during the entire transient.

Moreover, the PC and VV volumes of the ICE facility as are lumped in a single 0D volume called VV in the model. This simplification is justified by ICE results, which, for all the experiments, showed always the same pressure in PC and VV [46, 48]. Finally, two localized pressure drops are used to represent the pressure loss within the injection and relief lines, as well as the localized pressure drops at the nozzles: the first pressure drop is located after a set of valves, which simulate the nozzles injecting the coolant from the boiler, while the second one is between the burst disks and the SP.

Table 3.5: ICE 2000 test case 4 initial parameters [46].

Variable	***Initial value***
Number	1
Boiler temperature [K]	423
Boiler pressure [MPa]	2
PC wall temperature [K]	503
Suppression Tank temperature [K]	293
Number of safety lines	3
Injection time [s]	45
Heaters	OFF
Injection diameter [mm]	10
Number of injectors	2

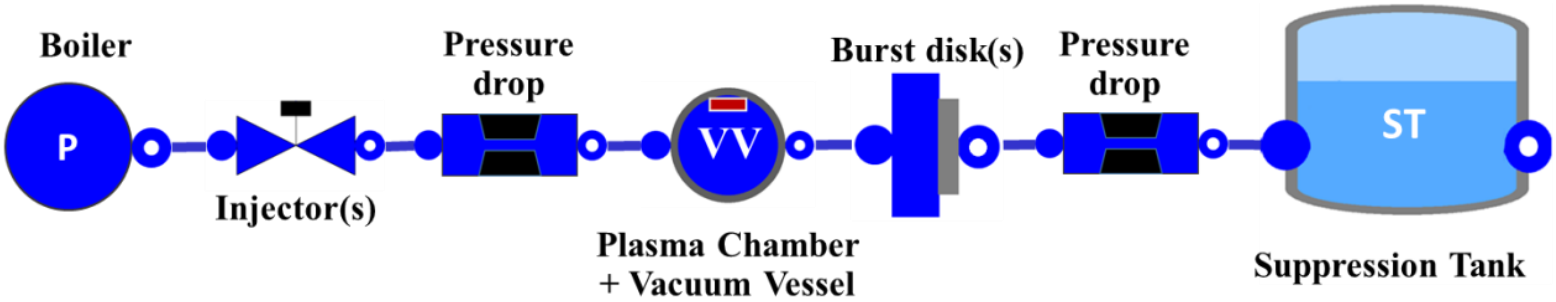

Figure 3.16: GETTHEM model used in the validation with ICE test result (reproduced from [36]).

3.4.3. Validation results

In the following the comparison between the ICE facility experimental results (solid lines) and GETTHEM computed results (dashed lines) is reported, in terms of mass flow rates injected from the boiler to the VV (Figure 3.17) and pressure inside the VV and ST (Figure 3.18).

At $t = 0$ the boiler starts discharging the water inside the VV, at a mass flow rate which stays almost constant (around 6 kg/s) during the 45 s of injection; this is due to the choked flow occurring at the injectors, which limits the fluid velocity (and, consequently, the mass flow rate) to the choked value, that depends on the upstream pressure only (as per equations (24) and (25) above). In fact, the small variations in the mass flow rate follow the variation in the boiler pressure, as evident in Figure 3.19. The BDs open immediately after the beginning of the transient, but the pressure in the VV continues increasing for ~10 s, when the peak is reached. The VV pressure stays then almost constant during the injection of water and rapidly drops when the injectors are closed, as water continues to be discharged to the ST.

The two graphs show an excellent agreement of the computed results if compared to the experimental data. In particular, the mass flow rate prediction reproduces almost perfectly the evolution in the ICE facility with an error always smaller than 5 %. Furthermore, the pressure peak value in the PC is overestimated by about 20 kPa (less than 5 %) and the final pressure in the VV at the end of the transient is underestimated by ~7 kPa. Finally, the pressure evolution in the ST is very well reproduced by the GETTHEM model with a pressure value reached at the end of the transient ~6 kPa higher than the experimental one. It is anyway important to note that, while GETTHEM correctly reached the same value of pressure at the end of the transient for VV and ST, the experimental data differ by ~13 kPa; since the two volumes are connected, a pressure unbalance may occur because of evaporation inside the VV, due to the higher wall temperature, which is not modelled in GETTHEM; alternatively, this difference can be due to experimental accuracy, maybe because of sensor hysteresis or simply different scales, as the two sensors had to measure very different values of pressure throughout the transient. The GETTHEM result is, however, between the two, so it can be considered correct within the experimental accuracy.

Figure 3.19 shows the evolution of pressure in the three volumes of the system (left axis) and the mass flow rate evolution (right axis). As mentioned, the pressure

inside the boiler is used as BC of the system in order to reproduce the behaviour of the ICE facility test Case 4.

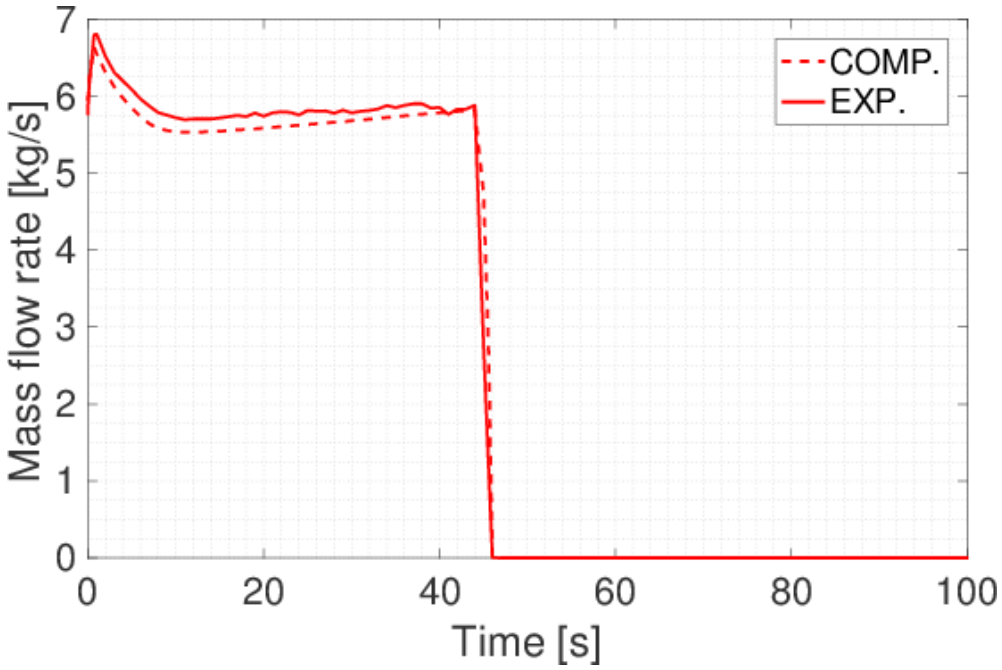

Figure 3.17: Comparison of the mass flow rate injected from the boiler to the VV. Solid line: experimental data; dashed line: GETTHEM results (reproduced from [36]).

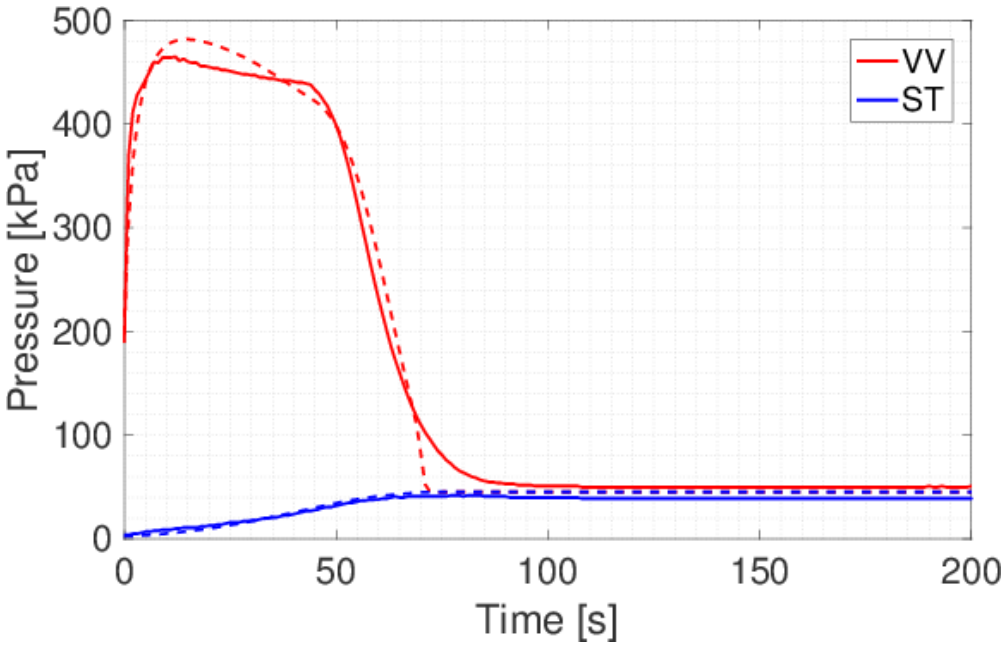

Figure 3.18: Comparison of the pressure evolution inside the VV (red lines) and ST (blue lines). Solid lines: experimental data; dashed lines: GETTHEM results (adapted from [36]).

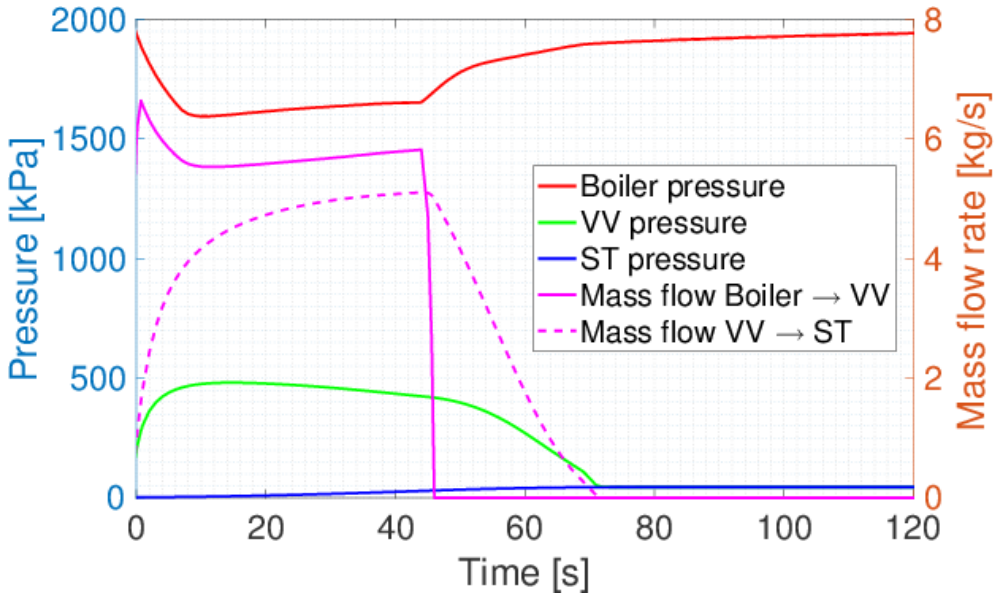

Figure 3.19: Evolution of pressures (left axis) and mass flow rates (right axis) on GETTHEM model of ICE test facility.

Chapter 4

GETTHEM applications to the EU DEMO tokamak

Having verified the GETTHEM capabilities in both nominal and off-normal conditions, it is now applied to EU DEMO-relevant scenarios: in section 4.1 below, the optimization of the mass flow rate distribution for the HCPB BB is performed, whereas in section 4.2 below the analysis of the EUROFER temperature distribution on the FW for both HCPB and WCLL is shown. At the end, a parametric study of an in-VV LOCA is reported in section 4.3 below.

4.1. Optimization of the coolant flow distribution in the HCPB BB[17]

4.1.1. Drivers

For this analysis, the baseline 2014 scenario is used; the power distribution to the BB according to such scenario is reported in Figure 4.1 and Table 4.1, in terms of FW surface load, FW nuclear load and BZ total load[18]. The loads vary with the poloidal location of the BM, but are considered uniform inside each BM (i.e., all the FW channels have the same load and all the CPs have the same load).

[17] Part of the work described in this section was also published in [29].
[18] In the 2014 revision of the HCPB BB, 6 BMs were foreseen for both IB and OB.

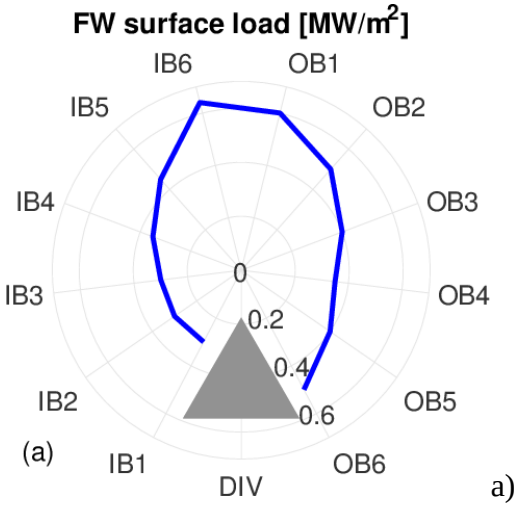

a)

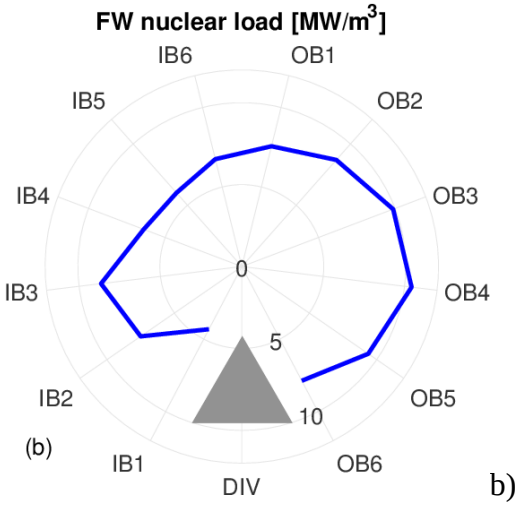

b)

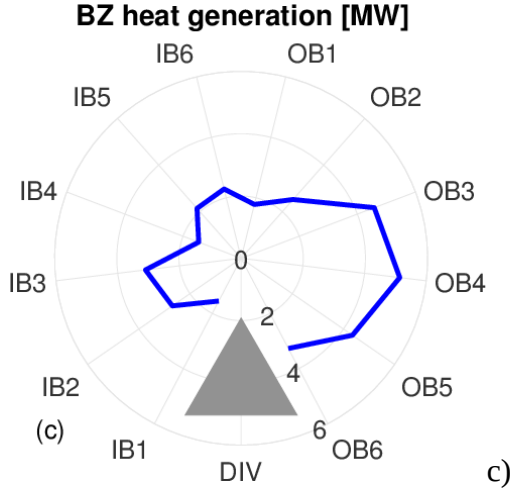

c)

Figure 4.1: Plot of the poloidal distribution of the heat loads on a 2014 HCPB segment (IB+OB): FW surface load (a), FW volumetric nuclear load (b), BZ heat generation (c). The triangle (DIV) represents the divertor (reproduced from [30]).

4.1.2. Boundary conditions

As mentioned in section 2.3.1 above, ex-vessel compressors, HXs, valves and manifolds are not included (i.e., the loops are not closed, see Figure 2.12). Therefore, BCs of fixed inlet mass flow rate (modelled as an ideal flow source, "m" in Figure 4.2) and fixed outlet pressure ("p" in Figure 4.2) are used. The nominal inlet conditions are 300 °C and 80 bar. The values of fixed mass flow at inlet are set as twice the value in [49], see Table 4.1 below, while the outlet pressure is fixed at 79 bar, as the total pressure drop across the BM in nominal conditions in the 2014 revision of the design is assumed to be ~1 bar, as given in [50]; when a higher pressure drop develops, the inlet pressure is free to increase. As shown in Figure 1.5, for the HCPB-I the helium flows initially in the FW channels, and only afterwards in the BZ and caps.

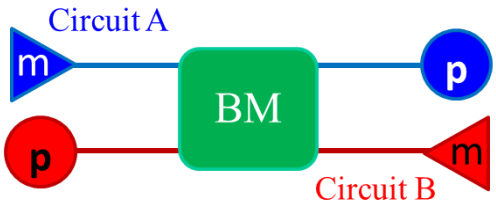

Figure 4.2: BCs in the HCPB simulation setup (reproduced from [30]).

Table 4.1: Poloidal distribution of the heat loads and coolant mass flow rate for a 2014 HCPB segment (adapted from [30]).

Load		***BM1***	***BM2***	***BM3***	***BM4***	***BM5***	***BM6***
FW surface load [MW/m²]	IB	0.300	0.300	0.300	0.350	0.450	0.640
	OB	0.600	0.500	0.400	0.350	0.400	0.500
FW volumetric nuclear load [MW/m³]	IB	4.32	7.50	8.65	6.40	6.01	6.75
	OB	7.56	8.69	9.87	10.4	9.37	7.87
Heat generated in the BZ [MW]	IB	1.55	2.69	3.10	1.46	2.14	2.29
	OB	1.78	2.52	4.58	5.14	4.35	3.27
Mass flow rate [kg/s]	IB	5.66	5.24	7.78	5.31	4.99	5.79
	OB	7.87	11.8	14.0	16.8	13.7	10.6

4.1.3. Results: HCBP-I

With the given simulation setup, all the FW channels are subject to the same load and have the same properties (as no orifices are implemented at this stage). Therefore, all channels exhibit exactly the same behaviour, so that the distribution of

pressure drops inside each FW channel and the temperature distribution is reported here for just one of them, as it is representative of the whole FW object. Analogous consideration applies to the BZ object, where all the CPs show the same behaviour (as well as the two caps); the different length of the channels inside a CP has a negligible bearing on the results (always below 1 %). Actually, also some edge effects are present, due to the fact that the first and last channels are coupled with only one channel; these effects are correctly accounted for by the model, but, since the resulting deviation of the results was always found to be lower than 5 ‰, the reported results refer to channels in the "bulk" without losing generality. Finally, the A and B loops show a perfectly antisymmetric behaviour, so all the results are shown for just one of them.

As a consequence of the forced mass flow rate distribution explained above, the pressure drops can be different among the BMs, even though they are supposed to be cooled in parallel; this implies that, if this is the wanted mass flow rate distribution, orifices shall be added in the circuit in series with the BMs showing a lower pressure drop.

The resulting pressure drops across each of the modules of the IB and OB segments are reported in the following Table 4.2. As expected the contribution of the FW is always much higher than that of the BZ, both due to the bigger length and to the higher friction that develops inside the front part, where the channel is ribbed. This is clearly visible also from the histogram of Figure 4.3, where the distribution of the FW pressure drop among the three parts of the FW channel is shown: the pressure drops inside the side parts are comparable to those found in the BZ, while the one in the front part is always at least four times bigger. The differences found among the BMs, instead, are given by the different value of mass flow rate forced through the channels and by the different heat loads: all of them, in fact, have the same geometry and nominal pressure drop. The two BMs showing the highest pressure drop, in fact, are the BM3, which is the one with the highest mass flow rate and BZ heat load, and the BM6, subject to the highest FW heat load. IB1 and IB2, instead, have the largest number of channels and CPs, and consequently show the lowest pressure drops. Among the OB BMs, instead, the pressure drop distribution is mainly driven by the total mass flow rate: in fact, the BMs with the largest pressure drop are the OB3-5, which are also the ones with the largest flow rate, see Table 4.1.

Finally, the pressure drop in all the OB BMs is ~3× larger than that in the respective IB BM; this effect, however, is only due to the larger mass flow rate that is forced through the OB BMs.

Table 4.2: HCPB-I: Computed pressure drop across the BMs (reproduced from [30]).

Inboard			Outboard		
	Region	Pressure drop [bar]		Region	Pressure drop [bar]
	FW	0.477		FW	1.00
IB1	BZ	0.0517	OB1	BZ	0.0853
	Total	0.529		Total	1.09
	FW	0.421		FW	1.74
IB2	BZ	0.0488	OB2	BZ	0.145
	Total	0.470		Total	1.88
	FW	0.856		FW	2.33
IB3	BZ	0.0694	OB3	BZ	0.118
	Total	0.925		Total	2.45
	FW	0.617		FW	2.90
IB4	BZ	0.0544	OB4	BZ	0.220
	Total	0.672		Total	3.12
	FW	0.624		FW	2.03
IB5	BZ	0.0558	OB5	BZ	0.155
	Total	0.680		Total	2.18
	FW	0.823		FW	1.31
IB6	BZ	0.0732	OB6	BZ	0.0675
	Total	0.896		Total	1.38

Figure 4.4 shows the temperature distribution along the helium path for all the BMs; the peak temperature is reached in the BZ region, overcoming also the design outlet value of 500 °C (which is needed in order to keep the EUROFER at temperatures below the 550 °C limit mentioned in section 2.2.2 above), while the FW and caps temperature is kept considerably lower. The large difference in the behaviour of CPs and caps inside the same BM can be explained by looking at Figure 4.5, which shows the split of the flow rate among them. Each of the two caps has the same heat load as a single CP; they, however, have a smaller number of channels with a larger cross section, so the friction factor is smaller and the caps account for 20% to 30% of the total flow rate, even if they contain only 2% to 5% of the chan-

nels. Therefore, the cooling of the CPs is less effective, leading to higher temperatures with respect to those found in the caps. The maximum helium temperature (and, consequently, the maximum solid temperature) can then be limited by mitigating this unbalance, for instance adding orifices at the caps inlet to increase the pressure drop.

The different behaviour among the BMs, instead, is again due to both the different flow rate and the different heat loads.

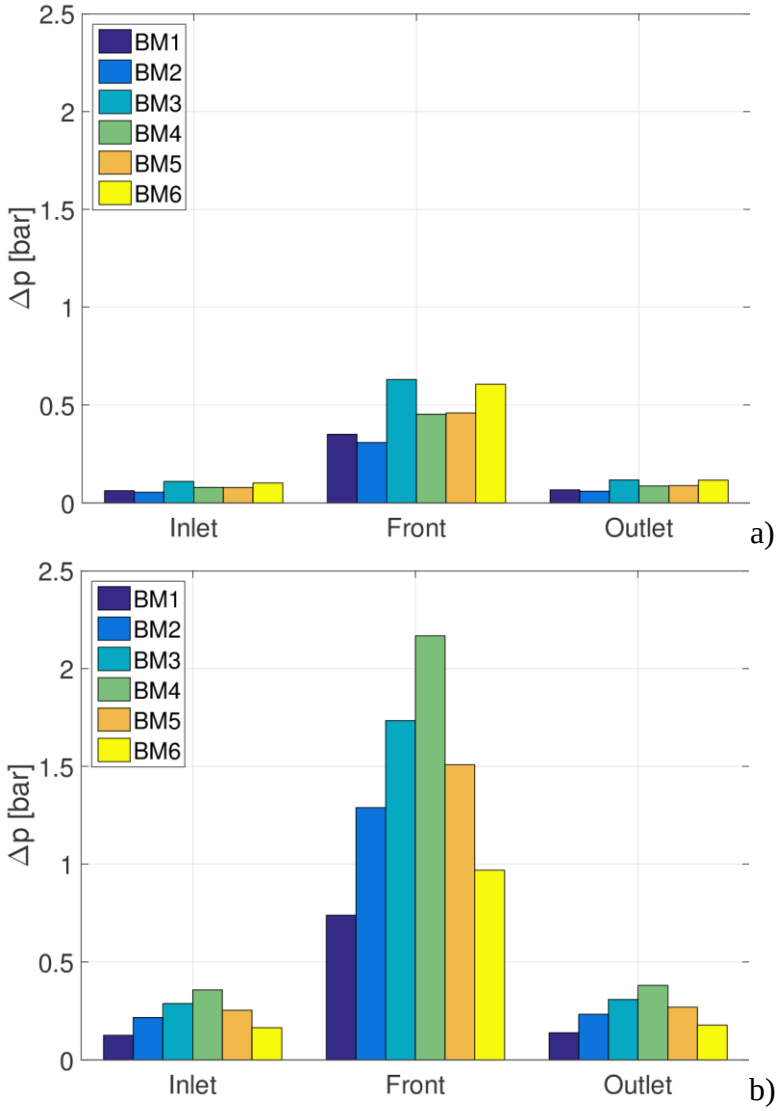

Figure 4.3: HCPB-I: Computed share of the pressure drop among the three parts of the FW channels: IB BMs (a) and OB BMs (b) (reproduced from [30]).

In addition, it should be stressed that such result is not even compliant with the BoP design: as mentioned, in fact, it has been obtained doubling the mass flow rate value with respect to that reported in [49], which was determined in order to have the prescribed temperature difference across the BM; the average coolant outlet temperature is indeed much lower than the design value of 500 °C. This assumption was driven by the very high temperatures reached with the nominal mass flow rate distribution, which would have overcome the melting temperature of the EUROFER.

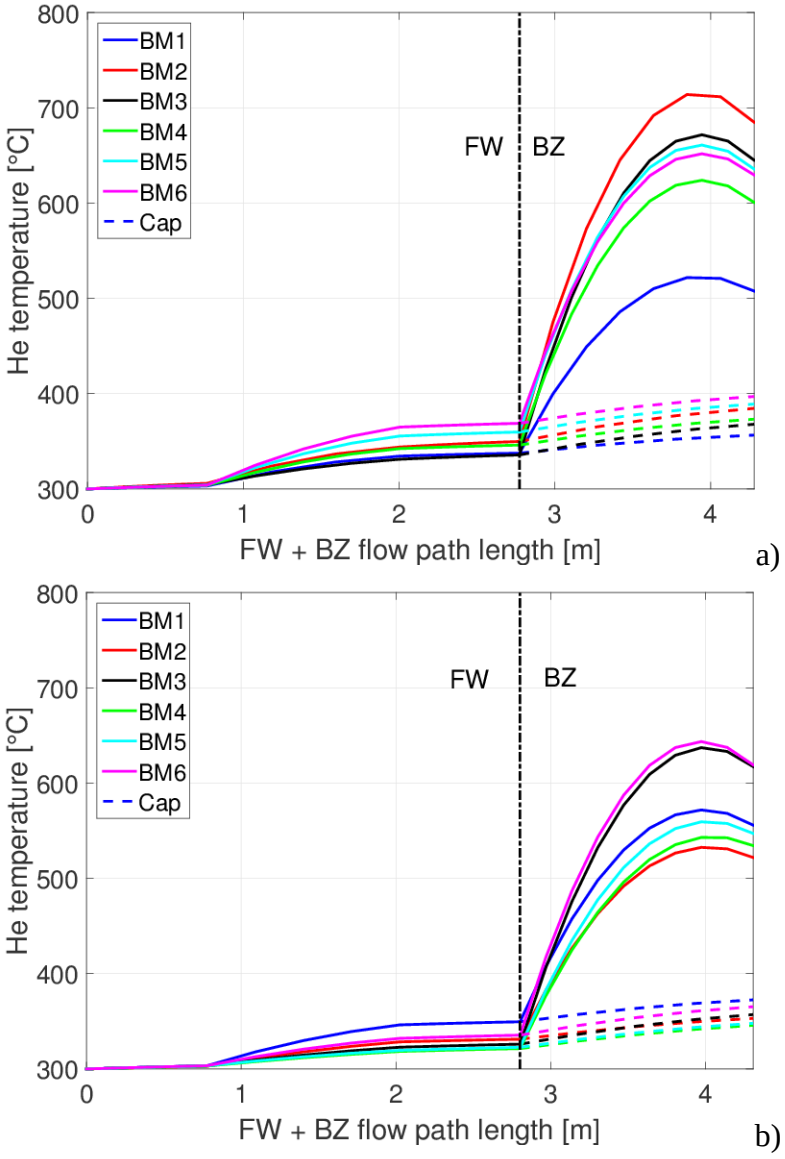

Figure 4.4: HCPB-I: Computed temperature distribution in the 12 BMs: IB BMs (a) and OB BMs (b). The dashed lines in the BZ region refer to the caps (reproduced from [30]).

The implementation of orifices at the inlet of the caps shows indeed the expected improvements: in fact the CPs are cooled better and, even halving the mass flow rate in each BM, the temperature is lower than in the previous case, as shown in Figure 4.6. This is due to the better distribution of the flow rate, as shown in Figure 4.7: now the caps correctly account for ~2% to ~6% of the total flow rate. More important, the peak temperature is now below 500 °C, with the exception of some IB BMs (where the peak temperature is indeed lower than before).

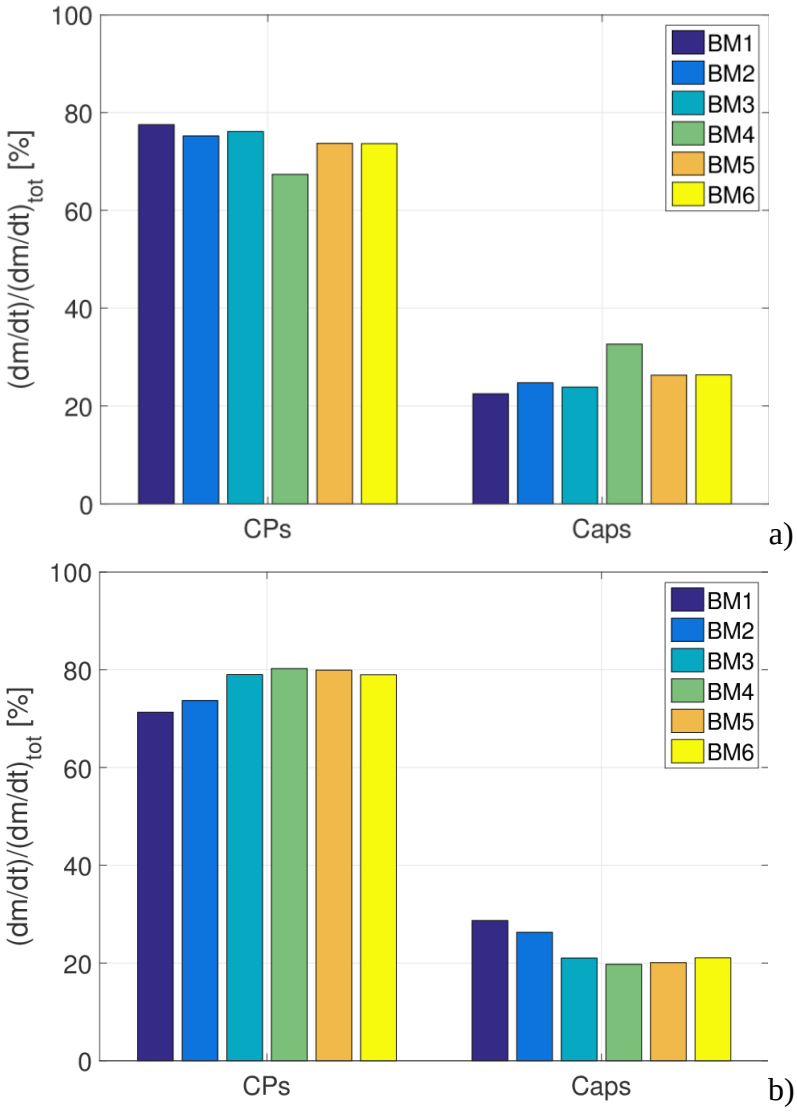

Figure 4.5: HCPB-I: Computed share of the mass flow rate among CPs and caps: IB BMs (a) and OB BMs (b) (reproduced from [30]).

Moreover, such results are obtained setting back the mass flow rate to the design values reported in [49], with a double beneficial effect: in fact, the outlet temperature is now everywhere closer to the design value of 500 °C, which is compliant with the BoP design, while the total pressure drop is reduced as well by a factor of ~2×, even if an orifice is present, as an effect of the reduced coolant speed; hence, considering that the compression power is proportional to the mass flow rate and pressure drop, the total compressor work is reduced by more than a factor of 4.

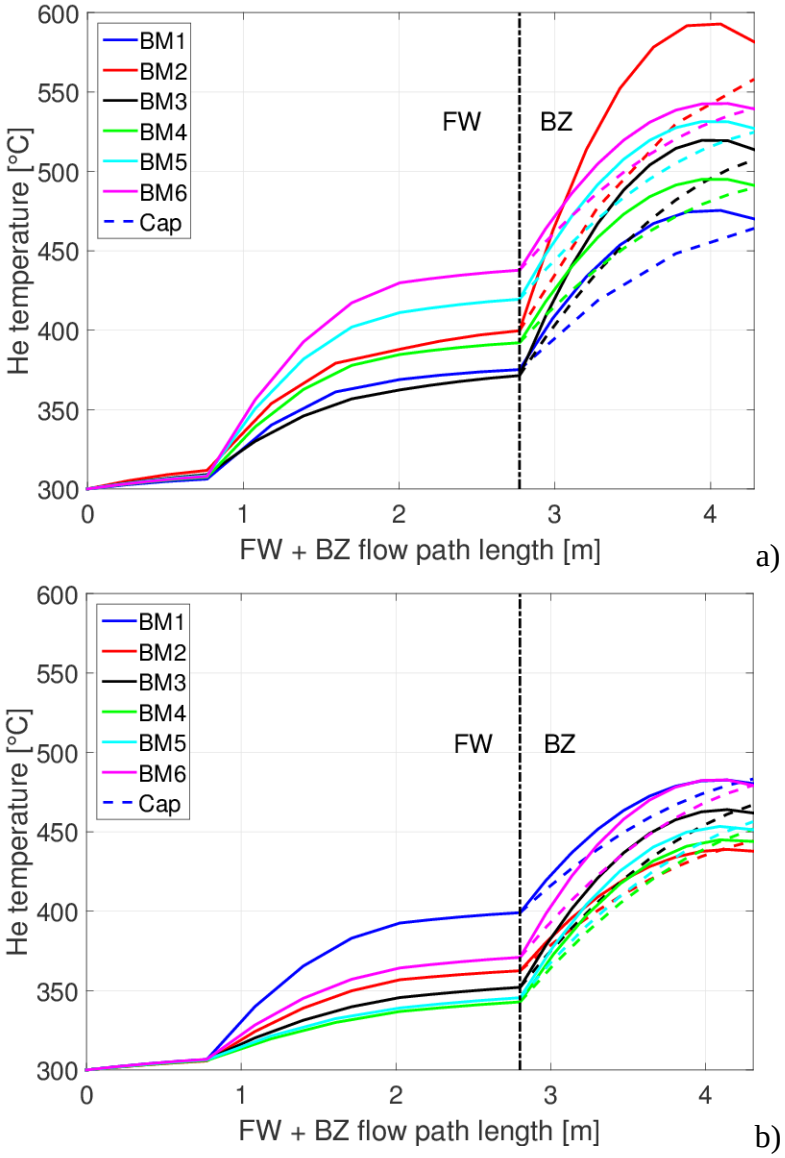

Figure 4.6: HCPB-I: Computed temperature distribution in the 12 BMs, when orifices are introduced at the cap inlets: IB BMs (a) and OB BMs (b). The dashed lines in the BZ region refer to the caps (reproduced from [30]).

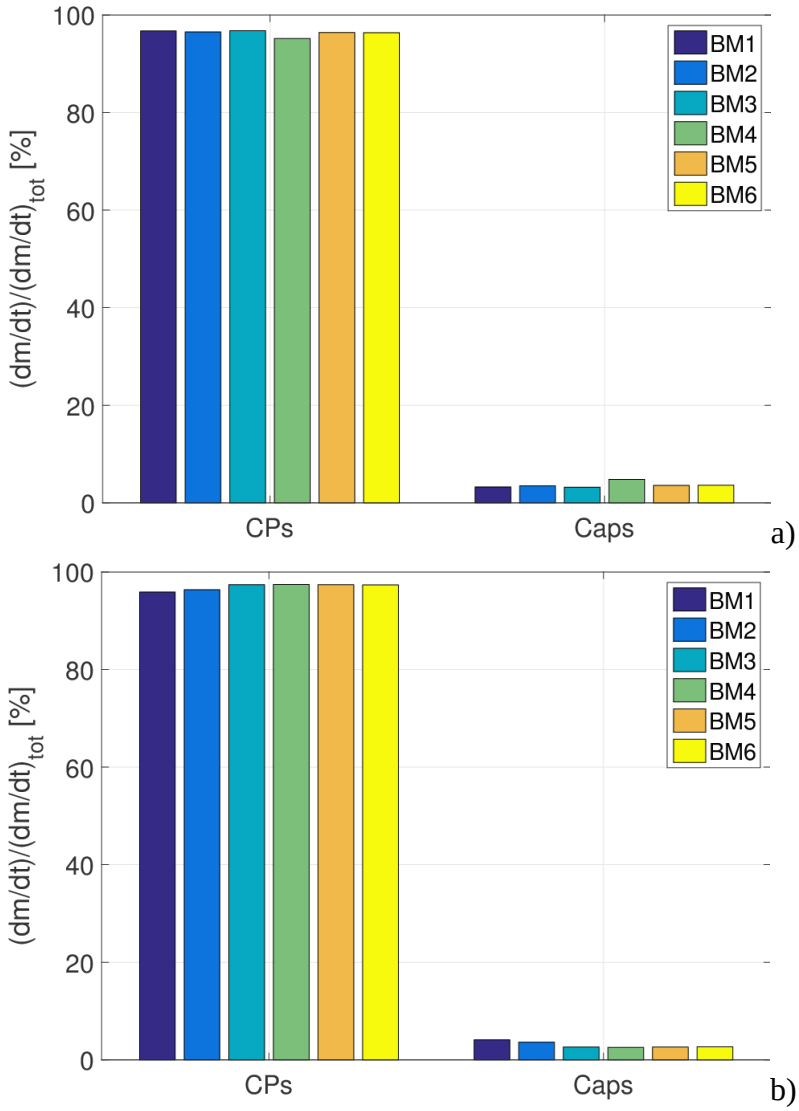

Figure 4.7: HCPB-I: Computed share of the mass flow rate between CPs and caps, when orifices are introduced at the cap inlets: IB BMs (a) and OB BMs (b) (reproduced from [30]).

4.1.4. Results: HCPB-S

In the HCPB-S configuration, considering what was found for the HCPB-I, the simulations are performed with the orifices at the inlet of the caps, and imposing half of the mass flow rate given in Table 4.1 above, through both the BZ and the FW. As stated for the HCPB-I, all the channels in the FW, CPs and caps are subject to the same load and the same flow rate; hence, the results are shown for just one of them.

Since the inlet conditions are identical, the pressure drop in the FW loop is very close to the HCPB-I case; this is true also for the BZ loop, where slightly bigger differences are found, due to the lower inlet temperature with respect to the previous case. The results for FW and BZ are reported in Table 4.3. Again, the highest pressure drops are found in the modules with the highest mass flow rate and/or the highest loads.

Also the temperature distribution inside the FW (Figure 4.8) is almost unaffected by the different configuration but, being the FW loop now separated from the BZ one, the mass flow rate can be considerably decreased to reduce the pressure drop, as the overall maximum temperature in the loop is the maximum temperature found in the FW.

The lower temperature at the inlet of the BZ brings the temperature in the BZ below 500 °C, also in the IB BMs which did not respect such constraint with the HCPB-I, see Figure 4.9: this suggests that HCPB-S may be used in such BMs, whereas HCPB-I (which has the advantage of incorporating the FW heat in the PHTS) should be used elsewhere.

Table 4.3: HCPB-S: Computed pressure drop across the BMs (reproduced from [30]).

Inboard			Outboard		
	Region	Pressure drop [bar]		Region	Pressure drop [bar]
IB1	FW	0.145	OB1	FW	0.309
	BZ	0.131		BZ	0.305
IB2	FW	0.131	OB2	FW	0.520
	BZ	0.127		BZ	0.545
IB3	FW	0.258	OB3	FW	0.691
	BZ	0.197		BZ	0.448
IB4	FW	0.190	OB4	FW	0.857
	BZ	0.194		BZ	0.626
IB5	FW	0.196	OB5	FW	0.599
	BZ	0.194		BZ	0.439
IB6	FW	0.261	OB6	FW	0.394
	BZ	0.253		BZ	0.247

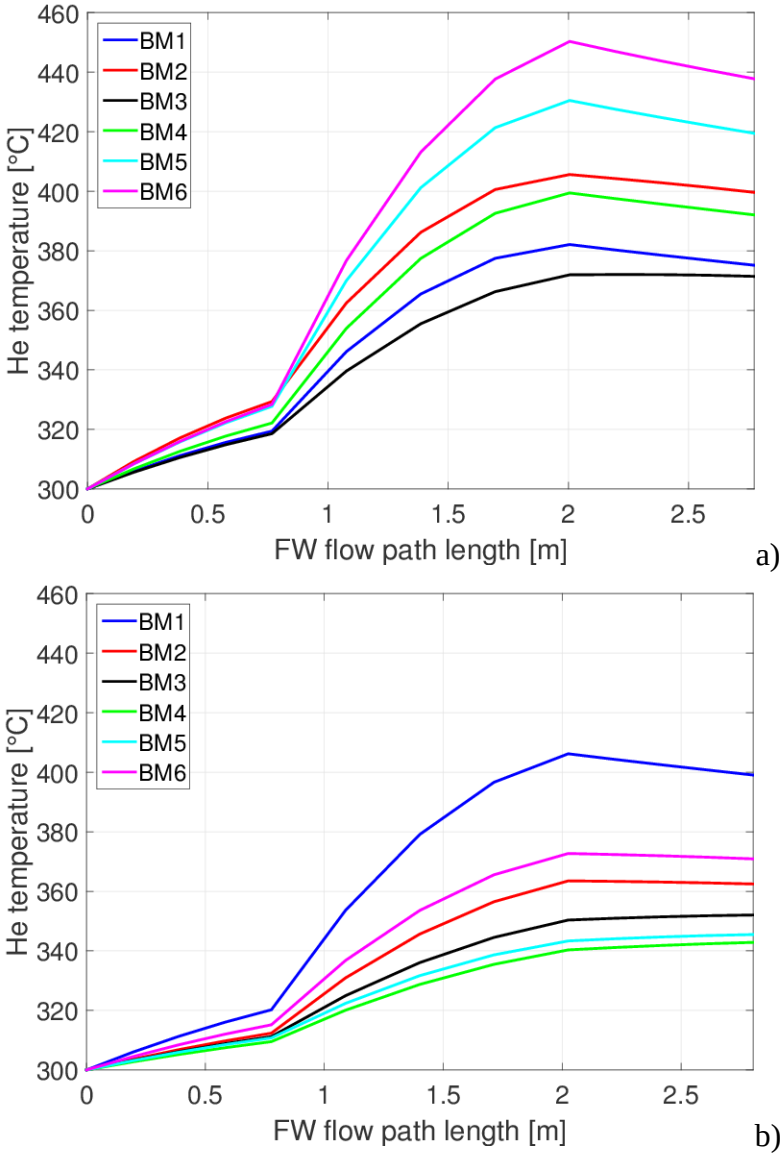

Figure 4.8: HCPB-S: Computed temperature distribution in the FW channels of the 12 BMs: IB BMs (a) and OB BMs (b) (reproduced from [30]).

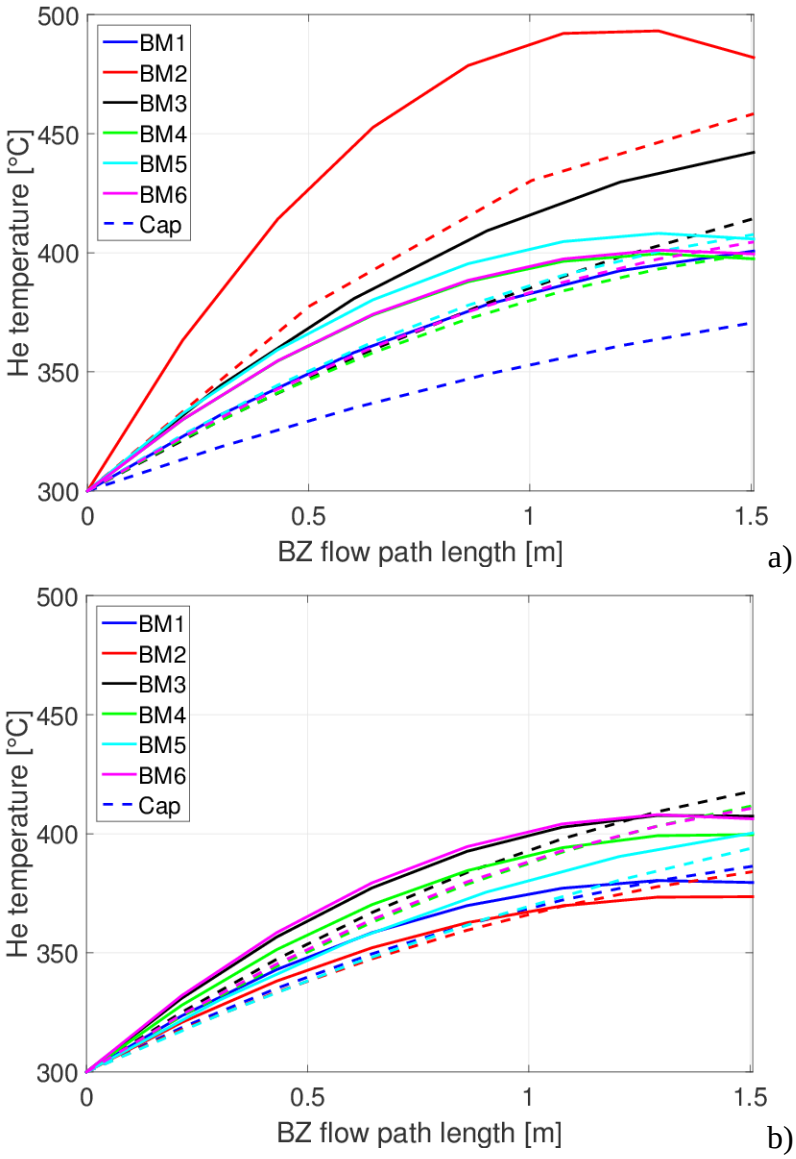

Figure 4.9: HCPB-S: Computed temperature distribution in the BZs of the 12 BMs: IB BMs (a) and OB BMs (b). The dashed lines refer to the caps (reproduced from [30]).

4.2. Analysis of the First Wall hot-spot temperature

4.2.1. Helium-Cooled Pebble Bed[19]

In this study, the postprocessing procedure described in Appendix A for the computation of the hot-spot EUROFER temperature is applied, in order to analyse the

[19] Part of the work described in this section was also published in [11].

peak temperatures reached in a HCPB BB segment (updated to the 2015 design, which foresees 7 BMs on both IB and OB [7]). As reference case, the HCPB-I cooling concept is considered.

The heat loads used in this analysis are the same as described in the benchmark, see section 3.1 above, i.e. a volumetric power generation induced by the neutron flux in the BZ and a surface heat flux from the plasma on the FW. Since this second term is subject to large uncertainties, in the design of the BB an assumption of poloidally uniform heat flux, equal to 500 kW/m², is done [7, 12][20]. Starting from these values, the required coolant mass flow rate for each BM is determined through an energy balance, in order to achieve the target outlet temperature, leading to the values listed in Table 4.4 [12].

Table 4.4: Poloidal distribution of design loads and coolant mass flow in a 2015 HCPB segment (reproduced from [13]).

Module	*BZ load [MW]*	*FW load [MW]*	*Mass flow rate [kg/s]*
OB1	2.52	1.00	3.4
OB2	3.87	1.28	5.0
OB3	4.83	1.40	6.0
OB4	5.06	1.52	6.3
OB5	4.44	1.45	5.7
OB6	3.79	1.31	4.9
OB7	2.84	1.13	3.8
IB1	2.02	1.04	2.9
IB2	2.10	0.967	2.9
IB3	2.60	0.962	3.4
IB4	2.53	0.962	3.4
IB5	2.27	0.802	3.0
IB6	2.89	0.833	3.6
IB7	2.04	1.01	2.9

Since these heat loads are constant during the plasma burn (which lasts ~2 h [51]), only steady-state results will be presented, as the characteristic timescales of

[20] Note that this is a conservative assumption, as the total power resulting would be larger than the power in the plasma. This design heat flux has indeed been recently updated to 290 kW/m², and a detailed poloidal distribution is also being determined [49].

the phenomena involved (advection in the coolant and thermal transient in the EUROFER) are much shorter than the plasma burn itself [13, 30, 52].

GETTHEM is used to analyse the hot-spot EUROFER temperature distribution in a HCPB segment (both IB and OB). The value of the shape factor, to be used to postprocess the solid temperature, is obtained from the same CFD study as that used for the benchmark (section 3.1 above); actually, the value of the shape factor may differ from BM to BM; nevertheless, as the only module for which a CFD analysis was available is the OB4, it is here assumed that the shape factor computed for OB4 can be applied as-is to all BMs.

The resulting hot-spot EUROFER temperature distribution is shown in Figure 4.10, distinguishing the FW and the BZ region. It is immediately evident how the hot-spot solid temperature overcomes the 550 °C limit, albeit marginally in some of them; more in detail, in all the BMs where the temperature is close to 550 °C (i.e. IB6 and OB2-6) the temperature in the BZ is higher than that in the FW, following the coolant temperature which is of course higher closer to the outlet. On the other hand, the BMs that largely overcome the limit have the hot-spot located on the FW, with the worst case being IB1.

Such result implies that, if a better cooling of the FW is achieved, the EUROFER temperature could be set within its operating window; so, the opportunity to use the HCPB-S concept, described in section 2.2.3 above, is considered, at least for the BMs which show such behaviour. In fact, being the FW separated from the PHTS in the HCPB-S concept, the mass flow rate flowing through it is a free parameter (as the coolant outlet temperature is not a concern). Of course, this has the drawback that the power deposited on the FW of such BMs will not be a power source for the external output of the plant, and its use may be limited to e.g. preheating the feedwater before entering the steam generator.

The GETTHEM HCPB model is then used, applying the HCPB concept to IB1-5, IB7, OB1 and OB7, to parametrically vary the mass flow rate flowing through the FW of such BMs, until the EUROFER temperature therein is reduced below 550 °C. On the other hand, the mass flow rate to the BZ of such BMs is reduced: in fact, it was designed in order to have a coolant outlet temperature of 500 °C when in series with the FW. So, the mass flow rate in this case is recomputed again from an energy balance, but accounting for the BZ power generation only (see Table 4.4). The BMs where the temperature was close to 550 °C (namely, IB6 and OB2-6) are

kept unmodified with the HCPB-I concept. The resulting mass flow rate to the HCPB-S BMs is reported in Table 4.5.

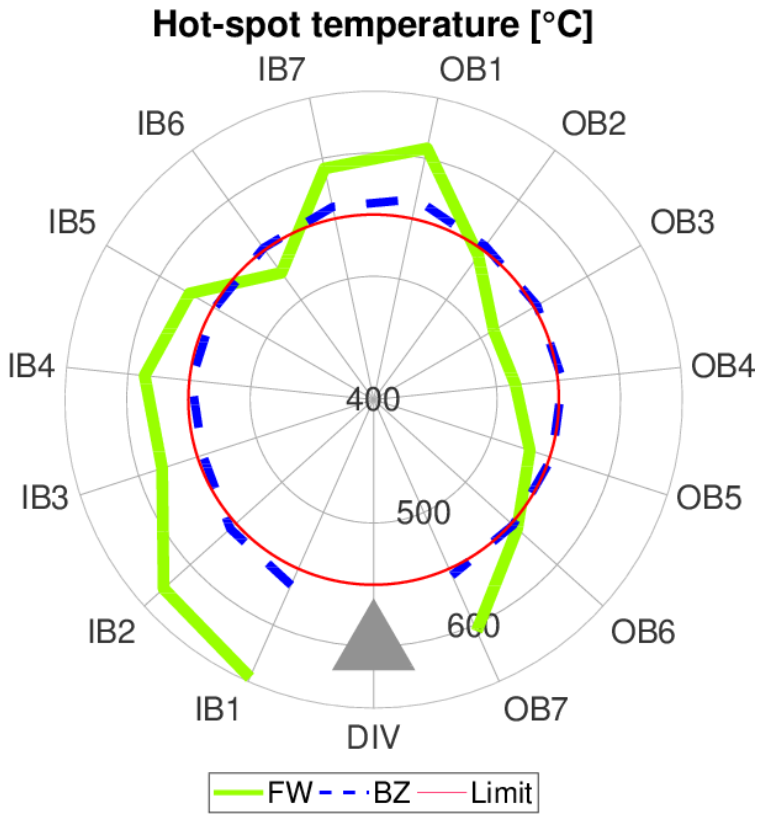

Figure 4.10: Computed hot-spot EUROFER temperature in a HCPB segment, in the FW (green solid line) and BZ (blue dashed line) regions. The thin, pink, solid line represents the operational upper limit of 550 °C (reproduced from [13]).

Table 4.5: Coolant mass flow rate in the 2015 HCPB BMs where the HCPB-S concept is applied (reproduced from [13]).

BM	***BZ mass flow [kg/s]***	***FW mass flow [kg/s]***
OB1	2.4	8.2
OB7	2.7	8.9
IB1	1.9	7.0
IB2	2.0	7.0
IB3	2.5	8.2
IB4	2.5	8.2
IB5	2.2	8.0
IB7	1.9	7.0

The hot-spot temperature distribution with the two concepts is compared in Figure 4.11: of course, the BMs which are still cooled with the HCPB-I concept show the same result, whereas the maximum temperature in the BMs where HCPB-S is applied is drastically reduced, eventually below the limit, proving the advantages of such solution. Nevertheless, the mass flow rate which is forced through these portions of the FW is considerably larger than the design value (up to ~2.5×, compare Table 4.4 and Table 4.5), causing the pressure drop in the separated FW loop to be as high as 3 bar (as a reference, consider that the *total* pressure drop across a 2015 HCPB-I BM is ~2 bar). Assuming perfect toroidal symmetry and replicating this scenario on the 54 OB + 36 IB segments, the overall power requirement for this loop should be ~100 MW[21]. On the other hand, the reduction of the mass flow rate (and pressure drop, consequently) on the BZ loop would induce a reduction of ~50 MW of the pumping power needed, so that overall the total compression power needed by the plant would change from the currently estimated 150 MW [11] to ~200 MW, which is considered acceptable (notwithstanding the reduction of the output power caused by the reduced primary coolant mass flow rate).

One additional point, highlighting again that this issue is caused by an insufficient heat transfer, is that, in the HCPB-I configuration, BMs with similar heat loads and mass flow rate show different behaviours. Taking as reference IB1 and IB7, for instance, from Table 4.4 it appears immediately that the input difference on heat loads and mass flow rate is ~1 %; looking at Figure 4.10, instead, the difference in the hot-spot temperature is much larger (~50 °C, ~17 %). This apparently counter-intuitive behaviour is instead justified by the different geometrical dimensions of the two BMs: in fact, all the BMs share the same cooling system design (i.e. layout, channel dimensions and pitch, poloidal size of pebble beds), obtained in detail looking at the OB4 BM, but, having a different poloidal length, they have consequently a different number of CPs and FW channels. The number of FW channels is then independent on the mass flow rate required by the BM, and as a consequence the mass flow rate *per cooling channel* may vary even significantly. Even though that mass flow rate is correctly dimensioned to achieve the target coolant outlet temperature, a mass flow rate value per channel lower than the design (i.e. 51 g/s per channel in the OB4 [12]) means lower coolant speed, which translates into a lower Reynolds number and, in the end, lower HTC. In the mentioned case of the IB1 and IB7, the total load and mass flow rate differ by less than 0.5 %, but the number of FW

[21] Please consider this number as a very rough estimate, as a HCPB-S FW loop design is not available to compute accurate values.

channels varies from the 112 of the IB1 to the 88 of the IB7, meaning ~26 g/s per channel in the IB1 and ~33 g/s in the IB7 (~25 m/s and ~31 m/s, respectively) [12]. These values translate into a HTC in the FW channels of ~2500 W/(m² K) and ~3000 W/(m² K) in IB1 and IB7 (both considerably lower than the ~4200 W/(m² K) in the IB4) [12], causing the FW temperature to rise much more than in the OB4. In view of this behaviour, it is evident that, in addition to HCPB-S, some other means of heat transfer promotion may be used, such as turbulence promoters (already being investigated [53]) or the "half-monoblock" design (inspired by divertor concepts), proposed by the HCPB design team [54].

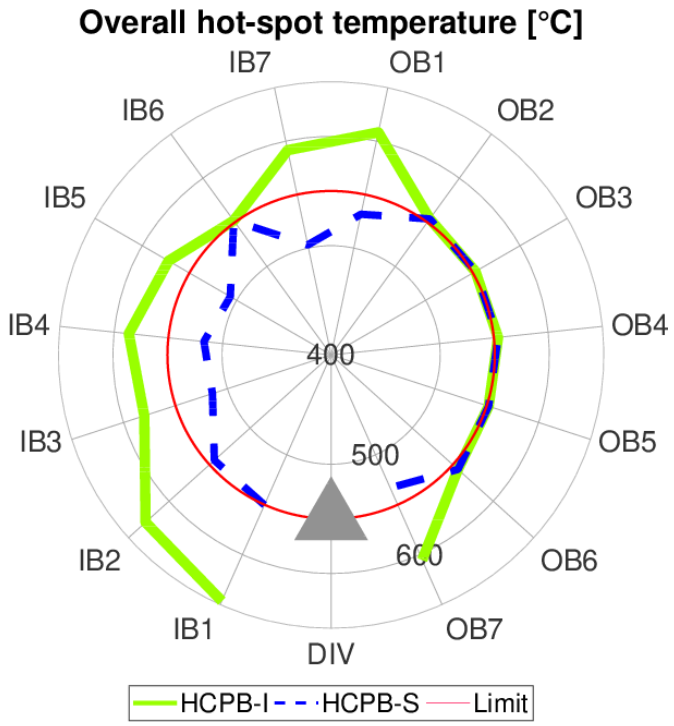

Figure 4.11: Computed overall hot-spot EUROFER temperature in a HCPB segment, with the series (green solid line) and parallel (blue dashed line) cooling options. The thin, pink, solid line represents the operational upper limit of 550 °C (reproduced from [13]).

4.2.2. Water-Cooled Lithium-Lead

An analysis similar to the one described in the previous section is also performed for the WCLL, aimed at identifying the most critical points in the 2016 WCLL FW segments, particularly when loaded with a heat flux distribution different from the design one. Starting from the design coolant mass flow rate distribution, as deter-

mined in [43] based on a uniform FW heat flux of 290 kW/m², a new power distribution, computed by the EUROfusion PMU for the 2017 EU DEMO1 design [55], is applied (keeping the NWL as in the WCLL design [43]).

Since the heat flux distribution computed by the PMU is based on a FW shape different from the 2016 WCLL design, it is rescaled to be adapted to the 2016 WCLL FW. In particular, the FW configuration used by the PMU is based on a MMS approach (as opposed to the SMS approach of the WCLL, see section 1.2.2 above), has a central OB segment different from the other two (all OB segments are equal in 2016 WCLL) and a different poloidal shape (these two conditions come from the 2017 EU DEMO1 revision, which is different from the 2015 one on which the 2016 WCLL is based). A 3D CAD of the PMU FW is shown in Figure 4.12a, and its poloidal shape is compared to the WCLL one in Figure 4.12b.

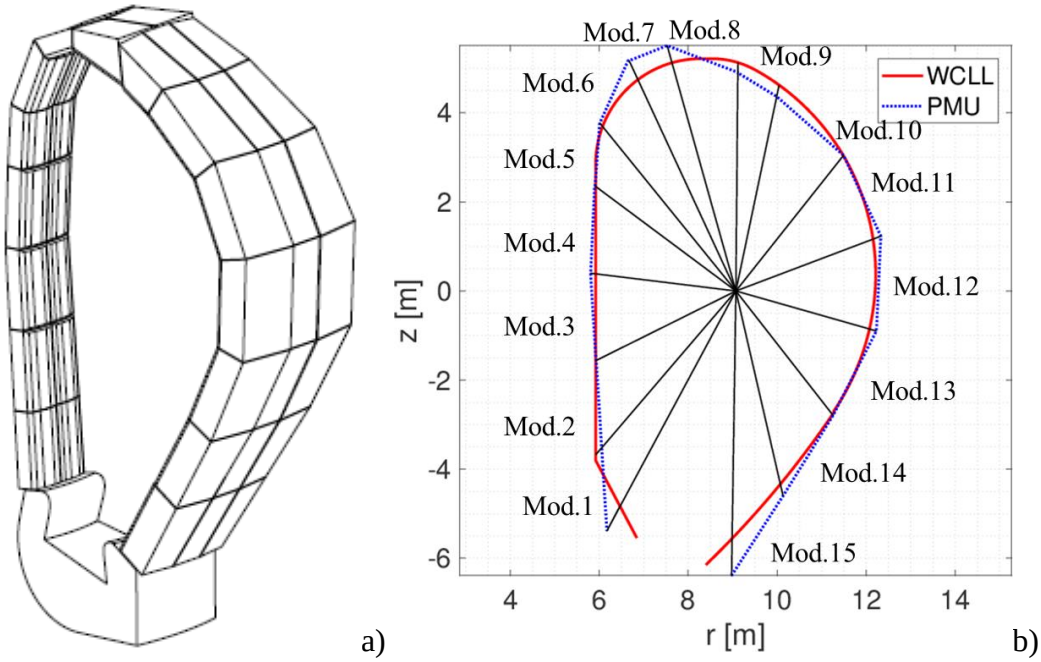

Figure 4.12: (a) 3D FW geometry used by the EUROfusion PMU to compute the plasma heat flux [56]. (b) Comparison of the 2D profiles of the WCLL (solid line) and PMU (dashed line) FWs, showing also the centre of the plasma and the ideal subdivision in modules.

The first issue is addressed by ideally splitting the WCLL SMS into 15 regions (identified as Mod. 1-15 in Figure 4.12b), in a way such that the lines connecting the edges between the different "modules" with the plasma centre coincide with those obtained on the PMU FW, as exemplified in Figure 4.12b. The second issue is solved by taking the total power on the three PMU segments and dividing it by

three, so that the WCLL SMS would be equivalent to the "average" PMU MMS. Finally, the third issue is solved by "spreading" the total power (coming from the integration of the PMU heat flux) on the WCLL "module". Those are evidently very rough assumptions, as the heat load coming from the plasma is anisotropic and is strongly affected by the FW shape itself; as also stated in [55], this heat load distribution determined by the PMU is meaningful only for the 2017 EU DEMO1 FW shape. On the other hand, it should be noted that the aim of this work is not to reshape the heat load distribution to the WCLL FW (which would require the use of plasma physics codes), but to analyse the effect of a deviation of the heat load distribution on the cooling performance of the WCLL FW; consequently, this rough redistribution is used in the present work. The resulting heat flux distribution is reported in Figure 4.13, together with its peak value, which may be deposited on small portions of the different regions (without affecting the total power) [55].

Simply looking at Figure 4.13 it is already possible to say that the most critical points will be located far from the equatorial plane (this is also consistent with what was found for the HCPB in section 4.2.1 above); this effect will also be more evident if considering the peak heat flux which, in Mod. 6 region, can be as high as 5× the design value.

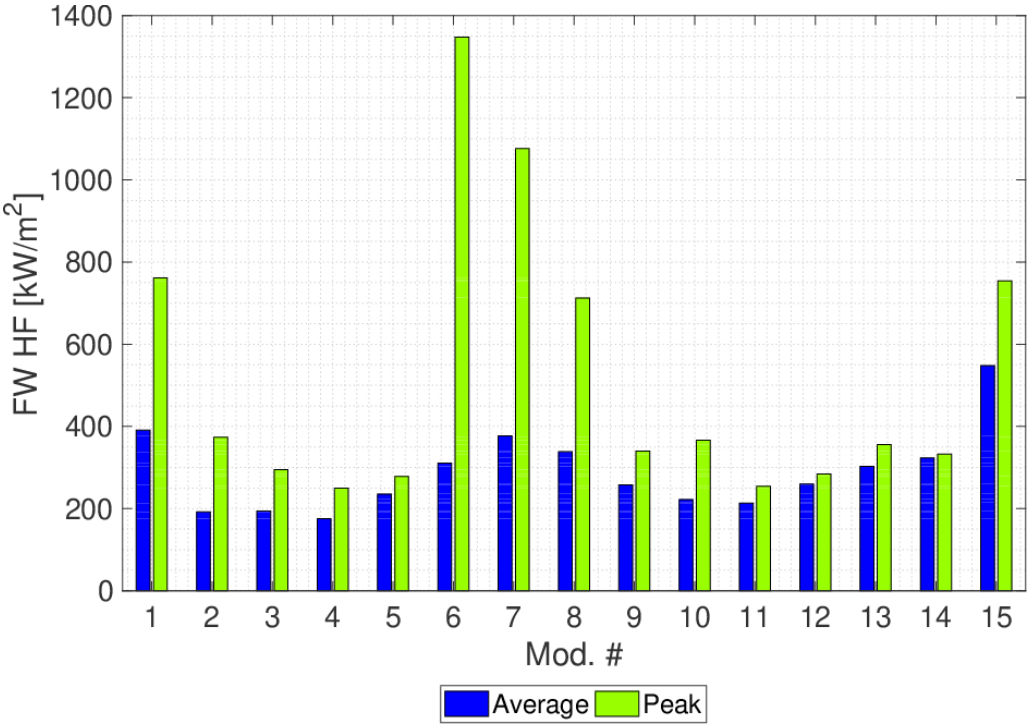

Figure 4.13: Average and peak plasma heat flux to the WCLL FW surface.

When applying this heat flux to the WCLL SMS, the total power to the IB and OB segment is also larger than the design value, increasing from 3.26 MW to 4.08 MW in the IB (+25 %) and from 6.49 MW to 7.71 MW in the OB (+19 %) [14]; also for this reason, different alternatives are investigated for the mass flow rate, starting from the design distribution [45], then redistributing it according to the PMU average heat flux, and finally increasing the total mass flow rate in order to match the increased total power deposition.

The different scenarios investigated are resumed in Table 4.6 and Figure 4.14: in scenarios 1 and 2 the mass flow rate is distributed according to WCLL design, and a sensitivity study is done on the HTC, using its average value among all the channels in scenario 1 and the minimum possible value in scenario 2 (this is a conservative assumption). In scenario 3 the total value of the mass flow rate is kept unmodified, but its distribution among the different regions is recalculated according to the PMU power distribution. Finally, in scenario 4 also the total value of the mass flow rate is changed, in order to reflect the mentioned increase of the total power deposition (i.e. so that the outlet temperature is set back to the design value of 328 °C).

As already discussed in section 4.2.1 above for the HCPB, all the results will be presented as steady state, as also in this case the characteristic timescales of the thermal phenomena are much shorter than the plasma burn phase. To compute the hot-spot EUROFER temperature postprocessing the GETTHEM results on the average solid temperature, the procedure described in Appendix A and already applied to the HCPB is adopted. The value of the shape factor used here is computed according to the 3D CFD study performed by the WCLL design team in an elementary unit at the OB equatorial plane [8].

Table 4.6: List of the analysed scenarios for the WCLL FW hot-spot study.

Scenario	***Mass flow rate***	***HTC***
1	Total value and distribution according to design data	**Average** value in entire segment
2	Total value and distribution according to design data	**Minimum** value in entire segment
3	Total value according to design data, distribution according to PMU power specifications	**Minimum** value
4	Total value and distribution recalculated according to PMU power specifications	**Minimum** value

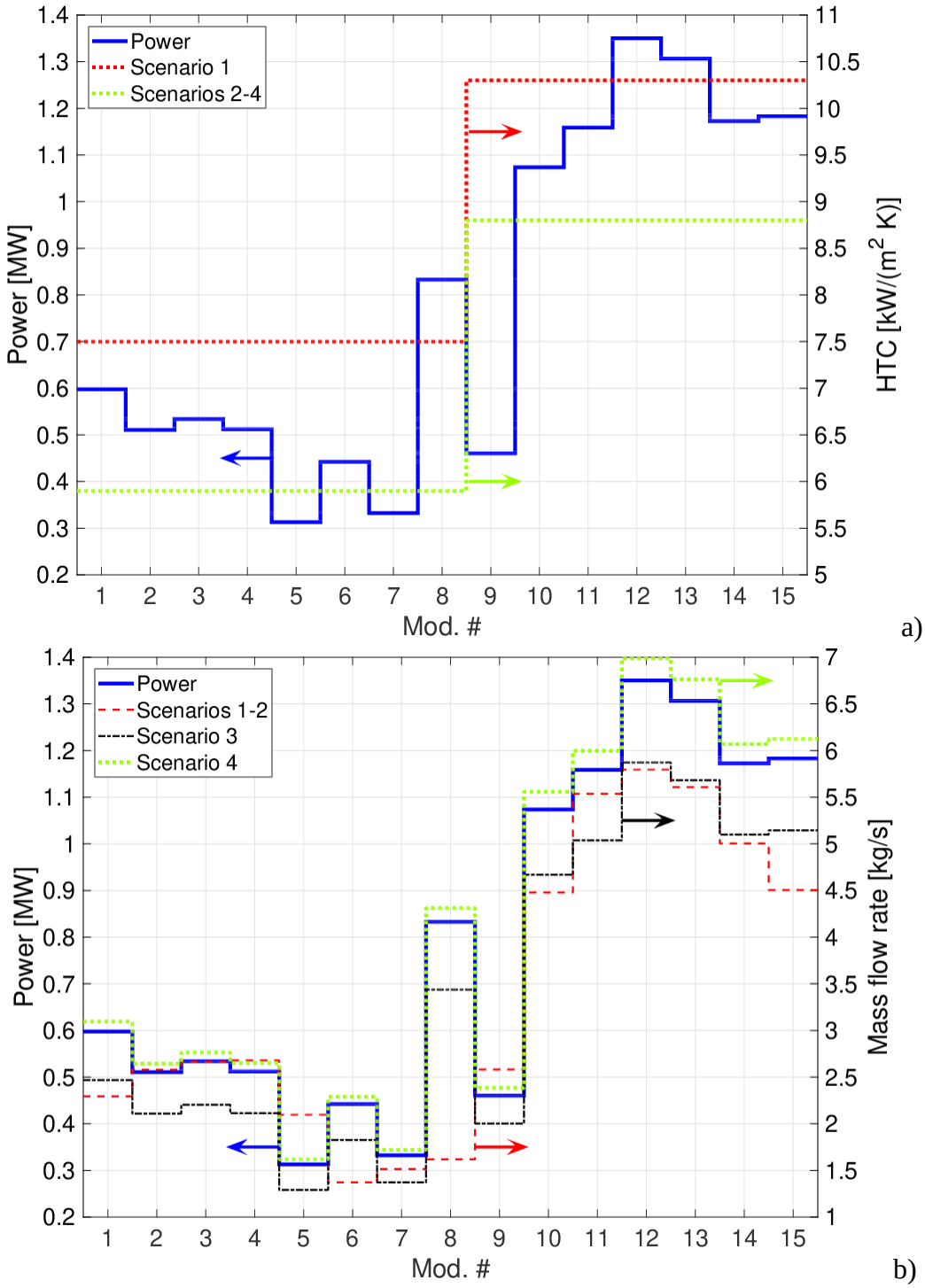

Figure 4.14: Poloidal distribution of power (solid lines, left axes), HTC (dashed lines, right axis in a) and mass flow rate (dashed lines, right axis in b) for WCLL FW hot-spot scenarios 1-4.

The poloidal distribution of the hot-spot EUROFER temperature is reported in Figure 4.15: as expected looking at the loads, the worst conditions are always found far from the OB equatorial plane, and particularly in the Mod. 8 region; nevertheless, the EUROFER temperature is always everywhere below the limit, even in scenarios 1-2 despite a non-optimized mass flow rate distribution. Comparing these two scenarios from a global perspective, it is evident how the assumption on the HTC has an effect which is not negligible, but still does not affect macroscopically the outcome. What is important also to notice in these two cases is that GETTHEM detected a temperature above saturation in Mod. 6 and in Mod. 8; since water is always assumed to be single phase liquid, its predictions in those regions may not be considered as accurate (albeit conservative) and call for further, more detailed analyses.

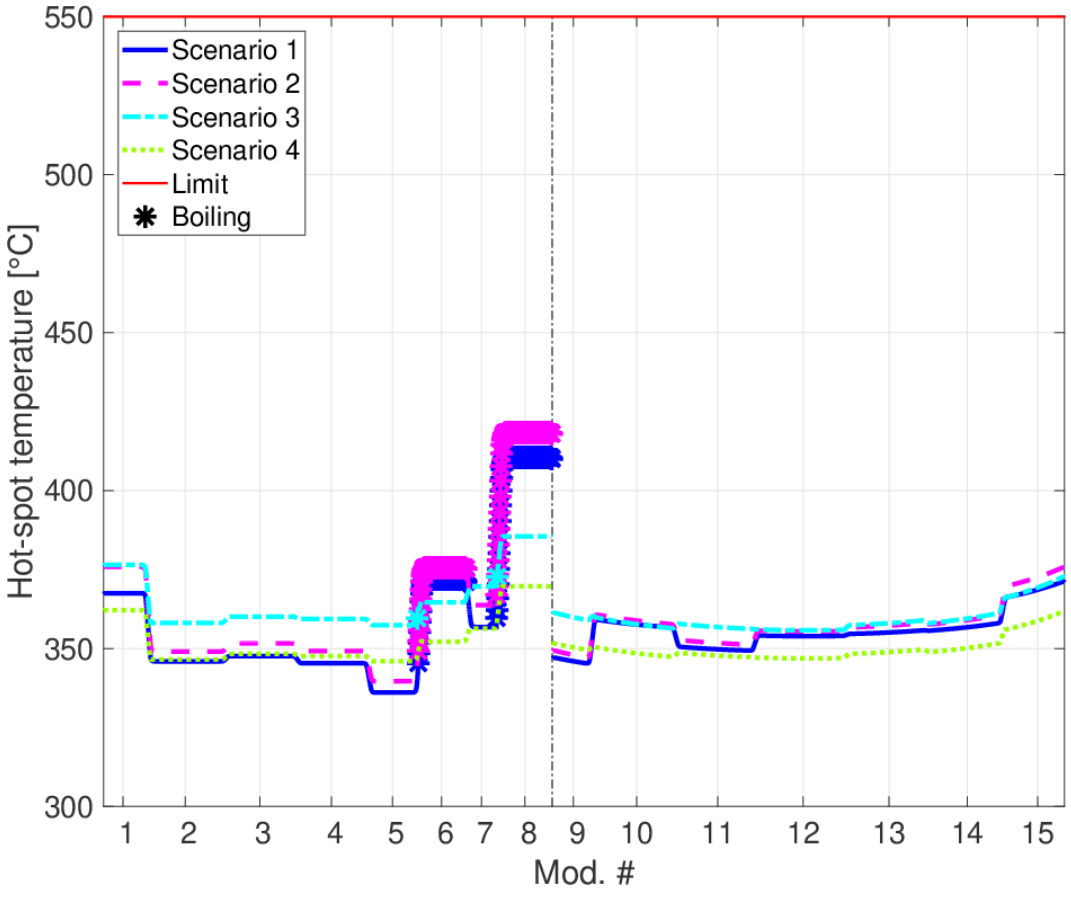

Figure 4.15: Poloidal distribution of the hot-spot temperature for WCLL FW hot-spot scenarios 1-4. The thin, red line represents the 550 °C limit; points marked with a star represent a poloidal position corresponding to channels where boiling was detected by the model.

Coming to scenarios 3 and 4, instead, thanks to the redistribution of the mass flow according to the power distribution, the temperature field in the BB is more uniform, with Mod. 8 and Mod. 15 still remaining the focus regions. The uniformity of the temperature distribution is particularly evident in the OB, thanks to a more uniform heat flux distribution.

Another feature which immediately comes out from Figure 4.15 is that on the IB the temperature distribution is almost piecewise constant, whereas it has a concavity on the OB: this is caused by the larger thermal conductance of the coupling in the OB, driven by geometry, which causes nearby channels (and consequently "modules") to influence with each other much more than in the IB, where the effect is also present but not visible on this scale.

Figure 4.16 reports the coolant outlet temperature for scenarios 3 and 4: since in this case the mass flow rate was redistributed according to the power distribution, the outlet temperature is uniform in IB and OB; in scenario 4, moreover, the mass flow rate value was also increased in order to have the design temperature increase, so that all the channels have the same outlet temperature of 328 °C.

Scenario 4 then proves that it is possible, with a relatively small increase in the coolant mass flow rate (which is not a concern in a water-cooled system), to keep the structures at a safe temperature with the PMU average heat flux, while at the same time having the target coolant outlet temperature; note also that no boiling is detected by GETTHEM in this scenario (nor in scenario 3).

Hence, taking scenario 4 as a reference, a parametric analysis is then performed, aimed at identifying which would be the largest possible FW surface to be loaded with the *peak* heat flux identified by the PMU (see Figure 4.13), without causing the FW to overheat above 550 °C. To this aim, the peak heat flux is applied to a progressively increasing number of FW channels (uniformly in the toroidal direction), until the hot-spot temperature overcomes the limit or boiling is detected.

Before this parametric analysis is performed, however, an *overconservative* scenario is considered, where the peak heat flux is applied to the *entire* BB (which consequently causes the total power to increase by 20 % on the OB and 80 % on the IB); in view of the peak heat flux distribution reported in Figure 4.13, the most critical points are expected to be in Mod. 1, 6-8 for IB and Mod. 15 for the OB.

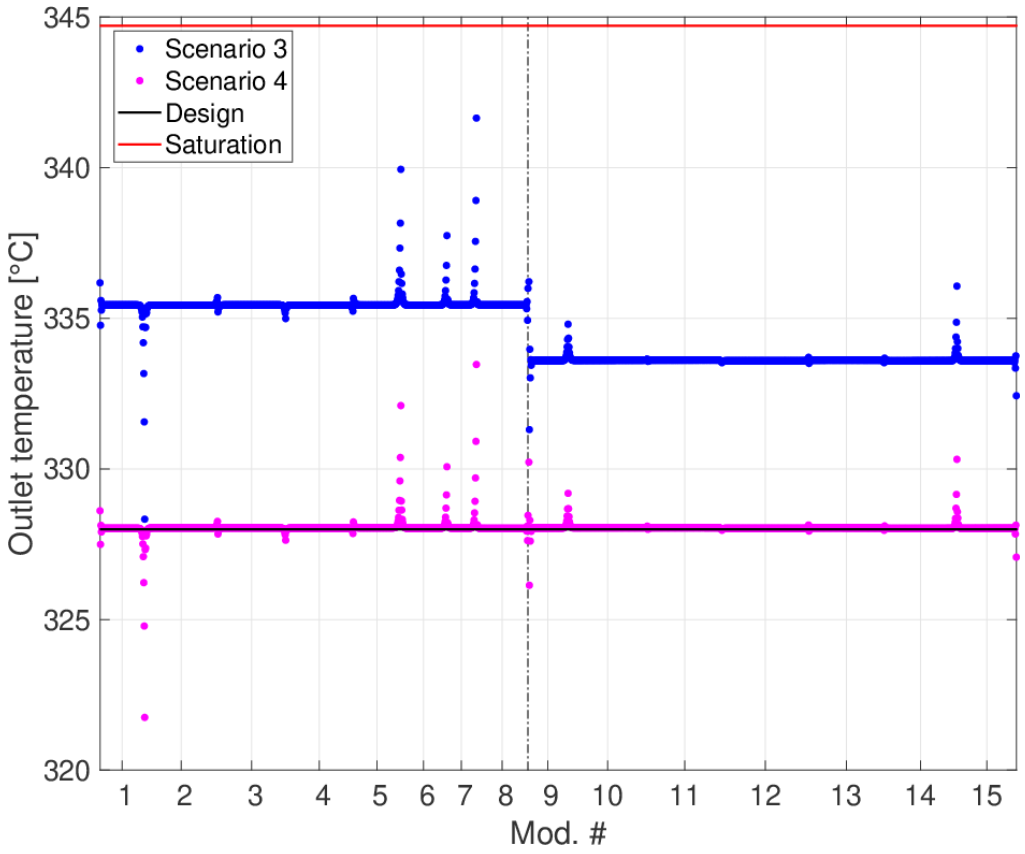

Figure 4.16: Poloidal distribution of the outlet temperature from the WCLL FW cooling channels, for scenarios 3 and 4. The thin, red line represents the saturation temperature, whereas the thin, black line represents the design outlet temperature (328 °C).

The result of this case is reported in Figure 4.17 (temperatures above 800 °C are cut in the figure, as they refer to channels where saturation temperature is largely overcome and GETTHEM predictions are not trustful): also in this overconservative scenario, all the regions (apart from the critical points identified above) show a EUROFER temperature within the working range; nevertheless, boiling is detected in Mod. 2 and 10, meaning that further, detailed investigations are advised in those regions. It should also be stressed that (apart from the mentioned boiling in Mod. 10) the OB is fully safe even in the overconservative case, as the EUROFER temperature limit is overcome only in the last 14 channels of Mod. 15; moreover, the peak temperature in this region is 558 °C, 3 % larger (with respect to the increase from 295 °C) than the limit, i.e. comparable with the estimated average GETTHEM error as reported in section 2.2.1 above.

The peak heat flux is then applied on an increasing number of channels in the middle of Mods. 1-2, 6-8, 10 and at the bottom of Mod. 15 (as the bottom part is

the most critical point of this region), until the EUROFER temperature overcomes the limit or saturation conditions are reached. When applying the peak heat flux to some channels, the total load to the other channels is reduced to keep the total power constant. The result of this analysis is reported in Table 4.7: in Mod. 6, which was expected to be the most critical point as the peak heat flux is ~1.4 MW/m², it is sufficient to apply it a single channel (i.e. ~0.013 m² of FW) to reach both conditions. Also in Mod. 8 the EUROFER temperature limit is overcome when loading a single channel, while boiling is detected when two channels are loaded; in all the other IB regions the situation is similar, as all the investigated regions do not respect (at least) one of the two constraints if at least five channels are loaded with the peak heat flux (Mod. 2 never reaches the temperature limit, as already identified in the overconservative scenario).

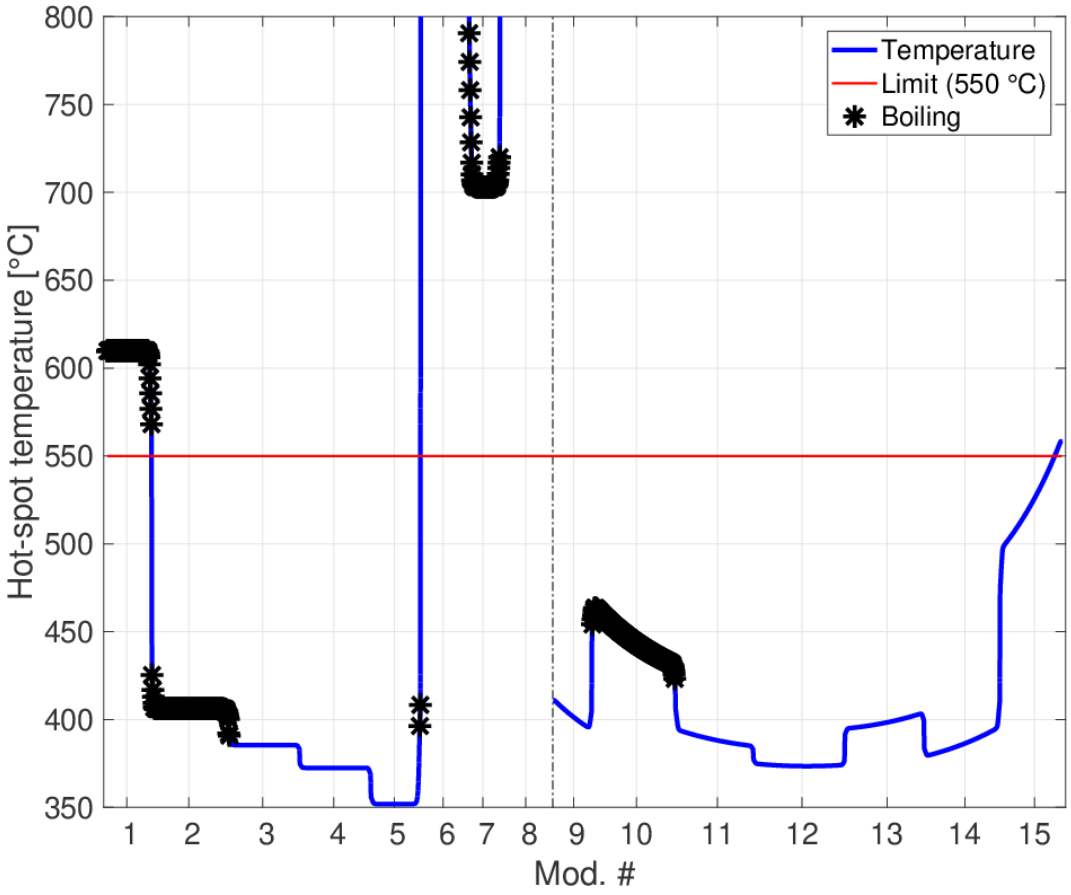

Figure 4.17: Poloidal distribution of the WCLL hot-spot temperature, when applying the peak heat flux to the entire BB. The thin, red line represents the 550 °C limit; points marked with a black star represent a poloidal position corresponding to channels where boiling was detected by the model.

Considering the OB, the situation slightly improves: in Mod. 10 boiling is in fact detected when at least 8 channels are loaded, while the EUROFER temperature never reaches the limit; for Mod. 15, instead, the latter condition is found as soon as at least 9 channels are loaded, while saturation is never reached. It should be recalled again that the EUROFER hotspot temperature overcomes the limit very slightly: in this particular case, it is overcome only in the last channel of the OB segment, and by less than 1 °C.

Table 4.7: Results of the parametric analysis for the WCLL FW hot-spot study.

Region	***Number of channels loaded with peak heat flux which cause:***	
	Boiling	$T_{hotspot}$ **> 550 °C**
Mod. 1	3	6
Mod. 2	5	-
Mod. 6	1	1
Mod. 7	2	4
Mod. 8	2	1
Mod. 10	8	-
Mod. 15	-	9

4.3. Parametric analysis of an in-vessel Loss-Of-Coolant-Accident

The GETTHEM module for VVPSS analyses described in section 2.3.2 above is here applied to study different in-VV LOCA scenarios, for both HCPB and WCLL. The initiating event for the first scenario is assumed to be a beam of runaway electrons impacting the FW, causing a toroidally continuous strip of 10 m² of FW surface at the OB equatorial plane to melt down [57]; taking into account the toroidal dimension of the OB4 in the 2015 EU DEMO1 design (1.424 m [3]), the number of sectors in the whole BB (18), and the number of OB segments for each sector (3), the height of the melting surface in the FW is approximatively 130 mm (computed as $10\ \mathrm{m}^2/(1.424\ \mathrm{m} \times 18 \times 3)$). Due to the proximity of the FW cooling channels to the FW, all the channels below the melted surface are supposed to be exposed to the plasma volume as the FW surface melts.

In this scenario (hereafter called the 2015 scenario), the parameters for the RLs are taken from the ITER design of the VVPSS [58], i.e. a single RL with a cross section of 1 m² + 2 BVs of 0.1 m², with a set-point of 150 kPa (differential pressure)

for the BD and 90 kPa (differential pressure) for the BVs. Concerning the helium EV, a volume of 120000 m³ is considered, with an initial pressure of 4.2 kPa (according to [39]), whereas for the water SP a total volume of 1107 m³ is assumed, initially filled at 50 % level by water at 2.34 kPa (i.e. at saturation conditions at 20 °C; these values are taken from [59]).

After the 2015 scenario, a parametric study is performed, to analyse which would be the largest possible break size of the FW that can be accommodated by the most recent VVPSS design. In this case, a more realistic assumption for the RLs, EV and SP is assumed: in fact, the most recent hypothesis for the routing of the RLs is through the Neutral Beam Injector (NBI) equatorial ports, which give a cross section of 0.7×0.7 m² each (see Figure 4.18); the cases with two and three RLs routed through just as many NBI ports are considered. Since a fourth equatorial port close to the NBI is also free (due to the NBI inclination), an additional case, with four RLs of 0.7×0.7 m² is also considered. Concerning the helium EV, the current idea is to make it expand freely in some parts of the reactor building, so a free volume of 60700 m³ is assumed [60]; finally, for the water SP a volume of 2000 m³ is considered, according to the VVPSS design which is currently being integrated in the DEMO plant layout [60], initially filled at 50 % level by water at 4.2 kPa (i.e. saturation pressure at 30 °C).

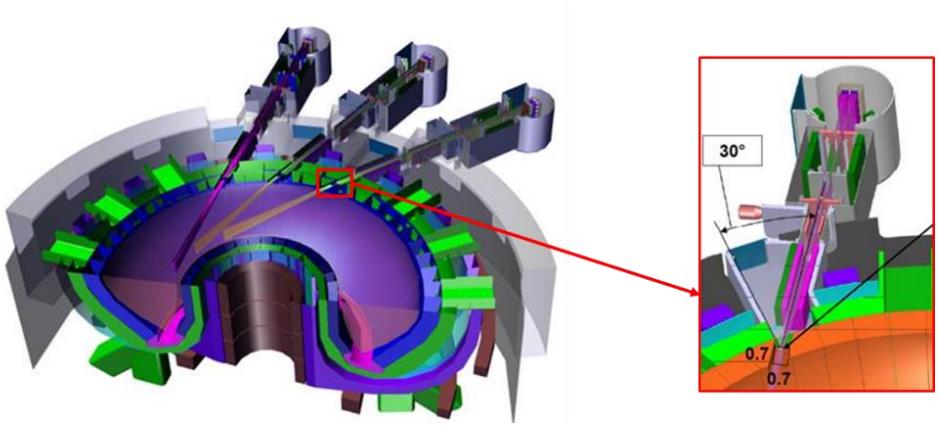

Figure 4.18: Position of the NBI ports in the 2015 EU DEMO1 design and cross section available for the coolant discharge [61].

Different surfaces of melting FW (0.01 m², 0.1 m², 1 m², 2 m² and 5 m²) are considered in this parametric study. The number of channels and the number of cooling loops which are involved by the FW melting are evaluated considering two different directions of propagation of the energy deposition on the FW surface: po-

loidal (see Figure 4.19a) and toroidal (see Figure 4.19b), respectively. The evaluation of the involved number of BMs (and, consequently, channels) is performed considering that the energy released on the surface of the FW is deposited only on the lateral (filleted) region of the modules which lies on the melting area involved. The filleted edge of the BM (red region in Figure 4.19c), indeed, is facing the field lines of the plasma almost orthogonally and it is subject to a more relevant heat flux if compared to the frontal surface of the module that is almost parallel to the field lines.

Taking into account the different break size dimensions and the two energy deposition directions, 86 cases have been identified for helium-cooled design and 44 for water-cooled design, considering the different characteristics of the two BB concepts and their PHTS. Among all, 10 scenarios for the HCPB and 5 scenarios for WCLL are identified as the most representative ones, because many cases showed similar values as far as the released inventory and the break size dimensions are concerned.

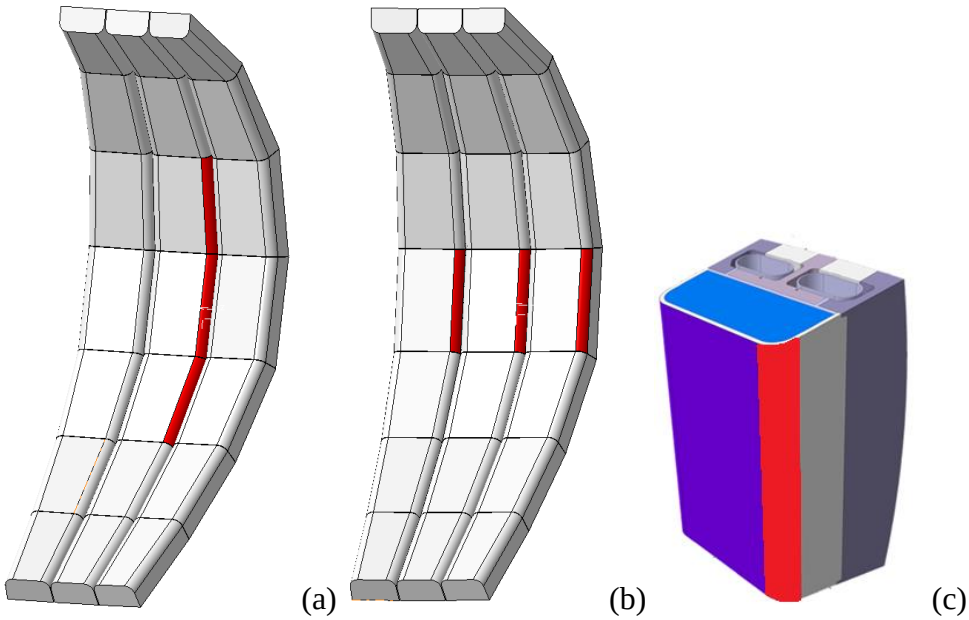

Figure 4.19: (a) poloidal and (b) toroidal energy deposition on the FW; (c) filleted edge of the BM (in red) which is heated by the runaway electrons (adapted from [7]).

Finally, in both cases (2015 scenario and parametric study), and for both BB concepts, the decay heat is not considered; even though this is a non-conservative assumption, it has already been shown in [39, 59] that its effect on the pressure

evolution in the VV is non-negligible only in the long term, leaving almost unaltered the pressure peak therein (which is the object of this work).

4.3.1. Helium-Cooled Pebble Bed

2015 scenario

Considering that in the 2015 HCPB design [7] the FW channels have a square cross section of 12.5×12.5 mm² and a pitch of 17 mm [7], with a break as high as 130 mm the number of channels involved is 8 (computed as $\lceil 130/17 \rceil$). The discharge area in the VV is evaluated taking into account, for the number of involved channels, their cross section and the double ended guillotine characteristic of the rupture, which doubles the cross section available for coolant discharge. Hence, the resulting total cross section involved in the HCPB in-VV LOCA is 0.135 m².

The parameters used in the simulation are reported in Table 4.8; the scenario is identical to the calibration scenario described in section 3.3 above; the only differences are found in the PHTS and VV volumes, which are set to DEMO-relevant values [62, 63], and in the break cross section, which is set to the value computed above. Consequently, the evolution of the relevant variable is expected to be qualitatively similar with respect to the calibration scenario; since the PHTS volume is reduced, the VV volume is increased and the break cross section is reduced, a lower pressure peak is expected.

As expected, the evolution of the considered variables is very similar to those found for the calibration, as visible in Figure 4.20 for the pressure and Figure 4.21 for the temperature; in fact, the only differences with respect to the calibration scenario are the PHTS volume and the break cross sections, which are reduced from 2325 m³ to 1497 m³, and from 0.2 m² to 0.135 m², respectively, and the VV volume, which increases from 2243 m³ to 3000 m³. In all the three cases, the effect is to reduce the peak pressure in the VV: in fact, the smaller PHTS volume means that there is less coolant mass available to fill the VV (as pressure and temperature are the same), while a smaller break translates to a lower mass flow rate from PHTS to VV, as visible in Figure 4.22a. Finally, the larger VV volume allows for a slower pressure increase inside the VV. All of these factors contribute to reduce the peak pressure to 571 kPa, which is still ~3× higher than the pressure limit but almost twice as smaller than in the calibration scenario. The temperature evolution, being linked to the pressure by the ideal gas law, also sees a small reduction of the peak temperature in the VV, with a value of ~1100 K. The temperature in the EV at the

end of the transient is still high (~730 K), calling for an additional heat sink (such as forcing the helium to flow through a cool water pool), which, by reducing the helium temperature, would allow reducing the volume needed by the EV (as density is inversely proportional to temperature in the ideal gas law).

Table 4.8: Value of the parameters used in the EU DEMO HCPB in-VV LOCA 2015 scenario.

Parameter	*Value*	*Notes / references*
PHTS		
Volume [m³]	1497	[62]
Initial pressure [MPa]	8	[7]
Initial temperature [K]	673	Average inlet/outlet value [7]
Break		
Cross section [m²]	0.135	See discussion above
VV		
Volume [m³]	3000	[63]
Burst disks		
Number	1	Same as ITER VVPSS
Cross section [m²]	1	Same as ITER VVPSS
Opening differential pressure [MPa]	0.15	Same as ITER VVPSS
Bleed valves		
Number	2	Same as ITER VVPSS
Cross section [m²]	0.1	Same as ITER VVPSS
Opening differential pressure [MPa]	0.09	Same as ITER VVPSS
EV		
Volume [m³]	120000	[39]
Initial pressure [kPa]	4.2	[39]

Figure 4.22b shows a zoom of the mass flow rate during the first 0.5 s of the transient; it is evident how the BLs open after ~0.21 s, but the flow rate they discharge into the EV is a very small fraction (less than 2 %) of that incoming into the VV, so that no pressure reduction is visible. On the contrary, after ~0.36 s also the BD opens, discharging a much higher flow rate and starting to reduce the pressure increase in the VV, although still not effectively enough to limit the pressure peak below the design limit of 200 kPa.

Figure 4.23 to Figure 4.25 report the evolution of pressure (left axis) and temperature (right axis) in the PHTS, VV and EV, respectively. The main results of the

calculation, in terms of peak and final pressures and temperatures in the three volumes, are reported in Table 4.9.

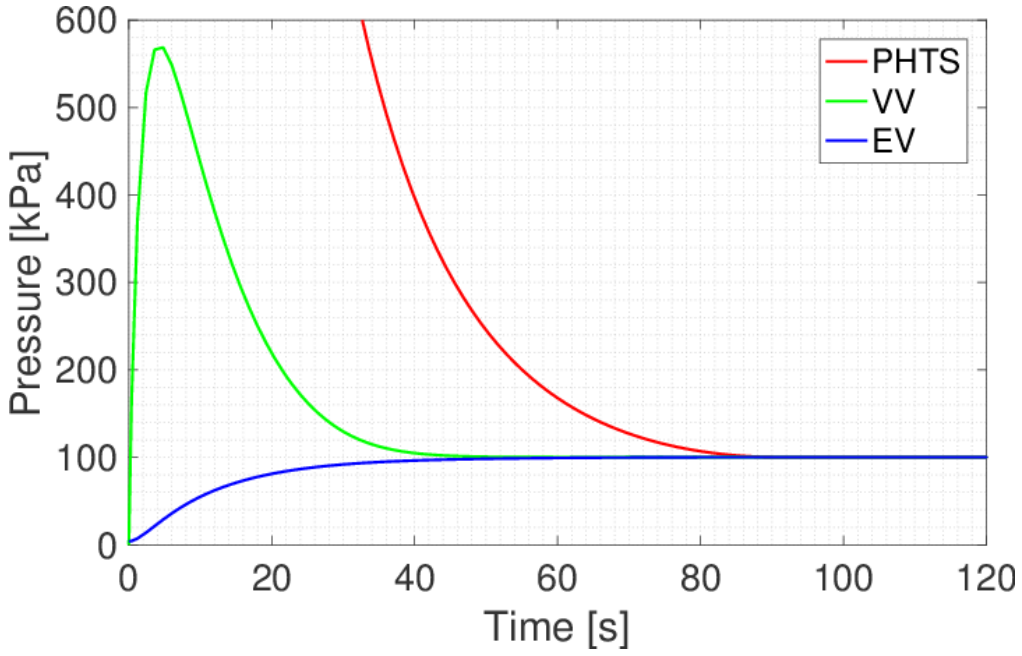

Figure 4.20: Computed evolution of the pressure in the three considered volumes, for the HCPB in-VV LOCA 2015 scenario.

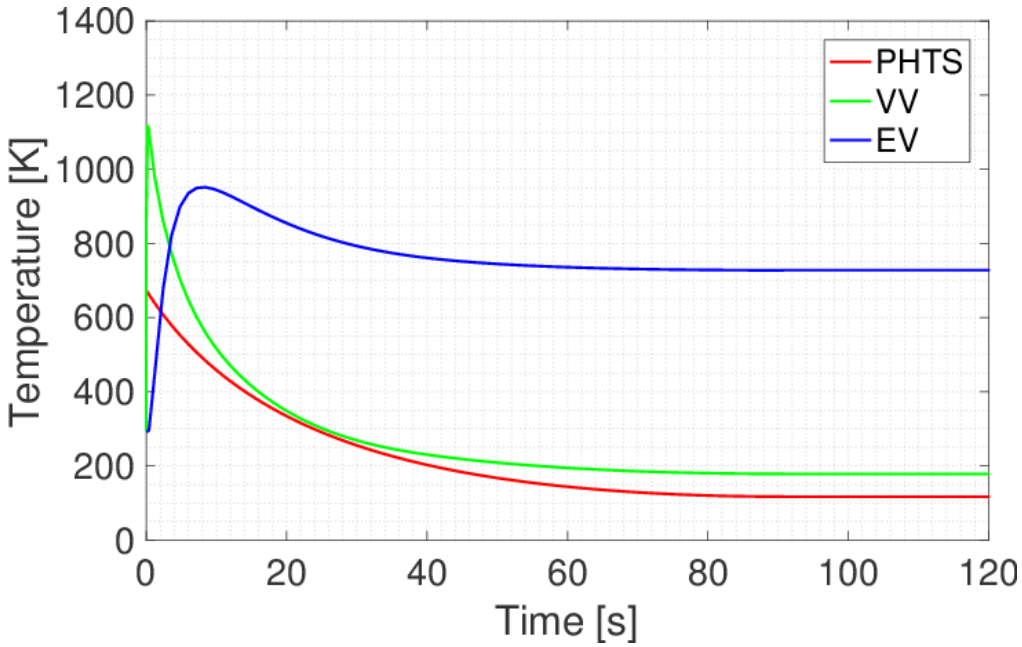

Figure 4.21: Computed evolution of the temperature in the three considered volumes, for the HCPB in-VV LOCA 2015 scenario.

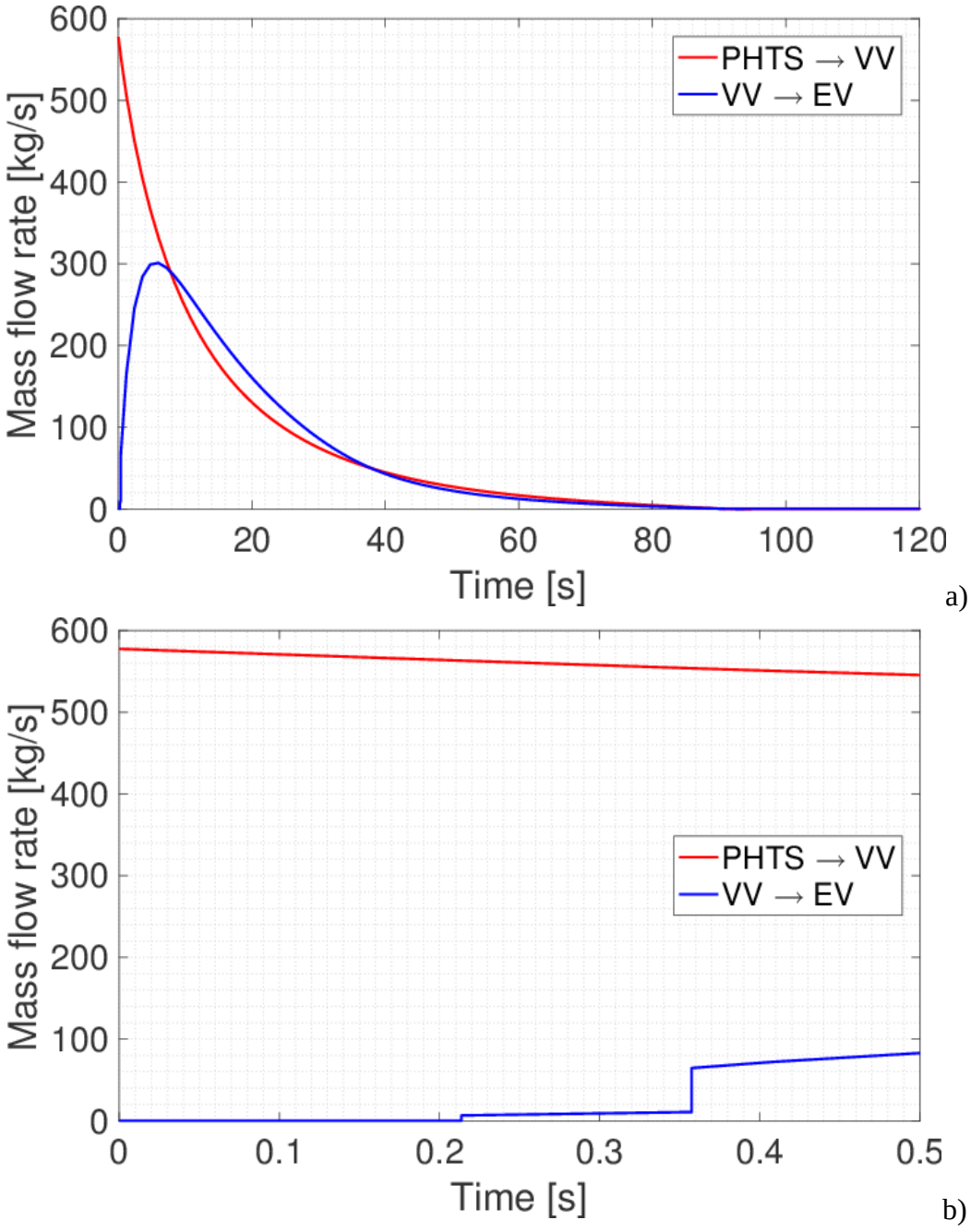

Figure 4.22: a) computed evolution of the mass flow rate from PHTS to VV and from VV to EV, for the HCPB in-VV LOCA 2015 scenario; b) zoom of the mass flow rates during the first 0.5 s.

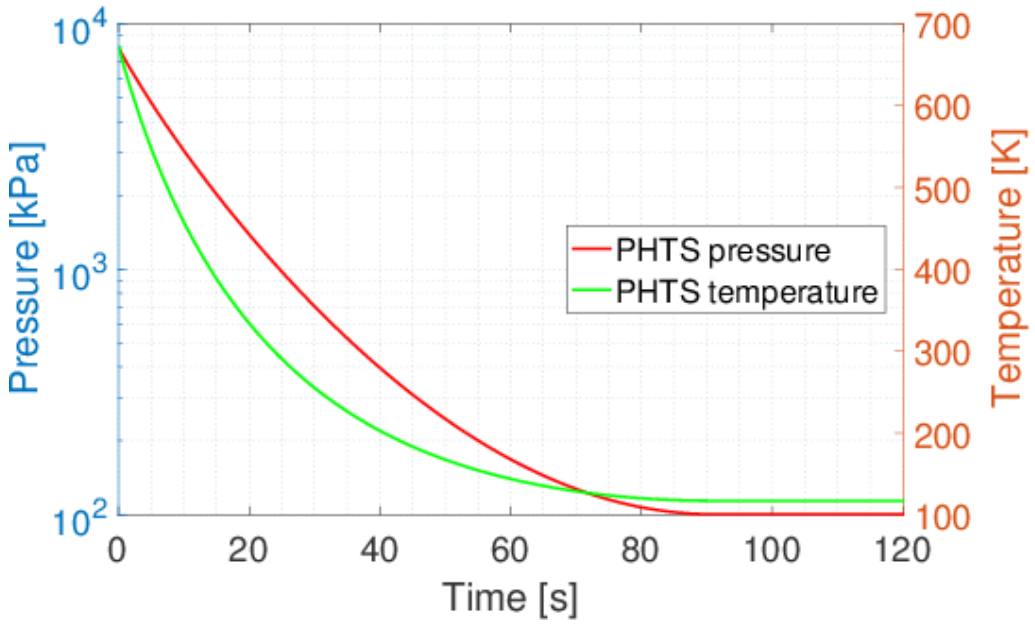

Figure 4.23: Computed evolution of pressure (left axis) and temperature (right axis) in the PHTS, for the HCPB in-VV LOCA 2015 scenario.

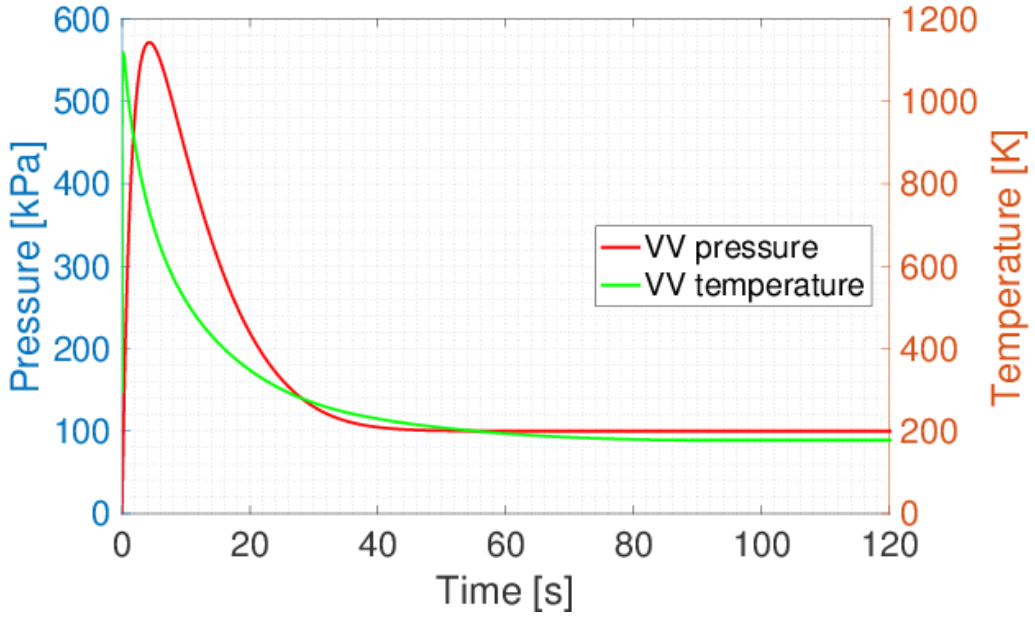

Figure 4.24: Computed evolution of pressure (left axis) and temperature (right axis) in the VV, for the HCPB in-VV LOCA 2015 scenario.

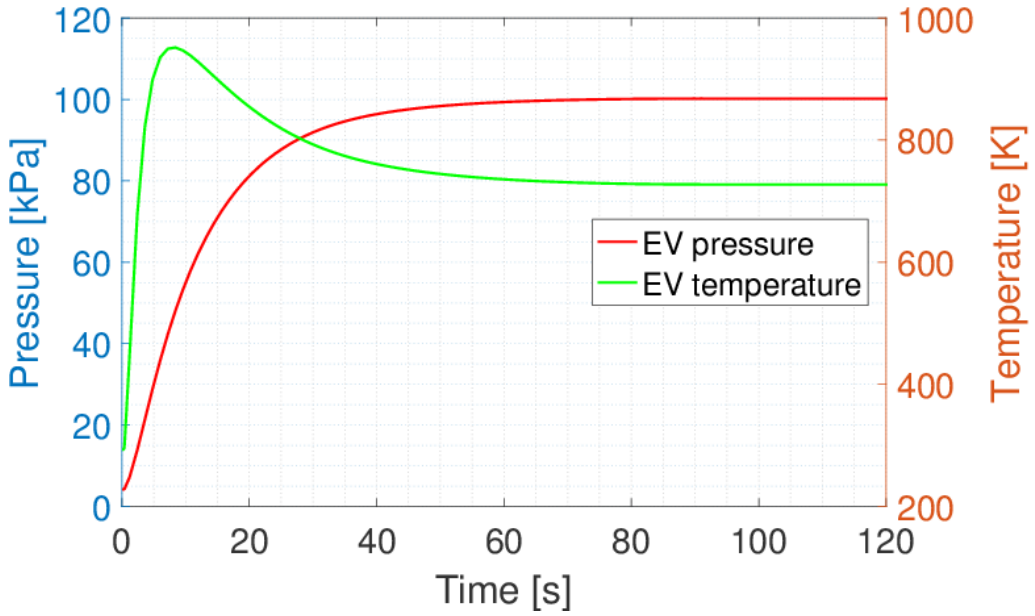

Figure 4.25: Computed evolution of pressure (left axis) and temperature (right axis) in the EV, for the HCPB in-VV LOCA 2015 scenario.

Figure 4.26 compares the evolution of pressure in the three volumes (left axis) and the evolution of the mass flow rates (right axis). In the first part of the transient, the pressure difference between PHTS and the rest of the system leads to a very high mass flow rate from the PHTS to the VV. In this time interval, the pressure in the VV rises up to the maximum value. Simultaneously, the pressure difference between VV and EV increases, as well as the mass flow rate between the two volumes after the BVs and BD opening.

The pressure peak value in the VV is reached approximatively when the mass flow rate from VV to EV overcomes the mass flow rate from PHTS to VV (the presence of the connection between VV and EV causes the anticipation of the pressure peak due to the simultaneous pressure increment in the EV). After around 10 s from the beginning of the transient, the mass flow rate from VV to EV overcomes the mass flow rate from PHTS to VV and, consequently, the pressure in the VV decreases until it reaches the same pressure in the EV, which on the other hand continues to increase as the discharge of coolant from the PHTS continues. After ~40 s, the two mass flow rate values are almost coincident, and VV and EV start following the same transient up to the steady-state conditions. The PHTS continues to inject coolant into VV and EV up to the pressure equilibrium is reached in the three volumes (~90 s), which leads to the conclusion of the transient event.

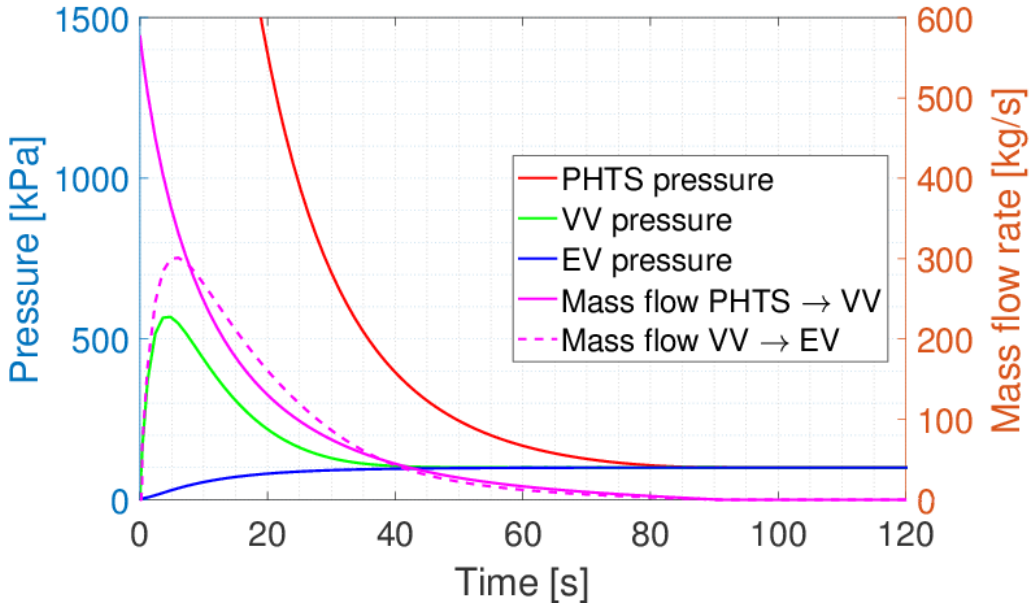

Figure 4.26: Computed evolution of the pressure and mass flow rates in the three considered volumes, for the HCPB in-VV LOCA 2015 scenario.

In Figure 4.27 the evolution of the stored mass is reported (the EV mass is plotted as increment with respect to the initial value, which, from the helium density at 4.2 kPa and room temperature, is ~828 kg); at steady state, the mass distribution reflect the different volumes; it is important to note how the mass content in the VV, after the initial increase due to the release of the gas from the PHTS, faces a reduction in the second phase, when the helium outflowing to the EV is more than that incoming from the PHTS, as visible from Figure 4.22a. After ~35 s, the VV and EV have almost the same pressure, so the VV mass increases again, driven by the release of mass from the PHTS.

Figure 4.28 shows the evolution of the energy stored inside the three volumes during the transient; almost all the energy goes to the EV at the end of the transient, highlighting again the need for an additional heat sink, which may slowly remove part of this energy, reducing the energy content in the EV at the end of the transient; moreover, it shows how the VV energy never reaches values higher than the EV, apart from a short period during the initial pressurization; this is mainly due to the value of mass stored in the VV, which never reaches a significant value.

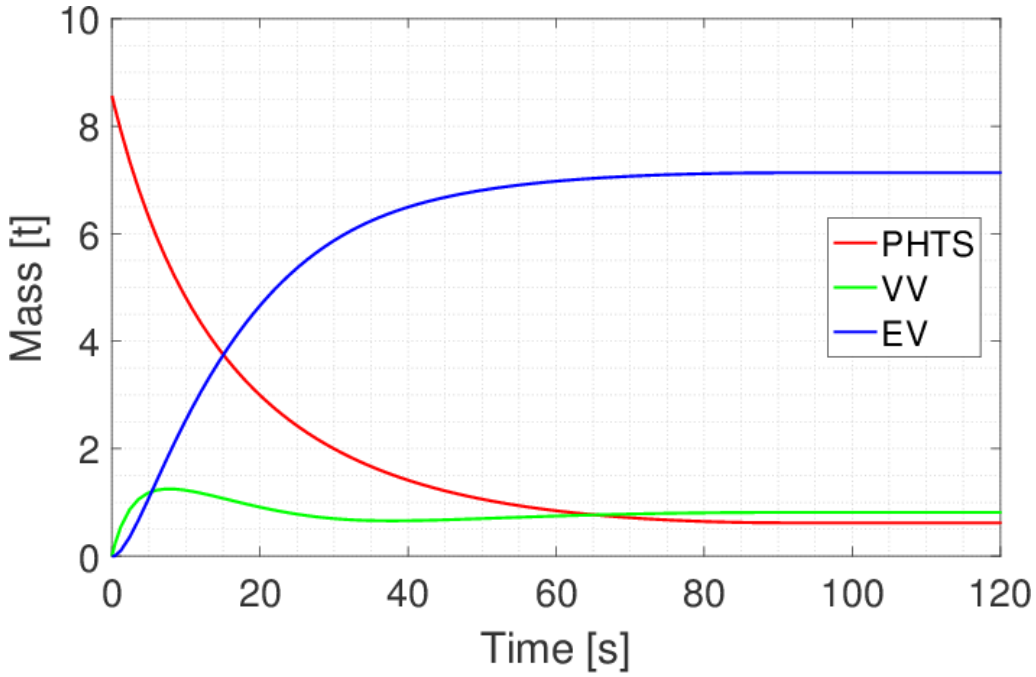

Figure 4.27: Computed evolution of the mass stored in the three considered volumes, for the HCPB in-VV LOCA 2015 scenario. The EV mass is plotted as increment with respect to the initial value.

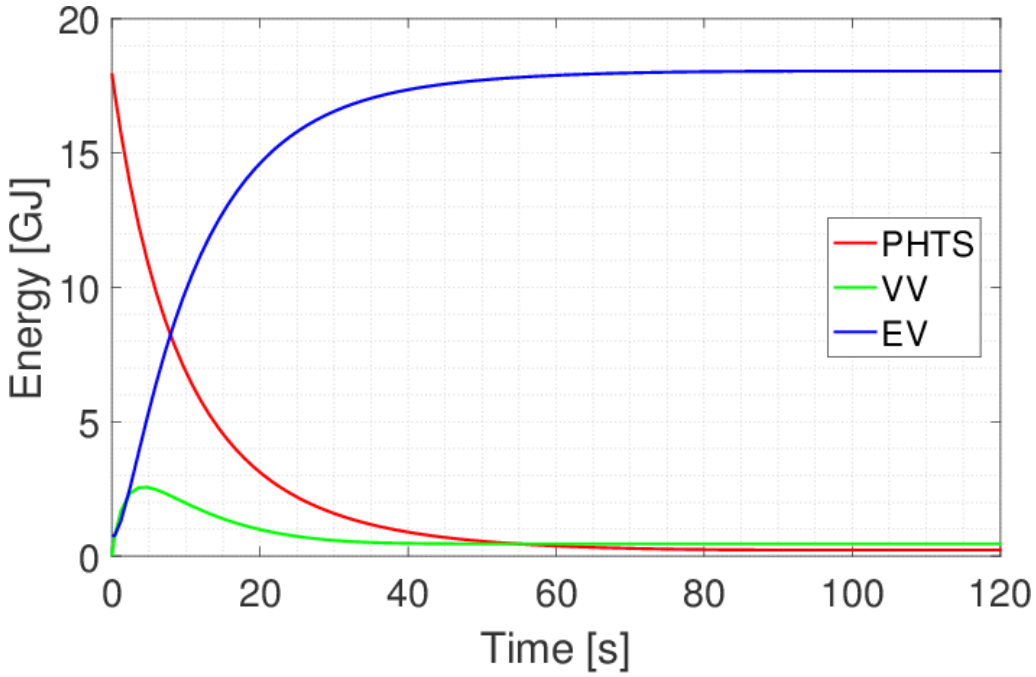

Figure 4.28: Computed evolution of the energy stored in the three considered volumes, for the HCPB in-VV LOCA 2015 scenario.

Table 4.9: Resume of the main results of the HCPB in-VV LOCA 2015 scenario.

Volume	***Pressure [kPa]***		***Temperature [K]***	
	Peak	*Final*	*Peak*	*Final*
PHTS	8000		673	117
VV	571	100	1120	178
EV	100		952	727

Parametric analysis

For the parametric analysis, all the parameters have the same value as in the 2015 scenario, with the exception of the values mentioned in the introduction to section 4.3, i.e. break cross section, number of RLs and EV volume (reduced from 120000 m³ to 60700 m³); moreover, it is here assumed that one BV is available for each BD, so that the number of BVs and BDs is identical. Finally, the inventory released to the VV from the PHTS is different from case to case, as it depends on the number of loops involved (i.e. on the number of segments); when more than one segment is involved, always the most conservative assumption is considered, maximizing the released inventory (e.g. if two segments are involved, it is assumed that they refer to two PHTS loops, even though this has a probability of 1/9). When two loops are involved, the model used is that represented in Figure 2.15.

The cases analysed in this parametric study are listed in Table 4.10. In cases 7-8 (as well as 9-10), the total break size and released inventory is the same, but they differ according to the repartition of break size between the two loops: in particular, since four segments are involved (9 in cases 9-10), the two extreme situations are investigated, i.e. (almost) equal repartition of the break size between the two loops (cases 7 and 9), and most unbalanced repartition (cases 8 and 10, see notes in Table 4.10).

Cases 3-5 refer to the energy deposition in poloidal direction, whereas cases 6-10 refer to the energy deposition in toroidal direction (see introduction to section 4.3 above). Cases 1-2, with 0.01 m² and 0.1 m² of FW break size, only involve a fraction of a BM, so there is no distinction between poloidal and toroidal direction of propagation; they are grouped with cases 3-5 in the results just for the sake of clarity.

Table 4.10: Cases analysed for the HCPB in-VV LOCA parametric analysis.

Case #	***FW break size [m²]***	***# channels involved***	***Discharging area [m²]***	***Inventory involved [m³]*** [11]
1	0.01	3	9.375×10^{-4}	290 (1 loop)
2	0.1	21	6.563×10^{-3}	290 (1 loop)
3	1	210	6.563×10^{-2}	290 (1 loop)
4	2	418	1.306×10^{-1}	290 (1 loop)
5	5	1031	3.222×10^{-1}	547 (2 loops)
6	1	208	6.500×10^{-2}	547 (2 loops)
7*	2	416	1.300×10^{-1}	547 (2 loops)
8&	2	416	1.300×10^{-1}	547 (2 loops)
9%	5	1039	3.247×10^{-1}	547 (2 loops)
10#	5	1039	3.247×10^{-1}	547 (2 loops)

* Loop 1 has a break size of 7.813×10^{-2} m²; loop 2 has a break size of 5.188×10^{-2} m².
& Loop 1 has a break size of 1.172×10^{-1} m²; loop 2 has a break size of 1.281×10^{-2} m².
% Loop 1 has a break size of 1.563×10^{-1} m²; loop 2 has a break size of 1.684×10^{-1} m².
# Loop 1 has a break size of 3.125×10^{-1} m²; loop 2 has a break size of 1.219×10^{-2} m².

The results of this study are reported in Figure 4.29, in terms of time evolution of the VV pressure. It is immediately evident that, with the given parameters for the VVPSS, any FW break size >1 m² (cases 4-5 and 7-10) is unacceptable if the pressure limit for the VV is not increased: in fact, even if using 4 RLs the peak pressure reached in the VV is above 200 kPa, albeit slightly in case 4. On the other hand, any FW break size <1 m² is acceptable, and the two investigated cases (1 and 2) do not even cause rupture of the BDs, even with 2 RLs only. Both 1 m² cases (3 and 6) are in the middle, as the pressure limit is overcome in those cases if using 2 RLs but not if using 4 RLs. With 3 RLs, case 3 is safely below the limit, whereas case 6 has a peak larger than 200 kPa, even if this is overcome by 7 kPa only.

Comparing cases 7-8 and 9-10 in Figure 4.29b, it is possible to highlight that, when different loops are involved, the worst case is when the break is almost equally partitioned between the two (as in cases 7 and 9). In fact, since the entire inventory can flow through a relatively large break size, a higher pressure peak is reached, with a difference up to ~30 %; on the other hand, if the break is unbalanced between the two loops, the one with the smallest break size has a negligible bearing on the first part of the transient and becomes relevant only after the BDs are open (i.e. the initial part of the transient is driven by one volume only). As a consequence, the peak is lower, but is reached before, as the break size through which the coolant flows at the beginning is ~2× larger.

The main results of this study are summarized in Table 4.11, reporting for each case the peak pressure in the VV ($p_{VV,peak}$), together with the time when the peak is reached (t_{peak}), for the three different numbers of RLs available (2/3/4 RLs).

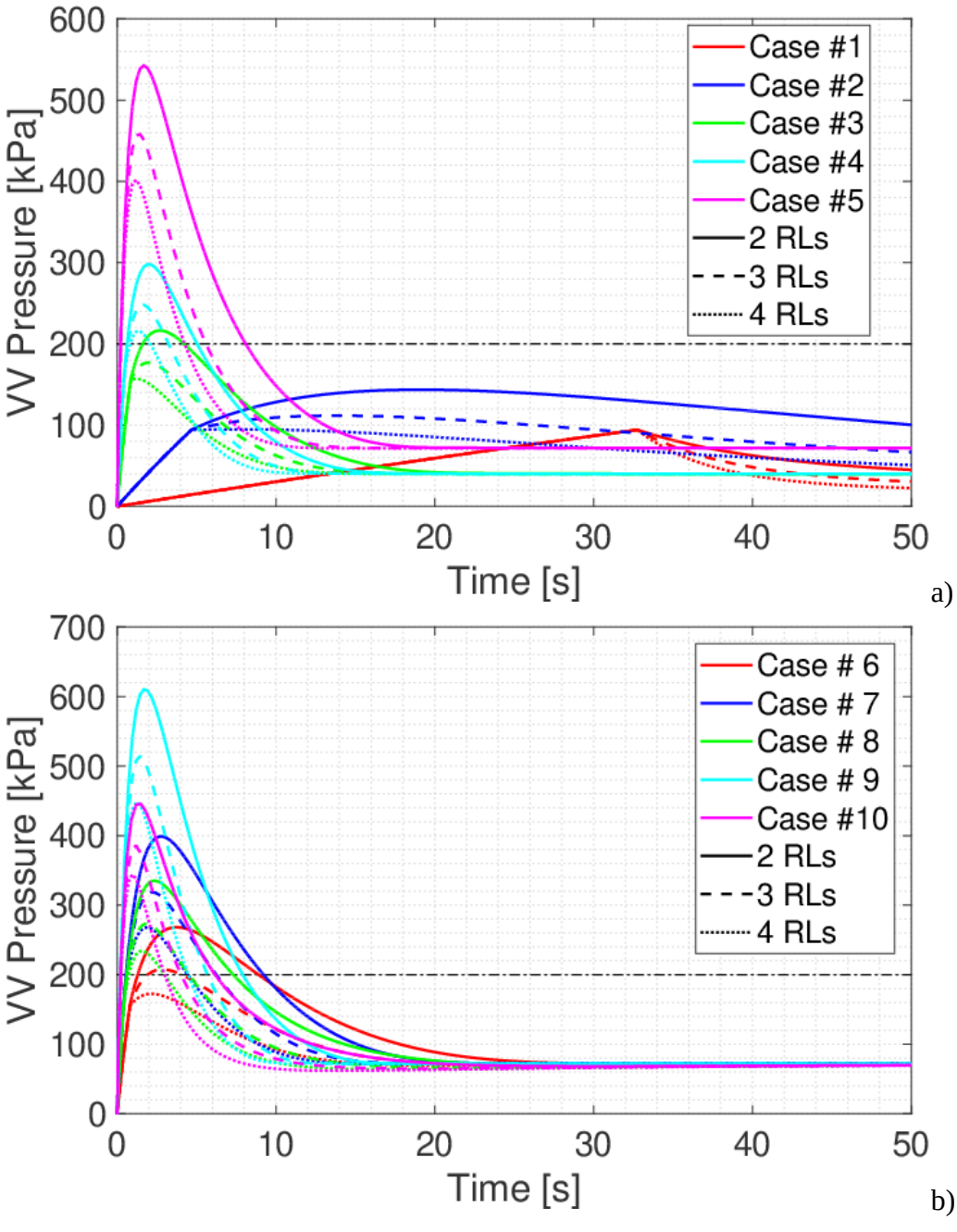

Figure 4.29: Computed evolution of the VV pressure for the HCPB in-VV LOCA parametric analysis, for cases 1-5 (a) and 6-10 (b). Different colours refer to different cases, whereas different line styles refer to a different number of RLs. The thin, black, dash-dotted lines represent the VV pressure limit (2 bar).

Table 4.11: Results of the HCPB parametric in-VV LOCA analysis, with 2/3/4 RLs. Peak values above the limit (200 kPa) are marked with red colour, whereas values below the limit are marked with green colour.

Case #	*FW break size [m²]*	$p_{VV,peak}$ *[kPa]*	t_{peak} *[s]*
1	0.01	94/94/94	33/33/33
2	0.1	144/112/94.7	19/14/8
3	1	217/177/157	2.6/2/1.2
4	2	298/248/216	2/1.6/1.3
5	5	541/457/402	1.6/1.4/1.2
6	1	268/207/173	3.8/2.8/2.2
7	2	399/318/268	2.8/2.2/1.8
8	2	335/273/234	2.4/2.9/1.5
9	5	612/514/450	1.7/1.4/1.2
10	5	445/385/344	1.4/1.2/1.0

4.3.2. Water-Cooled Lithium-Lead

2015 scenario

Considering 130 mm of melted FW (see introduction to section 4.3 above) and a pitch between the channels of 13.5 mm [8], the total number of involved channels is 10, computed as $\lceil 130/13.5 \rceil$. The discharge area in the VV is evaluated taking into account, for the number of involved channels, their cross section (7×7 mm²) and the double ended guillotine characteristic of the rupture. The resulting total cross section involved in the in-VV LOCA is then 0.0529 m².

The input parameters used for the 2015 scenario of the in-VV LOCA accident for a water-cooled BB are summarized in Table 4.12.

The results are reported in terms of pressure (Figure 4.30), temperature (Figure 4.31), and mass flow rates (Figure 4.32). The transient in the water case is much slower than that of helium for the same scenario; in fact, the three volumes reach the same pressure at around 500 s, whereas the helium transient lasted around 100 s. The pressure in the PHTS rapidly decreases in the first 1.2 s of transient, as highlighted in Figure 4.30b, until the saturation pressure (~12.05 MPa @ 598 K) is reached; at this point, water starts to vaporize inside the PHTS, sensibly reducing the mass flow rate going from the PHTS to the VV, as it is also evident from Figure 4.32a; as effect of the water flashing, a two-phase mixture goes inside the VV; moreover, during this period of time, the flashing also makes the VV temperature

rapidly drop, as highlighted in Figure 4.31b. Before the saturation point is reached, since water is liquid, the mass flow rate from PHTS to VV is very high, and the pressure increase in the VV is consequently much steeper than during the subsequent phases, when a two-phase mixture is present in the PHTS.

Table 4.12: Value of the parameters used in the EU DEMO WCLL in-LOCA 2015 scenario.

Parameter	***Value***	***Note***
PHTS		
Volume [m³]	300	[62]
Initial pressure [MPa]	15.5	[8]
Initial temperature [K]	598	Outlet value [8]
Break		
Cross section [m²]	0.0529	See discussion above
VV		
Volume [m³]	3000	[63]
Burst disks		
Number	1	Same as ITER VVPSS
Cross section [m²]	1	Same as ITER VVPSS
Opening differential pressure [MPa]	0.15	Same as ITER VVPSS
Bleed valves		
Number	2	Same as ITER VVPSS
Cross section [m²]	0.1	Same as ITER VVPSS
Opening differential pressure [MPa]	0.09	Same as ITER VVPSS
SP		
Volume [m³]	1107	[59]
Initial pressure [kPa]	2.34	[59]
Initial water level [%]	50	[59]

After that, the evolution of the transient is qualitatively similar to the helium one, but with much larger characteristic timescales. The pressure in the VV increases further, although at a limited rate, and the VV temperature starts to increase as well. The BLs open after 1.4 s of transient, see Figure 4.32b, so after the saturation pressure is reached; as with helium, the mass flow rate removed by these lines is too small (~2.5 % of the incoming flow) to effectively reduce the pressure increase in the VV, which continues increasing almost unaffected until ~2.5 s when the BDs break and much more water starts to be discharged to the SP, with a flow

rate ~25 % of the incoming flow. At this point, the mass removal from the RLs is high enough to produce a sensible change in the steepness of the pressure increase, but still not effective as needed, as the pressure in the VV continues to increase up to a peak value of 490 kPa after 30 s. Anyway, it is worth noting that the pressure peak in the VV is smaller than in the helium case, although with a volume need for the suppression system more than 100× smaller.

At the end of the transient, the pressure value in the three volumes is ~124 kPa. The main results of the calculation, in terms of peak and final pressures and temperatures in the three volumes, are reported in Table 4.13.

Figure 4.33 shows the evolution of pressure in the three volumes of the system (left axis) and mass flow rates between the volumes (right axis). The pressure in the VV increases in the first part of the transient until the mass flow rate from the VV to SP reaches and overcomes the mass flow rate from PHTS to VV. After that, the mass flow rate which exits from the VV is higher than the mass flow rate that enters the same volume, and the pressure in the VV decreases until it reaches the pressure in the SP (~300 s). From this point on, the pressure behaviour of the two volumes is the same, while the PHTS pressure continues decreasing as it empties, until it reaches the same pressure value as the other two volumes, thus ending the transient (~500 s).

The evolution of the mass stored within the three volumes is reported in Figure 4.34; the SP mass is plotted as increment with respect to the initial value (~522 t), in order to better highlight the mass conservation and the distribution of the water released from the PHTS. Since almost all the water in the SP is in liquid phase (as reported by Figure 4.36), the vast majority of the water mass released from the PHTS goes into the SP; only during the initial phase, when liquid is being discharged to the VV and flashing, the VV holds a non-negligible fraction of the total coolant inventory; it then stabilizes around a 40 % quality and discharges most of its mass inside the SP, which can accommodate a larger water mass by recondensing the steam.

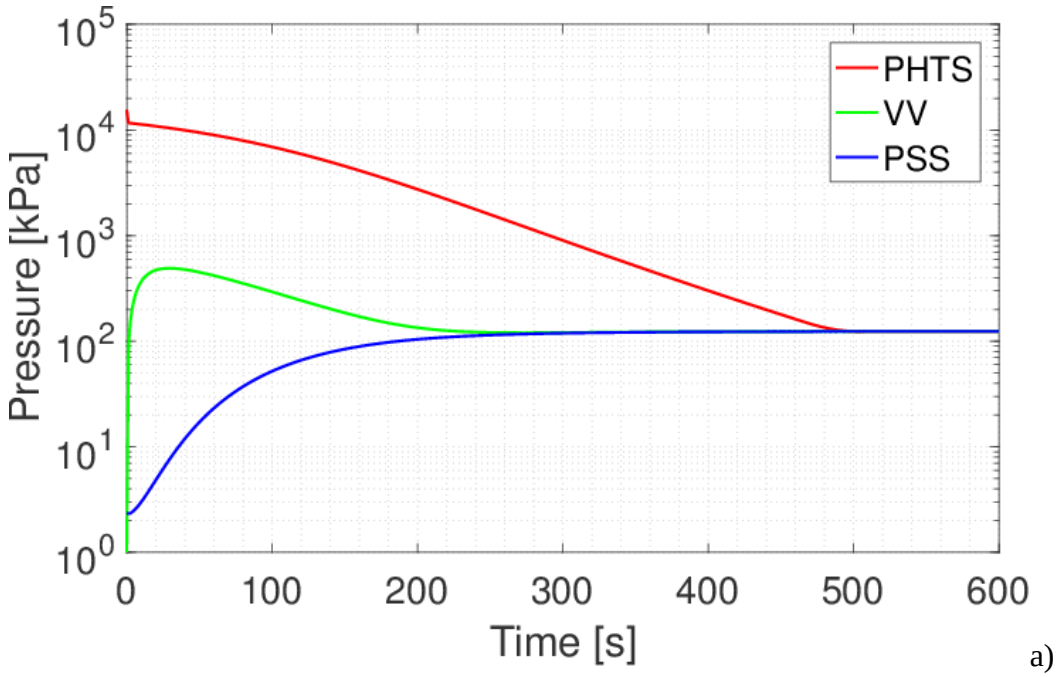

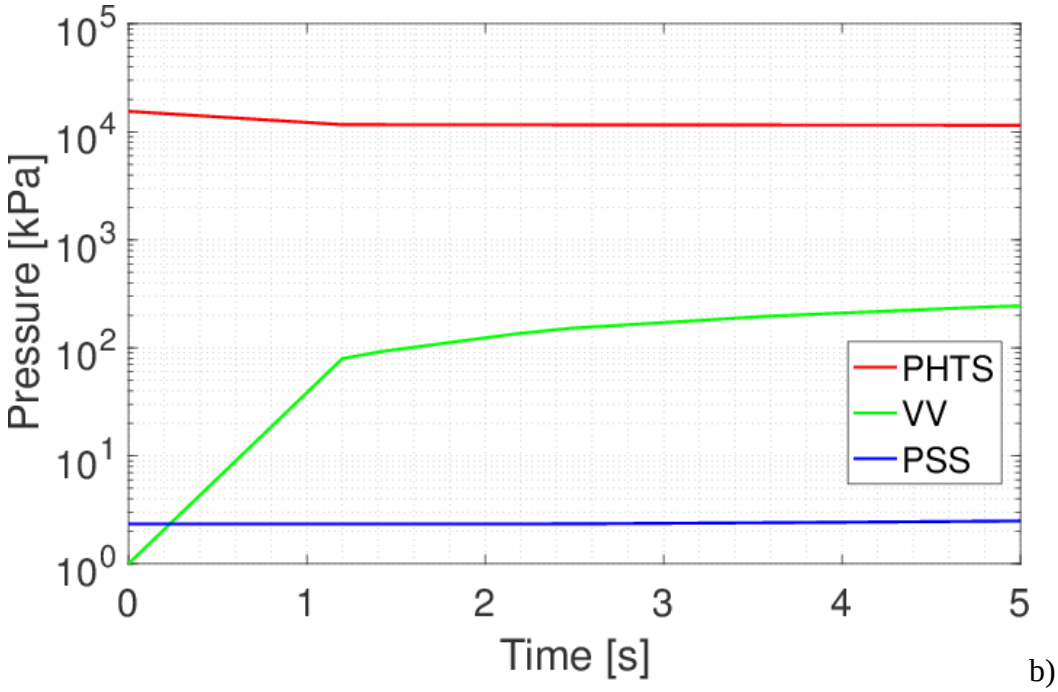

Figure 4.30: a) Computed evolution of the pressure in the three considered volumes, for the WCLL in-VV LOCA 2015 scenario; b) zoom of the pressures during the first 5 s.

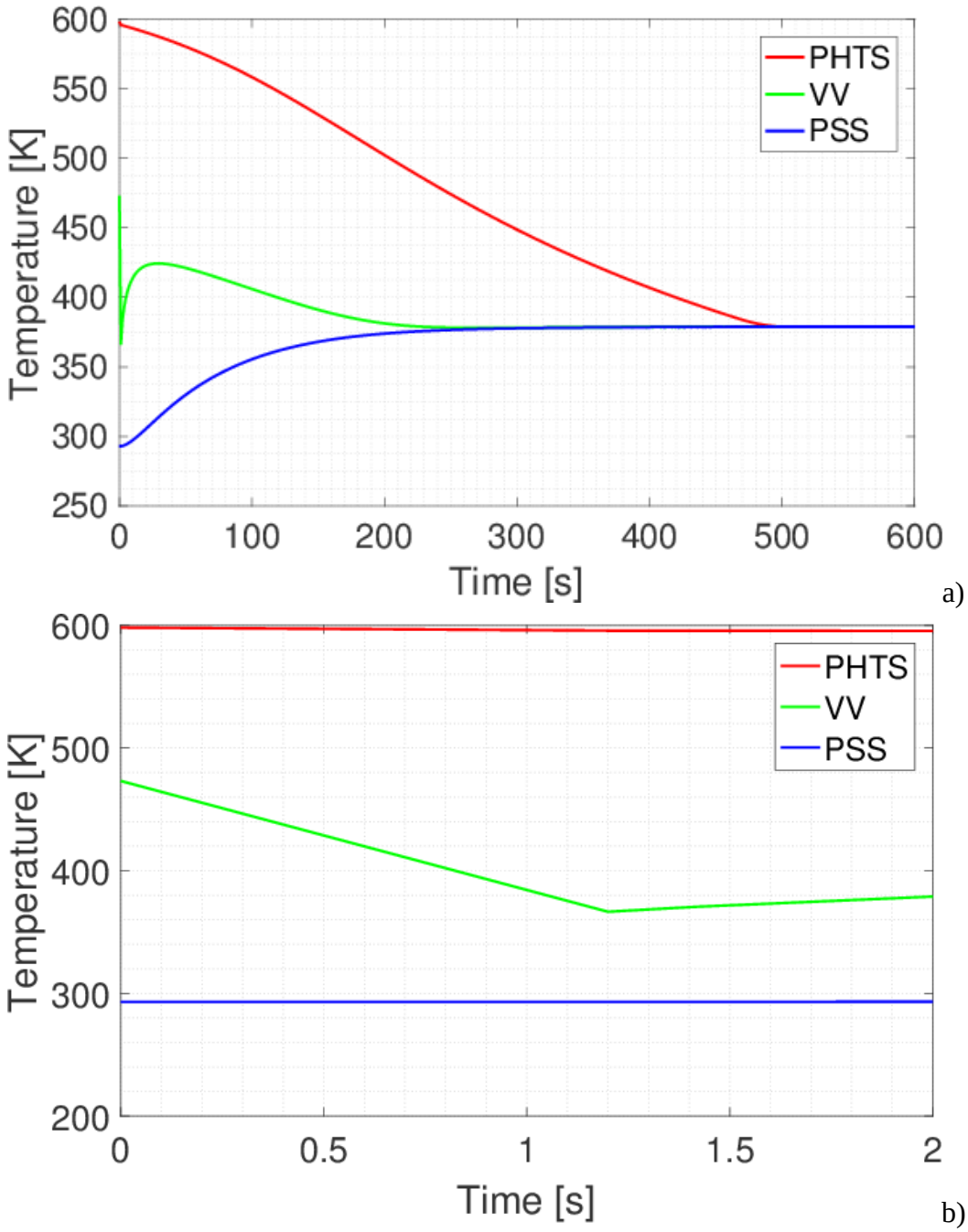

Figure 4.31: a) Computed evolution of the temperature in the three considered volumes, for the WCLL in-VV LOCA 2015 scenario; b) zoom of the temperature during the first 2 s.

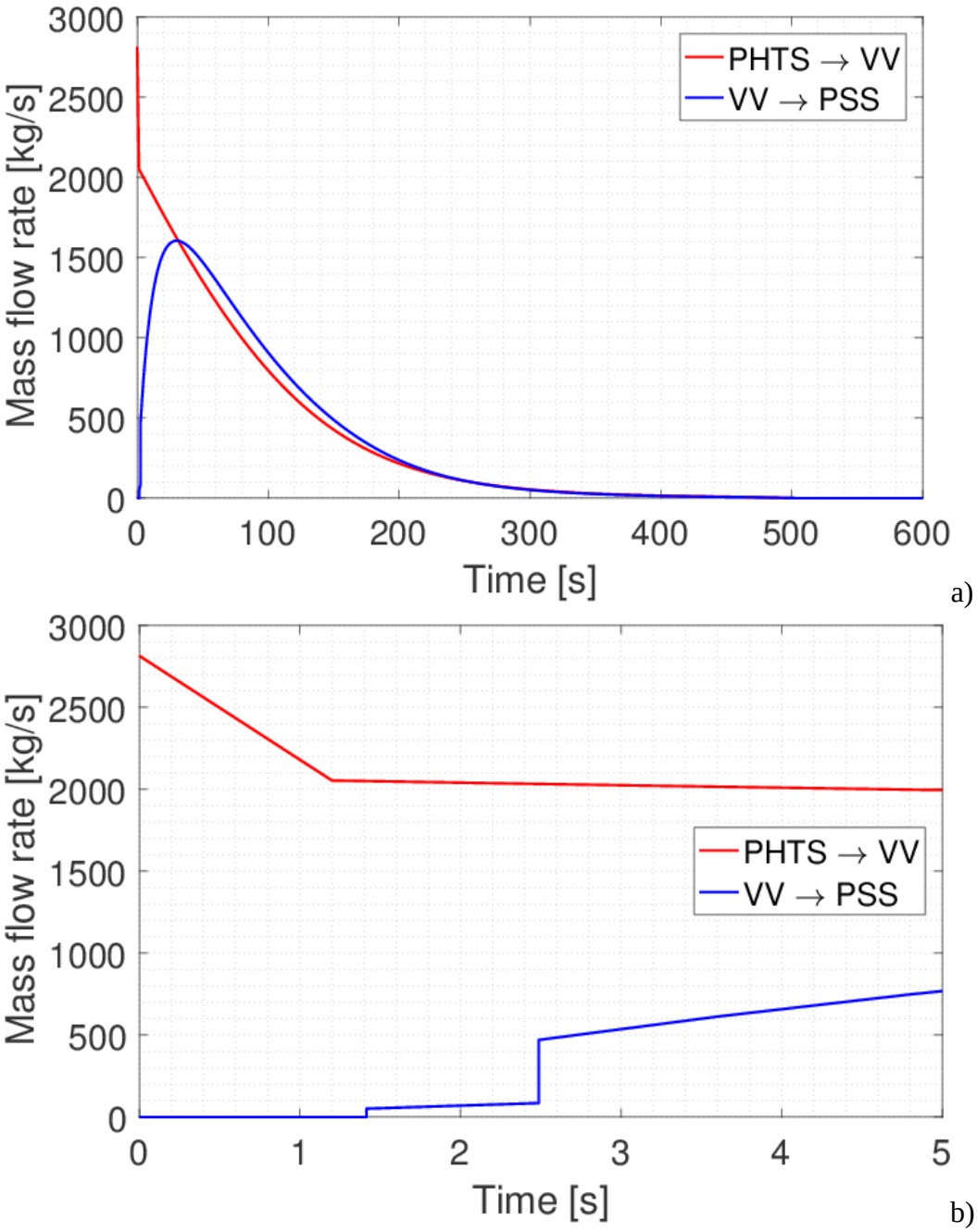

Figure 4.32: a) Computed evolution of the mass flow rate from PHTS to VV and from VV to SP, for the WCLL in-VV LOCA 2015 scenario; b) zoom of the mass flow rates during the first 5 s.

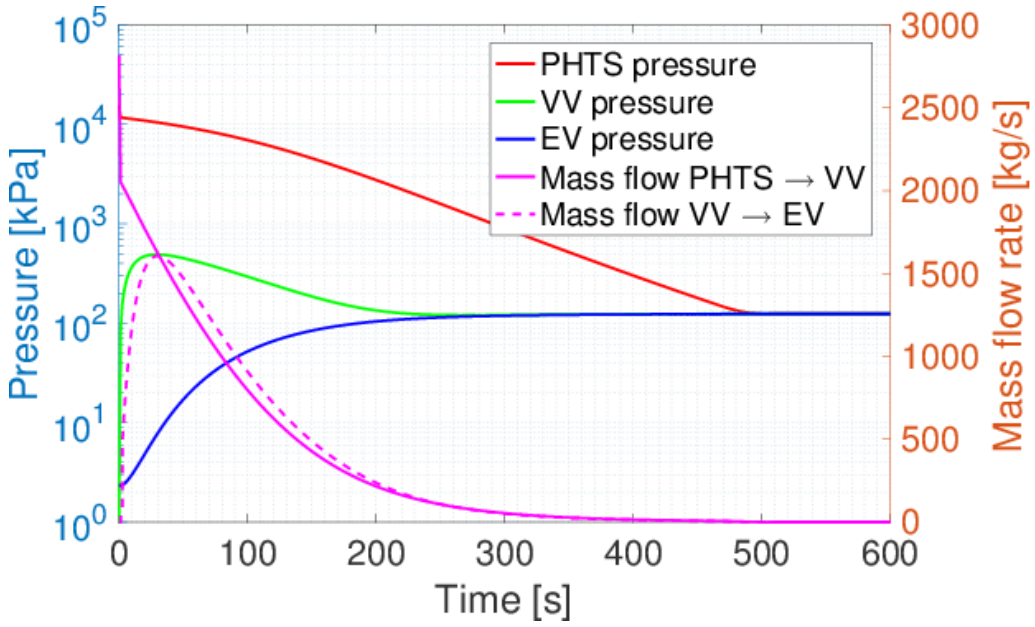

Figure 4.33: Computed evolution of the pressure and mass flow rates in the three considered volumes, for the WCLL in-VV LOCA 2015 scenario.

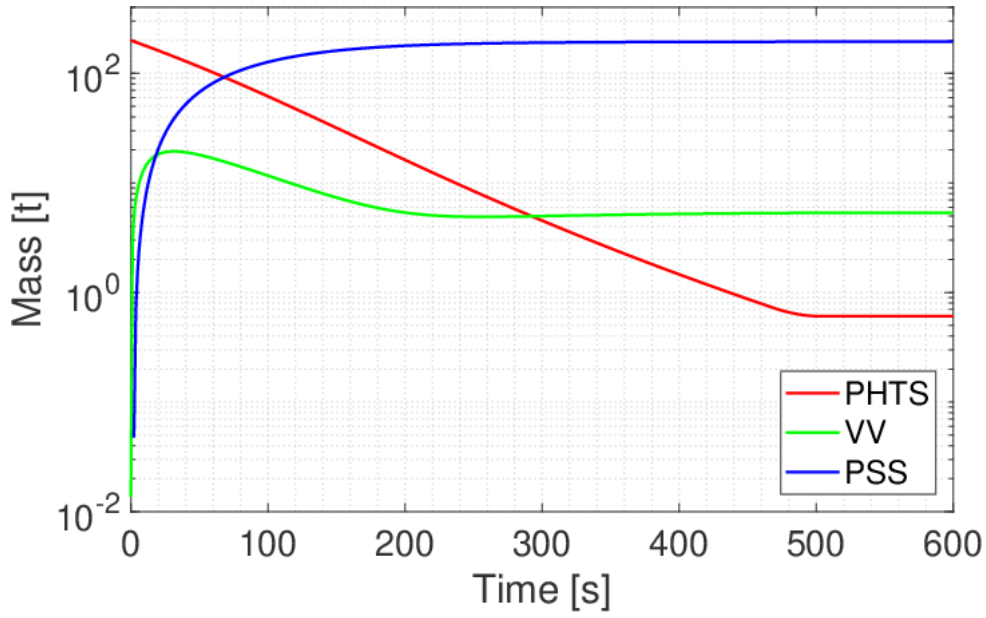

Figure 4.34: Computed evolution of the mass stored in the three considered volumes, for the WCLL in-VV LOCA 2015 scenario. The PSS mass is plotted as relative to the initial value (522 t)

Figure 4.35 reports the evolution of the energy stored in the three volumes. Also in this case, most of the energy is stored inside the SP at steady-state; moreover, the

energy stored in the VV never reaches a sensible value, if compared to the overall energy content of the system.

Finally, Figure 4.37 reports the evolution of the fluid state in the three volumes during the transient in the *T-s* (temperature – specific entropy) plane. The fluid inside the PHTS starts in liquid conditions slightly above the saturation and expands isentropically (as non-equilibrium phenomena are neglected); the water in the VV, initially in vapour conditions, rapidly enters the bell-shaped curve as the pressure increases and liquid forms during the transient, when it stabilizes (as visible also in Figure 4.36). The SP is instead always in saturation conditions, as it is assumed to always contain saturated fluid.

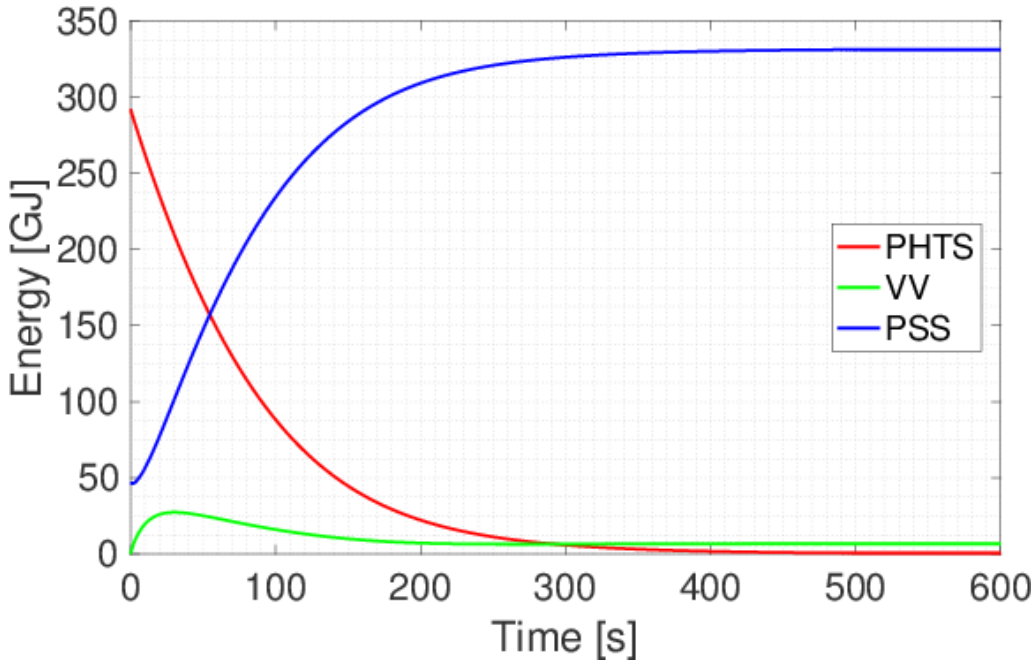

Figure 4.35: Computed evolution of the energy stored in the three considered volumes, for the WCLL in-VV LOCA 2015 scenario.

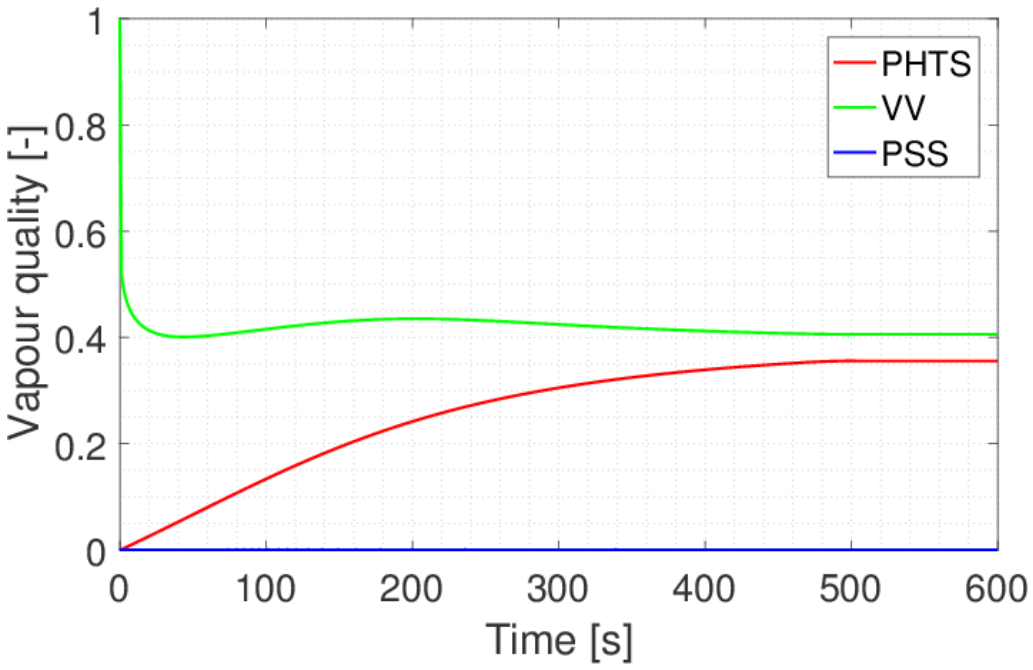

Figure 4.36: Computed evolution of the vapour quality in the three considered volumes, for the WCLL in-VV LOCA 2015 scenario.

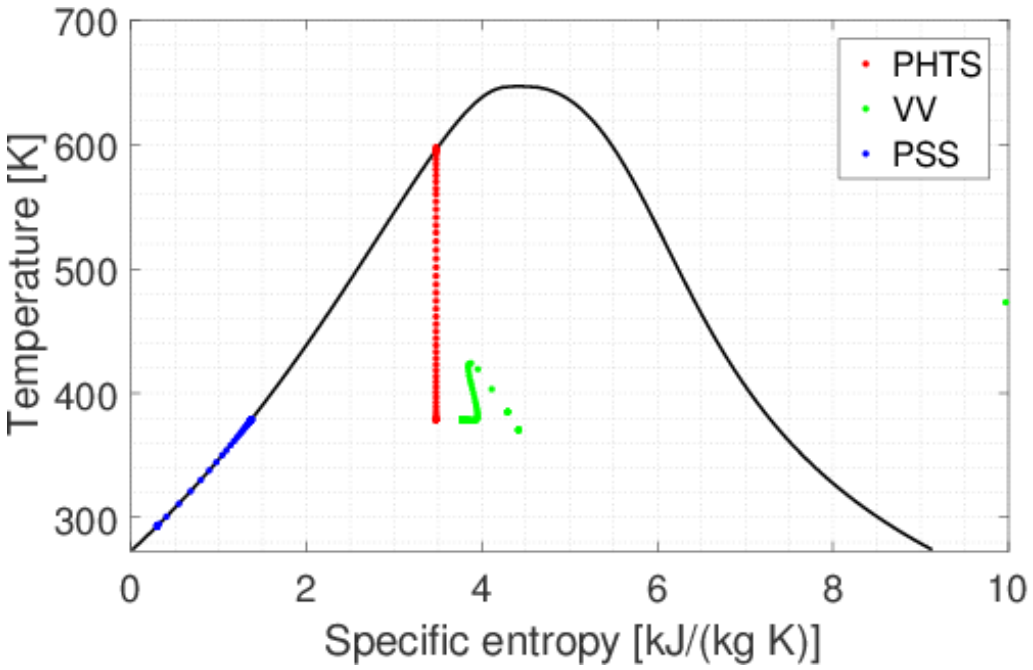

Figure 4.37: Computed evolution of the fluid state in the three volumes in the *T-s* plane, for the WCLL in-VV LOCA 2015 scenario.

Table 4.13: Resume of the main results of the WCLL in-VV LOCA 2015 scenario.

Volume	***Pressure [kPa]***		***Temperature [K]***	
	Peak	*Final*	*Peak*	*Final*
PHTS	15500		598	
VV	491	124	473	379
SP	124		379	

Parametric analysis[22]

As in the case of the HCPB, for the parametric analysis all the parameters have the same value as in the 2015 scenario, with the exception of the values mentioned in the introduction to section 4.3, i.e. break cross section, number of RLs and SP volume (increased from 1107 m³ to 2000 m³); also in this case it is assumed that one BV is available for each BD. Concerning the inventory, instead, since the current WCLL BoP design foresees a single loop for the FW PHTS (see section 1.2.2 above), all the investigated cases have the same inventory, i.e. the total inventory of the FW PHTS (138 m³ [15]). For the same reason, there is no visible distinction among the cases identified with the poloidal or toroidal direction of the energy deposition, so all results are discussed together.

The cases analysed in this parametric study are listed in Table 4.14.

Table 4.14: Cases analysed for the WCLL in-VV LOCA parametric analysis.

Case #	***FW break size [m²]***	***# channels involved***	***Discharging area [m²]***
1	0.01	3	2.940×10^{-4}
2	0.1	27	2.646×10^{-3}
3	1	262	2.568×10^{-2}
4	2	524	5.135×10^{-2}
5#	5	1305	1.279×10^{-1}

The results of this study are reported in Figure 4.38, in terms of time evolution of the VV pressure. The main outcome is nearly identical to the helium parametric analysis, despite all the differences (coolant behaviour, timescales, discharging area and expansion volume): in fact, all FW break sizes >1 m² cause the VV pressure to increase above 200 kPa, whereas with all FW break sizes <1 m² the BD set point is

[22] Part of the work described in this section was also published in [35].

not even reached. Again, case 3, with 1 m² of FW break size is in between, overcoming the pressure limit with 2 RLs only and being safe with 3 or 4 RLs (by 7 kPa only with 3 RLs).

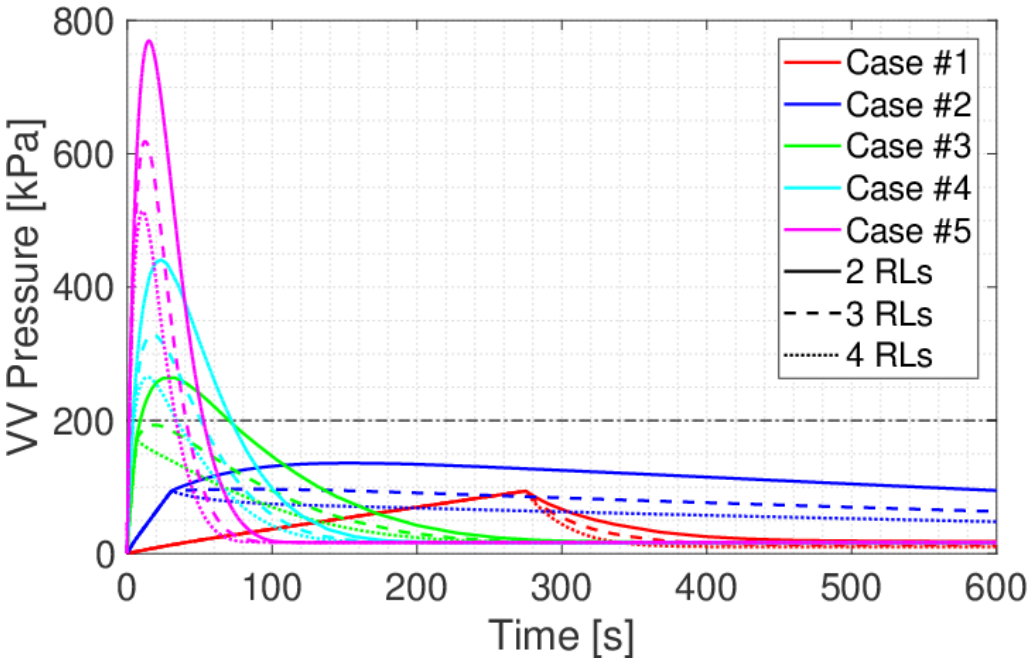

Figure 4.38: Computed evolution of the VV pressure for the WCLL in-VV LOCA parametric analysis. Different colours refer to different cases, whereas different line styles refer to a different number of RLs. The thin, black, dash-dotted line represents the VV pressure limit (2 bar).

As mentioned in section 1.3 above, the use of IVs is being considered for the WCLL cooling system; even if the aim of this solution is mainly to reduce the radioactive inventory released outside the PHTS rather than reducing the pressure peak, cases 3-5 are here simulated again including the IVs, to check if they may also help in mitigating the pressure transient. In fact, recent estimates for the time needed for the IVs to intervene are of 5 s, including the time needed to activate the valves and the time needed by the valves to completely close [38], and such time is in some cases much smaller than the time needed to reach the peak. Among the two alternatives highlighted in [38], here the IVs are assumed to be located downstream the loop collectors, see Figure 4.39, with one IV at the inlet and one at the outlet of each cooling circuit. The volume after the IV is then only the in-VV coolant volume (~32 m³ [15]).

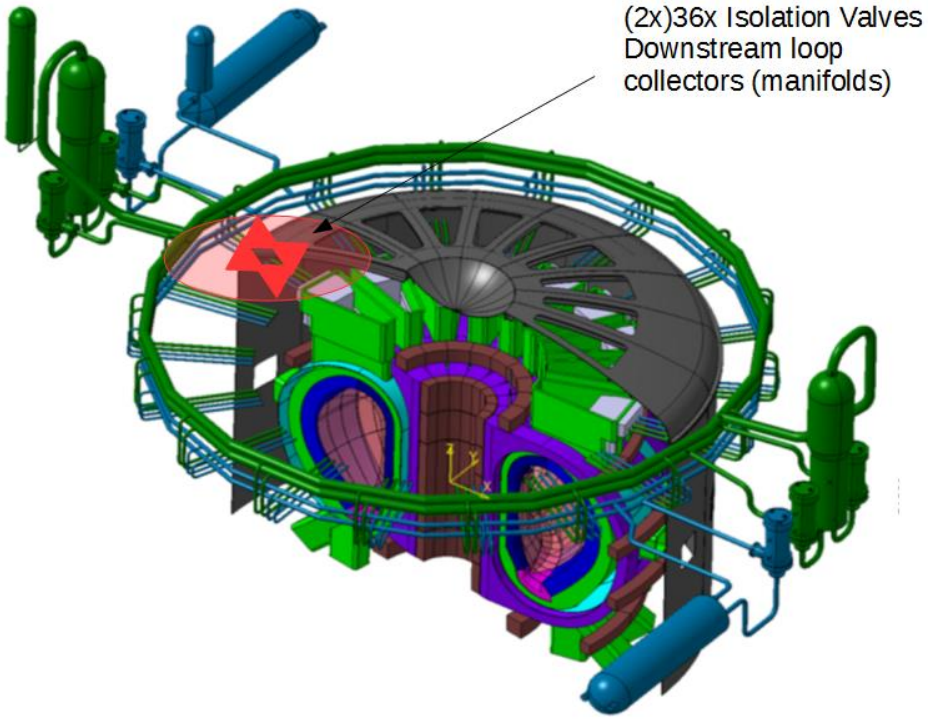

Figure 4.39: Location of the IVs assumed in this work (reproduced from [38]).

The evolution of VV pressure in cases 3-5 including IVs is reported in Figure 4.40. As evident, the main advantage of introducing IVs is that now a FW break of 1 m² (case 3) is withstood by the VVPSS even with 2 RLs only (peak pressure is 4 kPa below the limit), and also that case 4 with 2 m² can be dealt with if 4 RLs are used (even though the margin is even smaller, 2 kPa). In case 5, even if the pressure limit is overcome regardless of the number of RLs, it can be seen how the peak pressure is strongly reduced (more than halved in the worst case with 2 RLs).

As a side remark, it is also proved that IVs are indeed useful to reduce the coolant inventory discharged in the SP: this reduction, in fact, can be as high as ~78 % in the worst case, which is an undoubted advantage from the safety point of view, but also simplifies the design and integration in the plant of the SP itself.

The main results of this study are summarized in Table 4.15, reporting for each case the peak pressure in the VV ($p_{VV,peak}$), together with the time when the peak is reached (t_{peak}), for the three different numbers of RLs available (2/3/4 RLs), including the simulations with IVs.

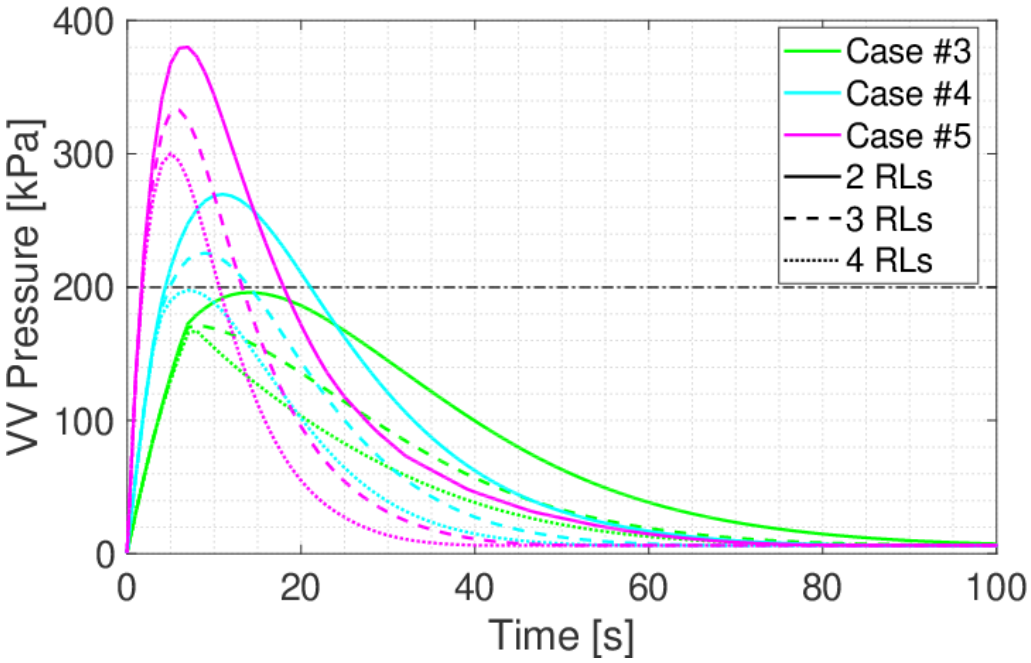

Figure 4.40: Computed evolution of the VV pressure for the WCLL in-VV LOCA parametric analysis, when IVs are implemented downstream the loop collectors. Different colours refer to different cases, whereas different line styles refer to a different number of RLs. The thin, black, dash-dotted line represents the VV pressure limit (2 bar).

Table 4.15: Results of the WCLL parametric in-VV LOCA analysis, with 2/3/4 RLs. Peak values above the limit (200 kPa) are marked with red colour, whereas values below the limit are marked with green colour.

Case #	***FW break size [m²]***	$p_{VV,peak}$ ***[kPa]***	t_{peak} ***[s]***
1	0.01	94/94/94	275/275/275
2	0.1	136/97/94	150/31/31
3 (w/o IV)	1	265/193/171	30/20/7
3 (w/ IV)	1	196/172/172	14/7.5/7.5
4 (w/o IV)	2	441/329/265	24/18/14
4 (w/ IV)	2	270/226/198	11/9/7
5 (w/o IV)	5	770/619/514	15/12.5/10.5
5 (w/ IV)	5	381/334/300	6.5/5.5/5

Chapter 5

Conclusions and perspective

The development of the GETTHEM code has been presented in this work. It is the first system-level dynamic thermal-hydraulic tool developed explicitly for the modelling of the PHTS and BoP of tokamak fusion reactors, with particular emphasis on the EU DEMO reactor, under design within the EU by the EUROfusion Consortium.

The code currently focuses on the modelling of the BB cooling loops, in particular concerning the HCPB and WCLL concepts of BB under investigation within EUROfusion as candidates for the EU DEMO blanket. Two modules have been developed, in order to cope with both normal and accidental transients, respectively. The code aims to be a fast-running tool, enabling parametric analyses in support of the different design teams, by rapidly sweeping the operating range of the machine parameters and providing feedbacks at the global level, e.g. suggesting the areas where improvements are needed. To this aim, some simplifying assumptions have been introduced, by simulating all the components with a 0D/1D approach and linearizing the computation of the fluid thermophysical properties. The Modelica® modelling language has been chosen as development language for this code, for its "implicit" dynamic nature, its user-friendliness, and to easily build a modular code, thanks to the object-oriented modelling paradigm.

The code capabilities have been checked in different scenarios and against different tools: for the nominal operating conditions, the code prediction of the solid temperatures, both average and hot-spot (obtained thanks to a suitable postprocessing procedure), have been benchmarked against a 3D CFD analysis of the

HCPB BB elementary cell. Despite the model simplifications and the coarse discretization (driven by its system-level nature), a very good agreement has been found, with the code prediction within the accuracy of the CFD. Moreover, the code has been found to be more precise in the regions where the solid temperatures are higher, i.e. in the most critical points. In addition, the computed coolant temperature has been also benchmarked against computationally expensive 3D CFD simulations of the WCLL BB elementary cell, showing again acceptable results given the model simplifications and its aim.

The accidental transient module of the code has been checked as well: in the case of the HCPB, the model predictions for an in-VV LOCA have been compared with those obtained with the validated CONSEN code, after an initial calibration phase, showing an excellent agreement on all the variables of interest. For the case of the WCLL, instead, the model was validated against experimental data from the ICE campaign performed in 2000 in Japan. Also in this case the model proved to be very accurate (well within experimental uncertainty) on the checked variables, i.e. pressures and mass flow rate.

After the benchmark and validation phase, GETTHEM has been reliably applied to different EU DEMO-relevant analyses. The first application was devoted to the analysis and optimisation of the coolant mass flow rate distribution in the 2014 version of the HCPB BM: in fact, a mass flow rate unbalance was identified between the CPs and the BM caps, causing the CPs to overheat. The code showed how the cooling performance of the BM might be optimised introducing suitable orifices at the inlet of the caps, reaching thermal equilibrium between caps and CPs while reducing the total mass flow rate and compression power. A comparison has also been done between two cooling concepts, namely HCPB-I and HCPB-S, with the FW integrated or separated from the primary loops, showing how HCPB-I concept may be used (directly integrating FW heat in the power conversion chain) only for the BMs which do not overcome 500 kW/m² of heat flux on the FW.

GETTHEM has then been applied to analyse the hot-spot temperature distribution in the EUROFER of the FW for both HCPB and WCLL, which is a design constraint for the system. It has been shown that in several IB BMs of the HCPB the EUROFER structures overcome the working temperature limit, if some heat transfer promotion is not introduced; also in this case the opportunity to use the HCPB-S concept has been investigated. For the WCLL, instead, the temperature in the EUROFER is below the threshold in the nominal scenario, but may overcome

550 °C if the peak heat flux on the FW is considered. Also, possible boiling has been detected in some regions, calling for further analyses.

The model has finally been applied to analyse accidental scenarios like, e.g., in-VV LOCA relevant for the EU DEMO: as a first scenario, a large toroidal break involving all the BB segments has been postulated, showing that the current VVPSS design is insufficient to mitigate the maximum VV pressure reached in this kind of transient, for both HCPB and WCLL. Then, a parametric analysis has been performed, varying the break size (spanning three orders of magnitude), and also changing the number of RLs available to evacuate the coolant. For both HCPB and WCLL it has been shown that breaks larger than 1 m² require an improvement of the VVPSS design, whereas breaks of 0.1 m² and below do not even require intervention of the BDs. For the WCLL, the use of IVs has also been considered, showing that, although not being determinant, it may allow relaxing some constraints on the VVPSS, e.g. allowing a break size equal to 1 m² to be withstood even with the smallest number of RLs.

In perspective, two different improvements are envisaged: the first is the inclusion of components closer to the electric grid (such as those belonging to the PHTS and PCS), in order to allow studying also the dynamic behaviour of the primary and secondary loops under different conditions and to estimate the global effects of different parameters. The second improvement is to include other in-VV components, such as the divertor and VV cooling systems, and their integration in the PHTS, to eventually build a complete global model of the EU DEMO plant. In addition, some of the simplifying assumptions, introduced to preserve the code's fast-running nature, may be relieved in the future, exploiting the constant improvements of the Modelica® compilers in terms of computational cost, leading to more accurate (but still fast and easily affordable) results.

Finally, also the accidental module of the code should be improved, e.g. by linking it to the 1D PHTS model, to analyse the effect of accidents such as Loss-Of-Coolant or Loss-Of-Flow on the PHTS, and by introducing suitable models for the solid structures. Also in this case, a better modelling of some of the components, such as the SP, should be introduced, relaxing the non-conservative assumptions.

Appendix A

Peak temperature estimation[23]

To estimate the hot-spot temperature from the GETTHEM results, a shape factor f_p^{CFD} is determined by postprocessing the 3D CFD simulations performed by the BB designers, according to equation (34):

$$f_p^{CFD} = \frac{T_{hotspot}^{CFD} - T_{coolant,in}}{T_{ave}^{CFD} - T_{coolant,in}} \tag{34}$$

where $T_{hotspot}^{CFD}$ is the computed hot-spot temperature in the EUROFER computational domain, T_{ave}^{CFD} is the volume-averaged temperature in the EUROFER domain and $T_{coolant,in}$ is the coolant inlet temperature.

The hot-spot temperature $T_{hotspot}^{GETTHEM}$ can be then estimated postprocessing the GETTHEM results according to equation (35):

$$T_{hotspot}^{GETTHEM} = T_{coolant,in} + f_p^{CFD}\left(T_{ave}^{GETTHEM} - T_{coolant,in}\right) \tag{35}$$

where $T_{ave}^{GETTHEM}$ is the temperature computed in the solid FVs by GETTHEM. The procedure is schematized in Figure A.1.

[23] Part of the work described in this section was also published in [11].

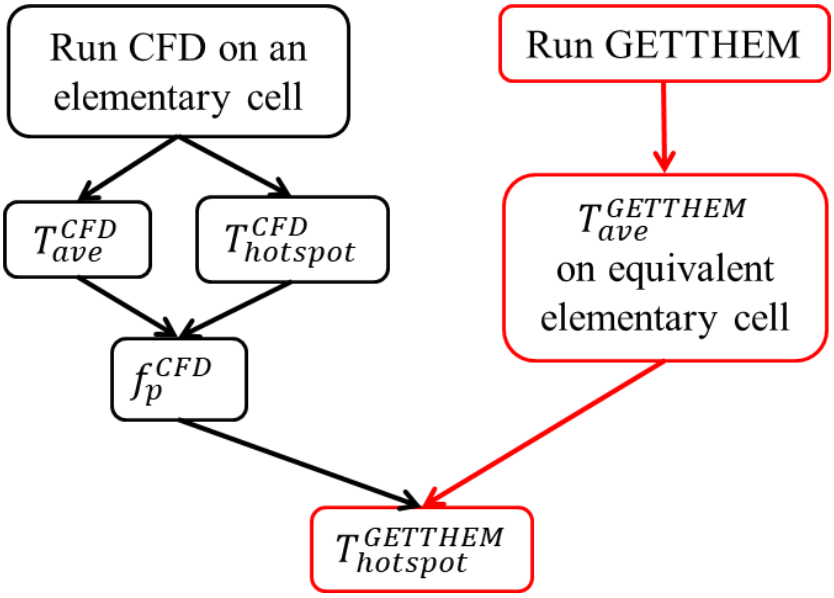

Figure A.1: Flow chart for the estimation of the EUROFER hot-spot temperature (adapted from [13]).

Appendix B

Verification of the 1D fluid model

In order to verify that the equations reported in section 2.2.2 above are correctly solved, the 1D fluid flow model for water is subject to four tests:

1. Verification of the hydraulic properties;
2. Verification of the thermal properties;
3. Verification of the advective properties;
4. Verification of the wall heat capacity.

The results of these tests are reported in the following.

B.1 Hydraulic properties

To verify the hydraulic properties, the model reported in Figure B.1 was used. The pressure source and sinks impose constant pressure values; the parameters for all the channels are reported in Table B.1.

As the total pressure drop, imposed by the ideal pressure source and sinks, is of 0.4 bar, and since channels 41 and 42 are in parallel, all the channels are expected to face a pressure drop of 0.1 bar, leading to a mass flow rate of 1 kg/s in channels 1-3; this mass flow rate should be equally split between channels 41 and 42, as it is a parallel of two identical channels, hence leading to a value of 0.5 kg/s in these channels. This is correctly computed by the model, as reported in Figure B.2 and Figure B.3 for the pressure drop and mass flow rate, respectively.

Table B.1: Parameters of the model used for the verification test 1.

Component	***Parameter***	***Value***
Pressure source	Pressure	155.4 bar
Pressure sinks	Pressure	155 bar
Channels 1-3	Nominal pressure drop	0.1 bar
	Nominal mass flow rate	1 kg/s
	Length	1 m
	Cross section	10^{-3} m²
Channels 41-42	Nominal pressure drop	0.4 bar
	Nominal mass flow rate	1 kg/s
	Length	1 m
	Cross section	10^{-3} m²

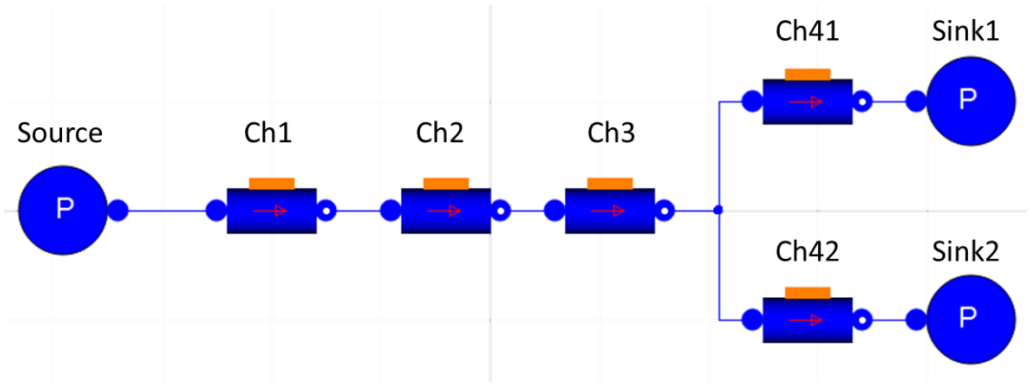

Figure B.1: Model used to verify the hydraulic properties. Ch#: 1D channels; Source: ideal pressure source; Sink#: ideal pressure sinks.

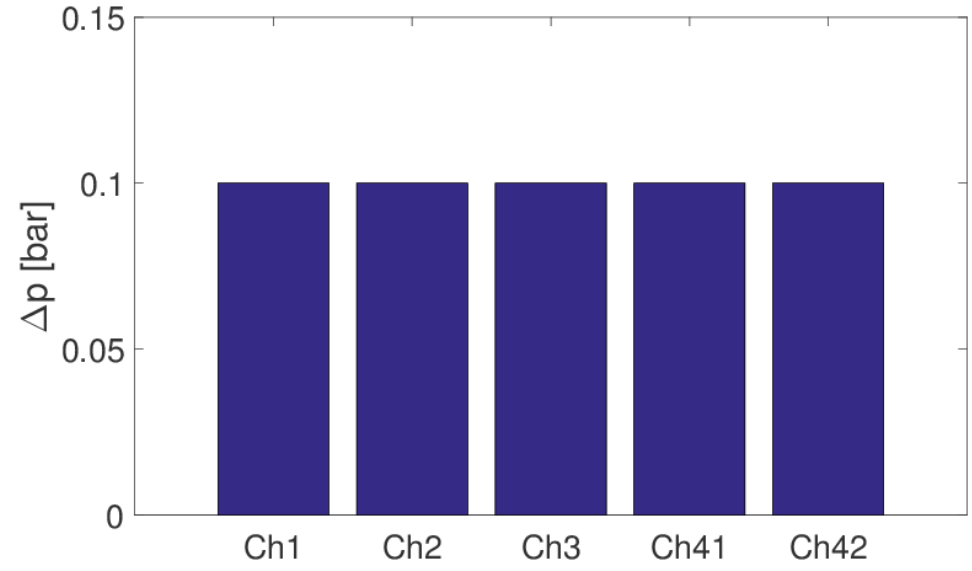

Figure B.2: Steady-state distribution of the pressure drop in the model used for the verification test 1.

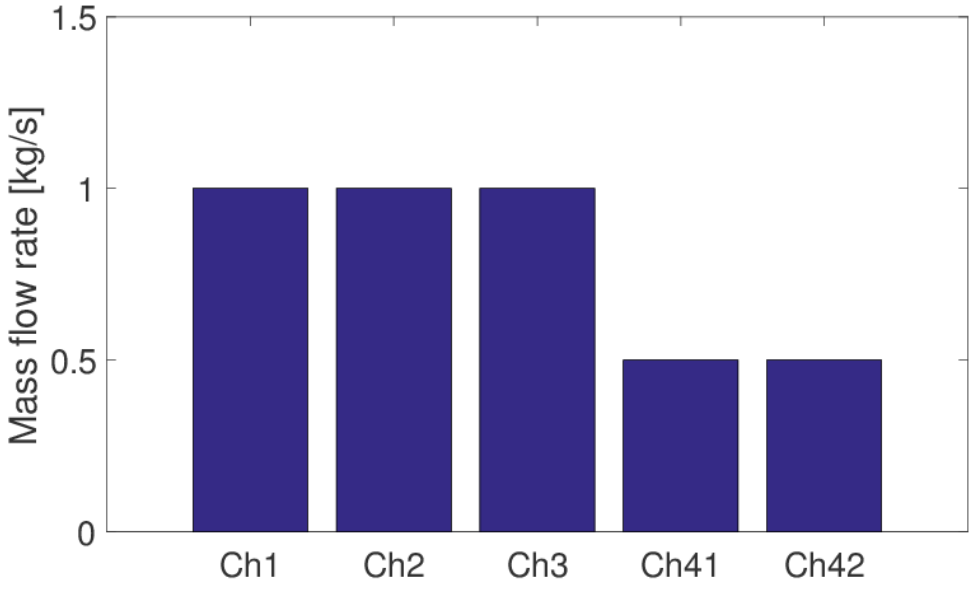

Figure B.3: Steady-state disitribution of the mass flow rate in the model used for the verification test 1.

B.2 Thermal properties

For the verification of the thermal properties, a single 1D channel is loaded by a heat load of $\dot{Q} = 5153$ W, uniformly distributed. The parameters used in this model are reported in Table B.2.

Table B.2: Parameters of the model used for the verification test 2.

Component	***Parameter***	***Value***
Pressure source	Pressure	155 bar
	Temperature	285 C
Pressure sinks	Pressure	154 bar
Channel	Nominal pressure drop	1 bar
	Nominal mass flow rate	1 kg/s
	Length	1 m
	Cross section	10^{-3} m²
	Number of FVs	20

Since the heat capacity of water @ 155 bar and 285 °C is $c_p = 5153$ J/(kg K), from the steady-state power balance $\dot{Q} = \dot{m} c_p \Delta T$ a temperature increase of 1 K is expected, uniformly distributed on the FVs. This behaviour is correctly reproduced by the model, as shown by Figure B.4.

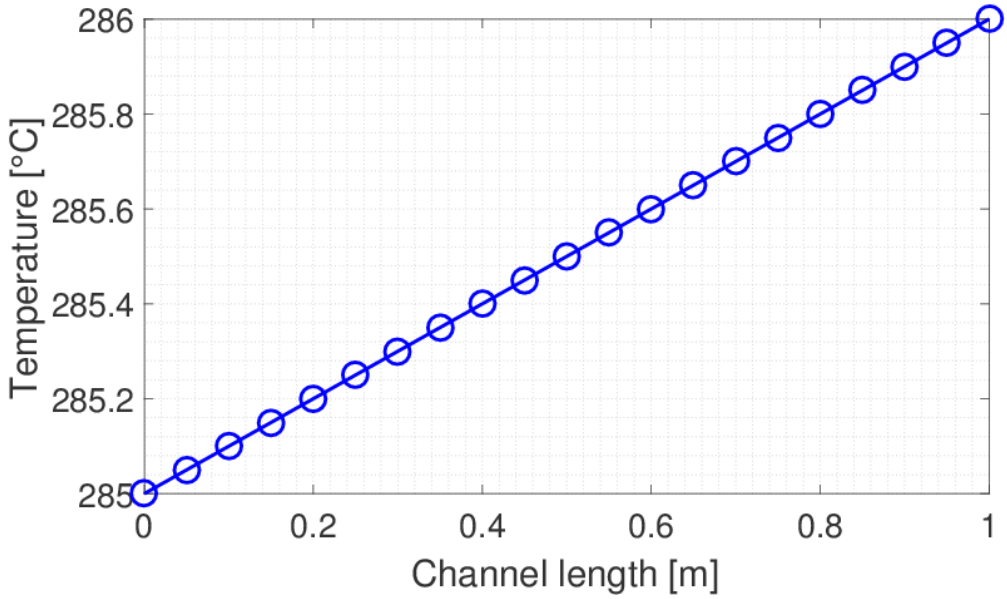

Figure B.4: Steady-state temperature distribution along channel length, for the verification test 2.

B.3 Advective properties

In order to verify the advective properties, a single channel, with no heat load, is connected to an ideal pressure source and to an ideal pressure sink; the water in the channel is initially at a uniform temperature of 285 °C. From $t = 0$ s to $t = 1$ s, the inlet temperature is fixed to 285 °C; after $t = 1$ s, the inlet temperature increases instantaneously to 286 °C. The parameters used in this model are reported in Table B.3.

Table B.3: Parameters of the model used for the verification test 3.

Component	***Parameter***	***Value***
Pressure source	Pressure	155 bar
Pressure sink	Pressure	154 bar
Channel	Nominal pressure drop	1 bar
	Nominal mass flow rate	0.7554 kg/s
	Length	1 m
	Cross section	10^{-3} m²
	Number of FVs	2000

Since no load is given to the channel, the temperature distribution of the water inside it should follow the standard 1D pure advection equation $\frac{\partial T}{\partial t} + v\frac{\partial T}{\partial x} = 0$, where v is the fluid speed. As the water density at 155 bar and 285 °C is $\rho = 755.4\ \mathrm{kg/m^3}$, from $\dot{m} = \rho c A$ a speed of 1 m/s is obtained. Therefore, the temperature step wave at the inlet should travel the channel length within 1 s (*i.e.*, the outlet temperature should become 286 °C at $t = 2$ s). This is correctly reproduced by the model, as reported by Figure B.5, with a small error due to the numerical diffusion deriving from the use of an upwind numerical scheme.

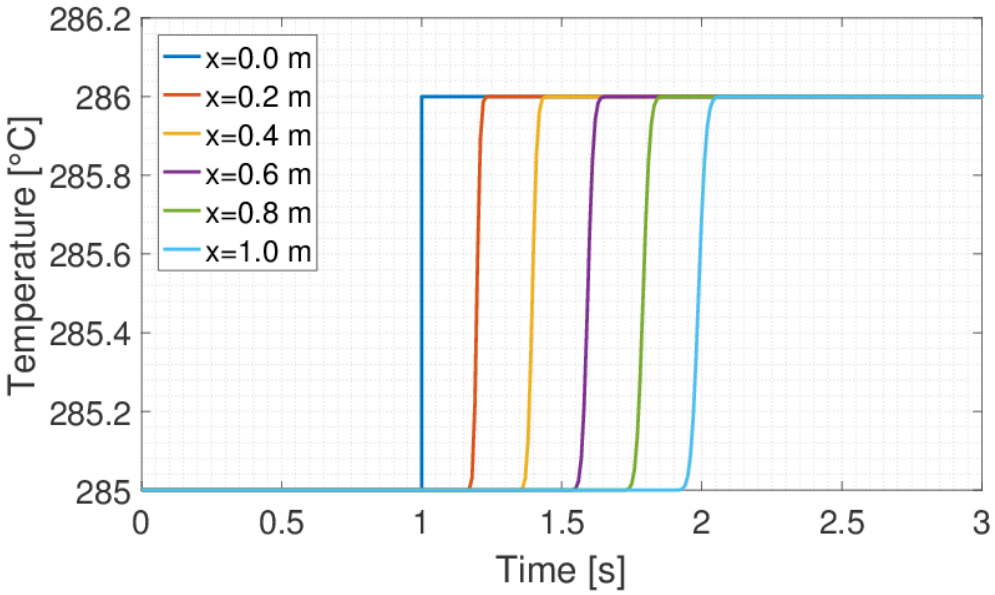

Figure B.5: Temeprature evolution at selected positions for verification test 3.

B.4 Wall heat capacity

Finally, to test the wall heat capacity, the same setup of the previous case was used, but adding a metal wall with heat capacity $C_m = \rho_m A_m l c_m = 100\ \mathrm{J/K}$; the wall-water heat transfer coefficient is set to $\mathrm{HTC} = 1000\ \mathrm{W/(m\ K)}$, while the wet perimeter, starting from the cross section of $10^{-3}\mathrm{m}^2$ mentioned previously, is $\Omega = \sqrt{4\pi A} \cong 0.112$ m.

Substituting equation (8) into equation (7), with $\dot{Q}_{in,i} = 0$, the differential equation for the temperature of the solid volume *i* becomes

$$C_m \frac{dT_{m,i}}{dt} = -\left(T_{m,i} - T_i\right)\Omega l \mathrm{HTC}.$$

Solving this equation for $T_{m,i}$, with initial condition $T_{m,i}(t = 1) = 285$ °C and for constant T_i (as it is the case for volume 1), gives the solution

$$T_{m,i} = T_i - e^{-\frac{\Omega l \mathrm{HTC}}{C_m}(t-1)}.$$

This evolution is correctly reproduced by the model, as reported in Figure B.6 for solid volume 1.

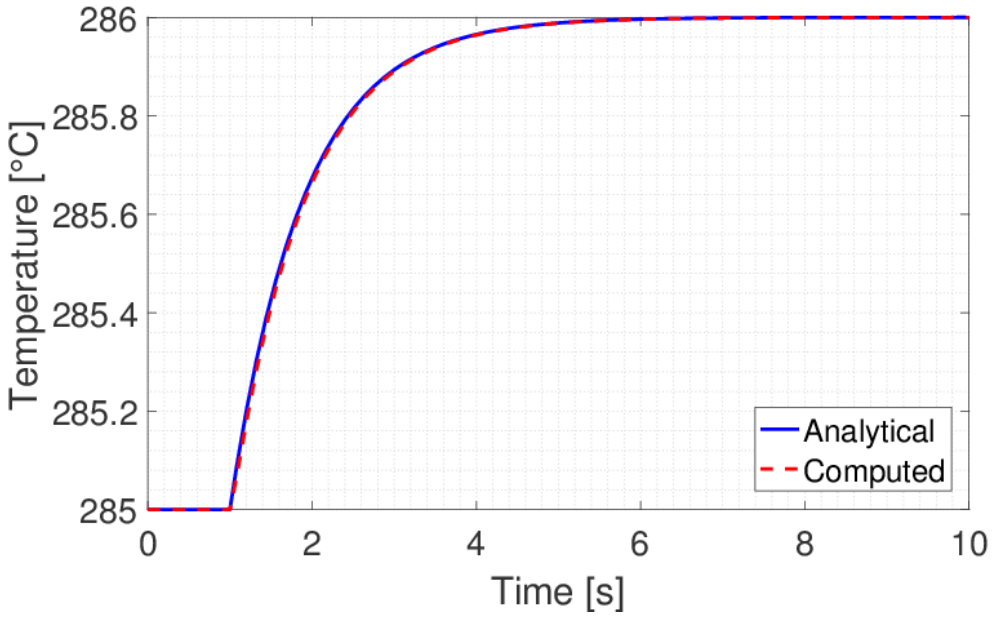

Figure B.6: Evolution of the temperature in the solid volume 1 for verification test 4 (solid line: analytical formula; dashed line: model output).

References

[1] EUROfusion Consortium, “European Consortium for the Development of Fusion Energy,” [Online]. Available: https://www.euro-fusion.org/. [Accessed 28 November 2017].

[2] F. Romanelli, P. Barabaschi, D. Borba, G. Federici, L. Horton, R. Neu, D. Stork and H. Zohm, “Fusion Electricity – A roadmap to the realisation of fusion energy,” European Fusion Development Agreement (EFDA), 2012, ISBN 978-3-00-040720-8T. [Online]. Available: https://www.euro-fusion.org/wpcms/wp-content/uploads/2013/01/JG12.356-web.pdf.

[3] R. Wenninger and G. Federici, “DEMO1 Reference Design - 2015 April ("EU DEMO1 2015"),” EFDA_D_2LBJRY, 2015.

[4] H. Hurzlmeier and B. Meszaros, “EU DEMO1 2015 - DEMO_TOKAMAK_COMPLEX,” EFDA_D_2M9AJJ, 2015.

[5] A. Tarallo, G. Di Gironimo, M. Chantant, I. Moscato and L. Barucca, “Pre-conceptual 3D CAD implementation of PHTS, ESS and PCS design for helium-cooled blanket concept,” EFDA_D_2MZDRS, 2016.

[6] L. V. Boccaccini, G. Aiello, J. Aubert, C. Bachmann, T. Barrett, A. Del Nevo, D. Demange, L. Forest, F. A. Hernández González, P. Norajitra, G. Porempovic, D. Rapisarda, P. Sardain, M. Utili and L. Vala, “Objectives and status of EUROfusion DEMO blanket studies,” *Fusion Engineering and Design,* Vols. 109-111 (Part B), pp. 1199-1206, 2016.

[7] F. A. Hernández González, P. Pereslavtev, Q. Kang, P. Norajitra, B. Kiss, G. Nádasi and O. Bitz, “A new HCPB breeding blanket for the EU DEMO: Evolution, rationale and preliminary performances,” *Fusion Engineering and Design,* no. 124, pp. 882-886, 2017.

[8] E. Martelli, A. Del Nevo, P. Arena, G. Bongiovì, G. Caruso, P. A. Di Maio, M. Eboli, G. Mariano, R. Marinari, F. Moro, R. Mozzillo, F. Giannetti, G. Di Gironimo, A. Tarallo, A. Tassone and R. Villari, “Advancements in DEMO WCLL breeding blanket design and integration,” *International Journal of Energy Research,* p. http://dx.doi.org/10.1002/er.3750, 2017.

[9] G. Aiello, J. Aubert, N. Jonquéres, A. Li Puma, A. Morin and G. Rampal, "Development of the Helium Cooled Lithium Lead blanket for DEMO," *Fusion Engineering and Design,* vol. 89, no. 7-8, pp. 1444-1450, 2014.

[10] D. Rapisarda, I. Fernandez, I. Palermo, M. Gonzalez, C. Moreno, A. Ibarra and E. Mas de les Valls, "Conceptual Design of the EU-DEMO Dual Coolant Lithium Lead Equatorial Module," *IEEE Transactions on Plasma Science,* vol. 44, no. 9, pp. 1603-1612, 2016.

[11] M. Chantant, W. Hering, E. Bubelis, A. Tarallo, I. Moscato and L. Barucca, "HCPB BB PHTS DDD 2016," EFDA_D_2MF5FV v2.3, 2017.

[12] F. A. Hernández González, Q. Kang, B. Kiss, H. Neuberger, P. Norajitra, G. Nadási, P. Pereslavtsev and C. Zeile, "DDD 2015 for HCPB," EFDA_D_2MRQ4E, 2016.

[13] A. Froio, F. Cismondi, L. Savoldi and R. Zanino, "Thermal-hydraulic analysis of the EU DEMO Helium-Cooled Pebble Bed Breeding Blanket using the GETTHEM code," *IEEE Transactions on Plasma Science,* Vols. SOFE-27 special issue, no. in press, 2017.

[14] E. Martelli, A. Del Nevo, P. Arena, G. Bongiovì, G. Caruso, G. Di Gironimo, P. A. Di Maio, M. Eboli, N. Forgione, F. Giannetti, G. Mariano, F. Moro, R. Mozzillo, A. Tassone, R. Villari, S. Paci and D. Giulietti, "WCLL Design Report 2016," EFDA_D_2MTZP6 v1.1, 2017.

[15] E. Martelli, A. Del Nevo, F. Giannetti and M. Polidori, "DEMO BoP - WCLL BB PHTS and PCS preliminary design," EFDA_D_2MH7KC, 2017.

[16] Modelica Association, "Modelica and the Modelica Association," 2017. [Online]. Available: https://www.modelica.org/. [Accessed 12 December 2017].

[17] Modelica Association, "Modelica® - A Unified Object-Oriented Language for Systems Modeling - Language Specification Version 3.4," 10 April 2017. [Online]. Available: https://www.modelica.org/documents/ModelicaSpec34.pdf. [Accessed 12 December 2017].

[18] P. Fritzson, Principles of object-oriented modeling and simulation with Modelica 2.2, Wiley, 2003.

[19] S. Mattsson, H. Elmqvist and M. Otter, "Physical systems modeling with Modelica," *Control Engineering Practice,* vol. 6, pp. 501-510, 1998.

[20] F. Casella, A. Bartolini, S. Pasquini and L. Bonuglia, "Object-Oriented Modelling and Simulation of Large-Scale Electrical Power Systems using

Modelica: a First Feasibility Study," in *IECON 2016 - 42nd Annual Conference of the IEEE Industrial Electronics Society, pp. 6298-6304*, Firenze, 2016.

[21] R. Bonifetto, F. Casella, L. Savoldi Richard e R. Zanino, «Dynamic modeling of a supercritical helium closed loop with the 4C code,» *AIP Conference Proceedings 1434*, pp. 1743-1750, 2012.

[22] L. Savoldi Richard, F. Casella, B. Fiori and R. Zanino, "The 4C Code for the Cryogenic Circuit Conductor and Coil modeling in ITER," *Cryogenics*, vol. 50, pp. 167-176, 2010.

[23] A. Froio, R. Bonifetto, S. Carli, A. Quartararo, L. Savoldi and R. Zanino, "Design and optimization of Artificial Neural Networks for the modelling of superconducting magnets operation in tokamak fusion reactors," *Journal of Computational Physics*, vol. 321, pp. 476-491, 2016.

[24] Dassault Systèmes®, "Dymola," 2017. [Online]. Available: https://www.3ds.com/products-services/catia/products/dymola/. [Accessed 12 December 2017].

[25] The Open Source Modelica Consortium, "OpenModelica," 2017. [Online]. Available: https://www.openmodelica.org/. [Accessed 12 December 2017].

[26] F. Casella and A. Leva, "Modelica open library for power plant simulation: design and experimental validation," *Proceedings of 3rd International Modelica Conference*, pp. 41-50, Linköping, Sweden, 3-4 November 2003.

[27] F. Casella and A. Leva, "Modelling of thermo-hydraulic power generation processes using Modelica," *Mathematical and Computer Modelling of Dynamical Systems*, vol. 12, no. 1, pp. 19-33, 2006.

[28] The International Association for the Properties of Water and Steam, "Revised Release on the IAPWS Industrial Formulation 1997 for the Thermodynamic Properties of Water and Steam," 2007. [Online]. Available: http://www.iapws.org/relguide/IF97-Rev.pdf. [Accessed 07 December 2016].

[29] L. V. Boccaccini, L. Giancarli, G. Janeschitz, S. Hermsmeyer, Y. Poitevin, A. Cardella and E. Diegele, "Materials and design of the European DEMO blankets," *Journal of Nuclear Materials*, Vols. 329-333, part A, pp. 148-155, 2004.

[30] A. Froio, C. Bachmann, F. Cismondi, L. Savoldi and R. Zanino, "Dynamic thermal-hydraulic modelling of the EU DEMO HCPB breeding blanket cooling loops," *Progress in Nuclear Energy*, vol. 93, pp. 116-132, 2016.

[31] A. Froio, F. Casella, F. Cismondi, A. Del Nevo, L. Savoldi and R. Zanino, "Dynamic thermal-hydraulic modelling of the EU DEMO WCLL breeding blanket cooling loops," *Fusion Engineering and Design,* vol. 124, pp. 887-891, 2017.

[32] A. Bertinetti, A. Froio, B.-E. Ghidersa, F. A. Hernández González, L. Savoldi and R. Zanino, "Thermal-hydraulic Modeling of a Segment of the EU DEMO HCPB Breeding Blanket Back Supporting Structure," presented at 13th International Symposium on Fusion Nuclear Technology (ISFNT-13), Kyoto, Japan, 25-30 September 2017.

[33] M. T. Porfiri, *Personal communication,* February 01, 2017.

[34] ANSI/ISA, "Flow Equations for Sizing Control Valves," 2007. [Online]. Available: https://www.isa.org/pdfs/microsites121/isa-750101-spbd/. [Accessed 08 January 2017].

[35] A. Froio, A. Bertinetti, L. Savoldi, R. Zanino, S. Ciattaglia and F. Cismondi, "Benchmark of the GETTHEM Vacuum Vessel Pressure Suppression System (VVPSS) model for a helium-cooled EU DEMO blanket," in *Safety and Reliability - Theory and Applications, Proceedings of the 27th European Safety and Reliability Conference*, Portorož, Slovenia, 2017.

[36] A. Froio, A. Bertinetti, S. Ciattaglia, F. Cismondi, L. Savoldi and R. Zanino, "Modelling an In-Vessel Loss of Coolant Accident in the EU DEMO WCLL Breeding Blanket with the GETTHEM Code," *submitted to Fusion Engineering and Design (ISFNT13 special issue),* 2017.

[37] A. Bertinetti, A. Froio, L. Savoldi and R. Zanino, "Analysis of VVPSS for Helium and Water cooled Breeding Blankets," EFDA_D_2MQDJG v1.1, 2017.

[38] M. Caramello, G. Sanguinetti and P. Zanaboni, "Industry Task: RELAP5-3D Thermal-hydraulic investigation of WCLL BB FW-PHTS LOCA," EFDA_D_2MST4C v2.0, 2017.

[39] G. Caruso, "Preliminary design of the expansion system for a DEMO reactor based on a helium-cooled blanket," DIAEE-NU(16)-0802 – Rome (Italy), 2016.

[40] G. Mazzini, "Preliminary analyses of the Vacuum Vessel Pressure Suppression System using MELCOR 1.8.6," EFDA_D_2L7JLV v1.2, 2017.

[41] B. Kiss, "Thermo-hydraulic analysis support - Activities in 2016," EFDA_D_2MXRHT, 2017.

[42] F. A. Hernández González, Q. Kang, B. Kiss, P. Norajitra, G. Nádasi, P. Pereslavtev and C. Zeile, "HCPB Design Report 2015," EFDA_D_2MNBH9, 2016.

[43] A. Del Nevo, E. Martelli, P. Agostini, P. Arena, G. Bongiovì, G. Caruso, G. Di Gironimo, P. A. Di Maio, M. Eboli, R. Giammusso, F. Giannetti, A. Giovinazzi, G. Mariano, F. Moro, R. Mozzillo, A. Tassone, D. Rozzia, A. Tarallo, M. Tarantino, M. Utili and R. Villari, "WCLL breeding blanket design and integration for DEMO 2015: status and perspectives," *Fusion Engineering and Design,* vol. 124, pp. 682-686, 2017.

[44] A. Del Nevo, E. Martelli and M. Oron-Carl, "Design Description Document 2015 for WCLL (update of DDD 2014)," EFDA_D_2MU9XC, 2016.

[45] E. Martelli, A. Del Nevo, P. Arena, G. Bongiovì, G. Caruso, G. Di Gironimo, P. A. Di Maio, I. Di Piazza, N. Forgione, R. Forte, M. Frullini, R. Giammusso, F. Giannetti, A. Giovinazzi, D. Giulietti, G. Mariano, R. Mozzillo, A. Naviglio, S. Paci, M. L. Richiusa, A. Tassone and R. Villari, "WCLL Design Report 2015," EFDA_D_2N6WLQ v1.0, 2016.

[46] M. T. Porfiri and P. Meloni, "ISAS validation against ICE Experimental campaign 2000 - Pre-test calculations," ENEA FUS TN SIC TR 09/2000, 2000.

[47] K. Takase, *Upgraded ICE Spec,* Personal communication from M. T. Porfiri.

[48] G. Caruso and T. Pinna, "CONSEN validation against ICE experimental campaing 2000 - Post-test calculations," ENEA FUS TN SA-SE-R-012, 2000.

[49] F. A. Hernández Gonzalez, "Thermo-hydraulic layout of the HCPB segment," 1st BB Design Progress Review Meeting, Garching, June 23, 2015.

[50] P. Norajitra, M. Oron-Carl, O. Bitz, V. Chakin, D. Demange, M. Genzalez, F. Hernandez, T. Hernandez, U. Fischer, Q. Kang, B. Kiss, R. Knitter, H. Neuberger, P. Pereslavtsev, G. Porempovics and P. Vladimirov, "DDD 2014 for HCPB," 2MCQCX v1.1, 2015.

[51] B. Meszaros, "EU DEMO1 2015 plasma and equilibrium description," EFDA_D_2LJFN7, 2015.

[52] G. Zhou, F. A. Hernández González, L. V. Boccaccini, H. Chen and M. Ye, "Preliminary steady-state and transient thermal analysis of the new HCPB blanket for EU DEMO reactor," *International Journal of Hydrogen Energy,* vol. 41, no. 17, pp. 7047-7052, 2016.

[53] S. Ruck and F. Arbeiter, “Thermohydraulics of rib-roughened helium gas running cooling channels for First Wall applications,” *Fusion Engineering and Design,* Vols. 109-111, no. A, pp. 1035-1040, 2016.

[54] F. A. Hernández González, P. Pereslavtev, C. Zeile, G. Zhou, I. Maione, O. Bitz, B. Kiss and G. Nádasi, *HCPB Breeding Blanket design and improvements for 2017,* Brasimone, Italy: presented at DEMO BB Design and Analysis Methods Meeting, 2017.

[55] F. Maviglia, “DEMO PFC Heat Load Specifications,” EFDA_D_2NFPNU v0.3, 2017.

[56] M. Kovari, F. Maviglia and T. R. Barrett, “DEMO 2016 - First Wall,” EFDA_D_2MWN32 v1.0, 2016.

[57] F. Maviglia, “Thermo-hydraulic analysis with the RACLETTE code of the maximum first wall breaks size for an unmitigated DEMO disruption,” v 0.1 (draft), Personal communication from F. Cismondi, 2016.

[58] S. Ciattaglia, *Personal communication,* June 29, 2016.

[59] G. Caruso and F. Giannetti, “Sizing of the Vacuum Vessel Pressure Suppression System of a Fusion Reactor Based on a Water-Cooled Blanket, for the Purpose of the Preconceptual Design,” *Science and Technology of Nuclear Installations,* vol. 2016, no. 8719695, p. 11.

[60] C. Gliss, *Personal communication,* March 23, 2017.

[61] T. Franke, *Personal communication,* March 23, 2017.

[62] I. Moscato and F. Cismondi, “Input data by BB - BOP for SAE - VVPSS,” EFDA_D_2MWTX5 v4.0, 2016.

[63] C. Bachmann, *Personal communication,* September 30, 2016.